SINGLE DROPLET DRYING AT HIGH TEMPERATURES

Andrew Bayly
PhD students: Wael Ebrahim, Tien Nguyen
School of Chemical and Process Engineering, University of Leeds, U.K.

IFPRI International Fine Particle Research Institute

UNIVERSITY OF LEEDS

1 Key Developments

- Drying rig development
  - Filament rig constructed, experimental mapping in progress
  - Drop tube development
    - Experimental and CFD assessment
    - Mono-dispersed atomizer selected and developed
- Material property method development
  - microwave rig discounted
- Single droplet drying modelling initiated

2 Drying at High Temperature

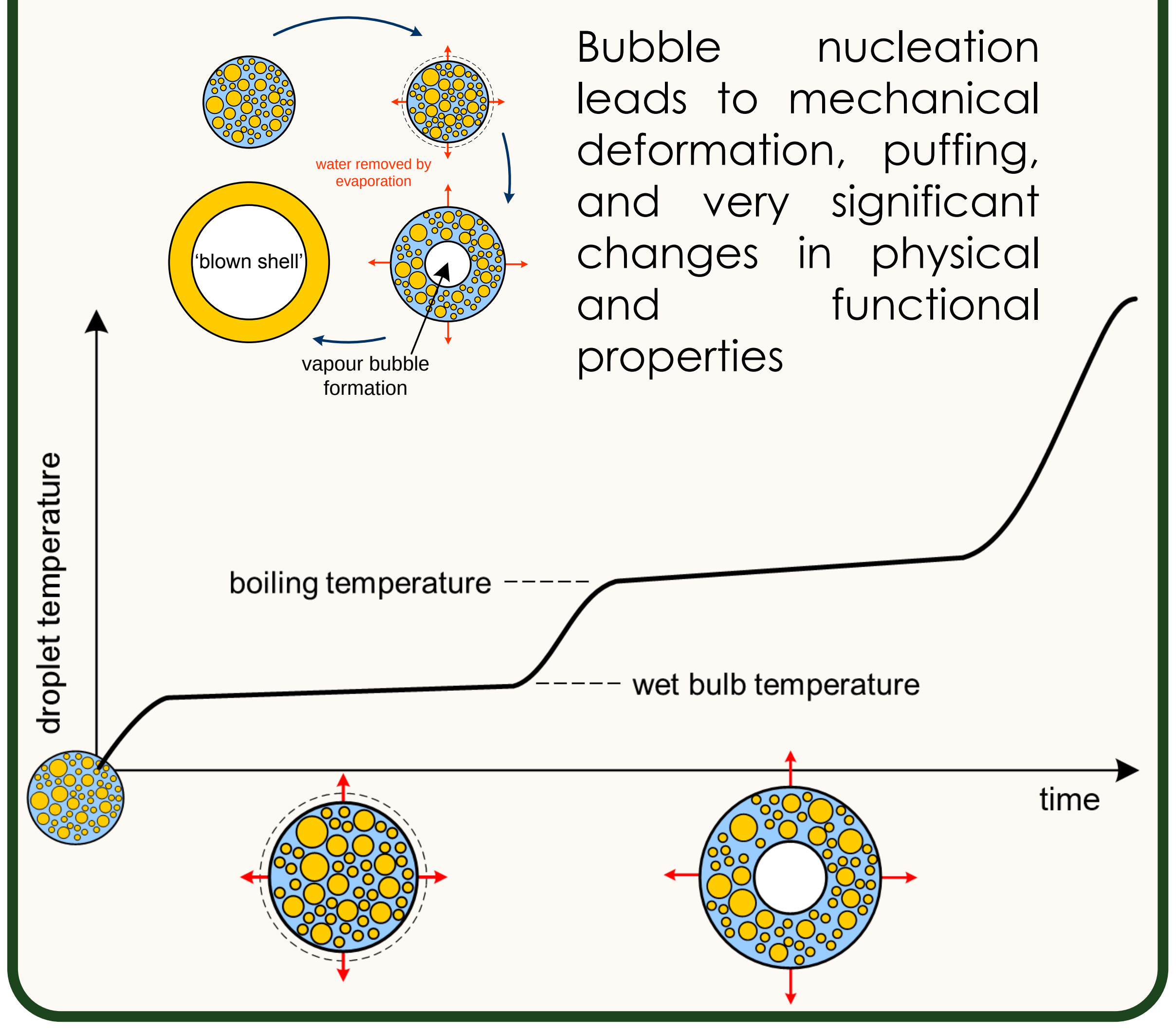

Bubble nucleation leads to mechanical deformation, puffing, and very significant changes in physical and functional properties

3 CFD Modelling of Procept Spray Drier

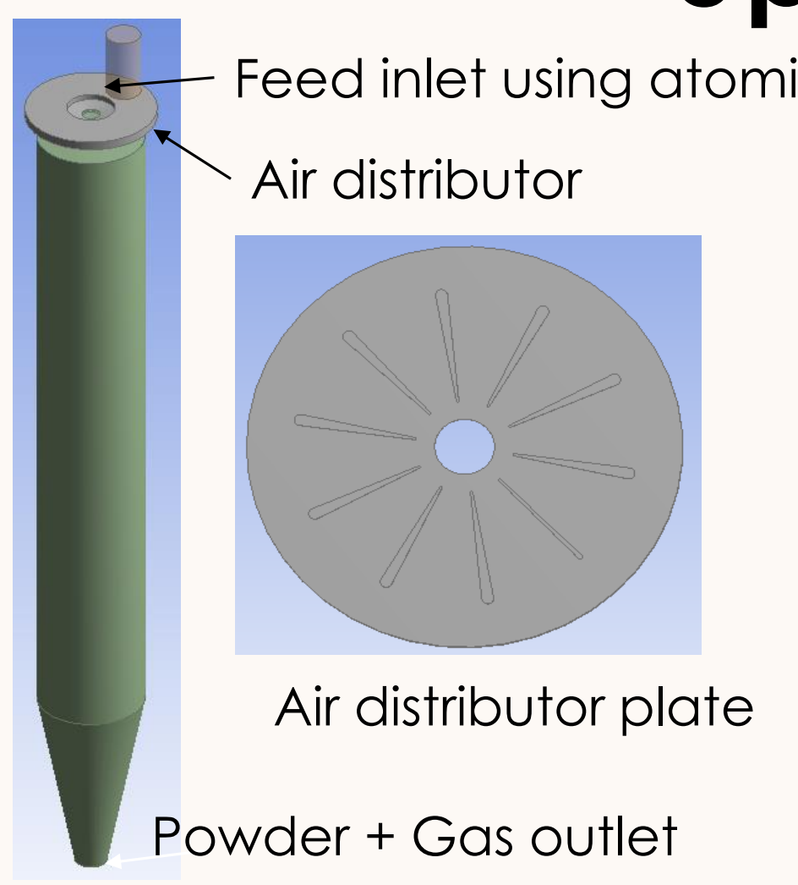

Procept Spray Dryer Geometry

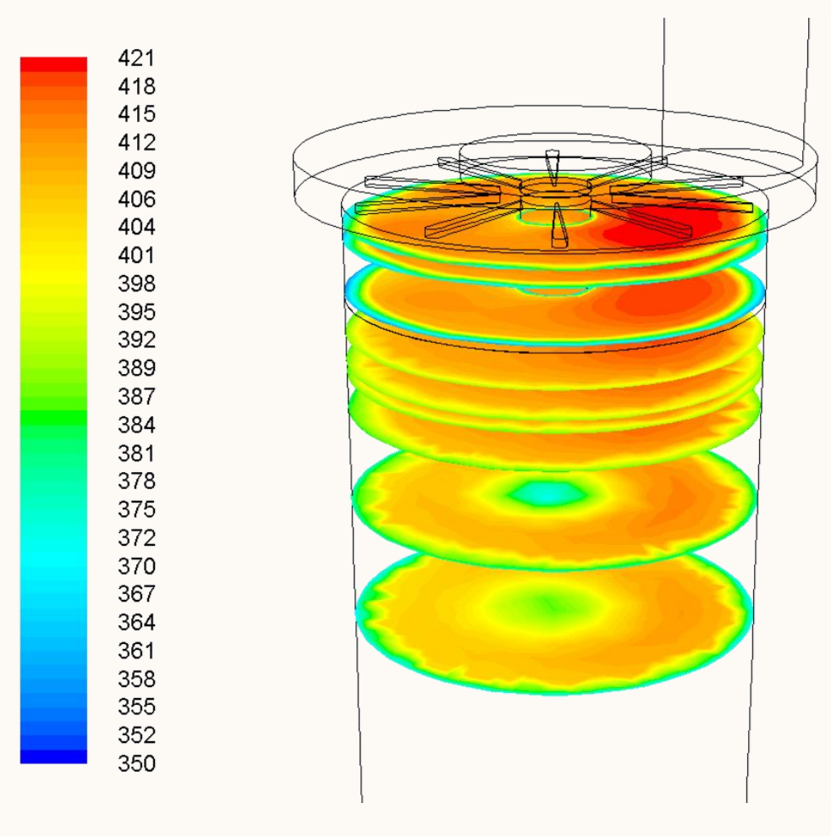

Temperature Distribution

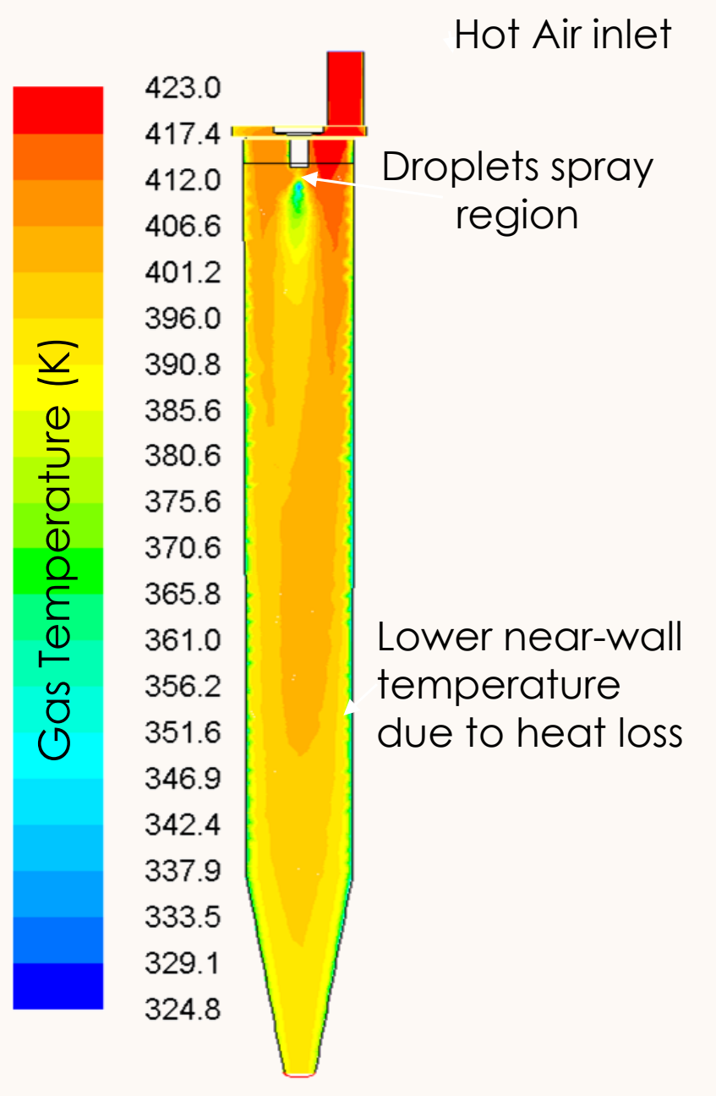

Gas Temperature Profile

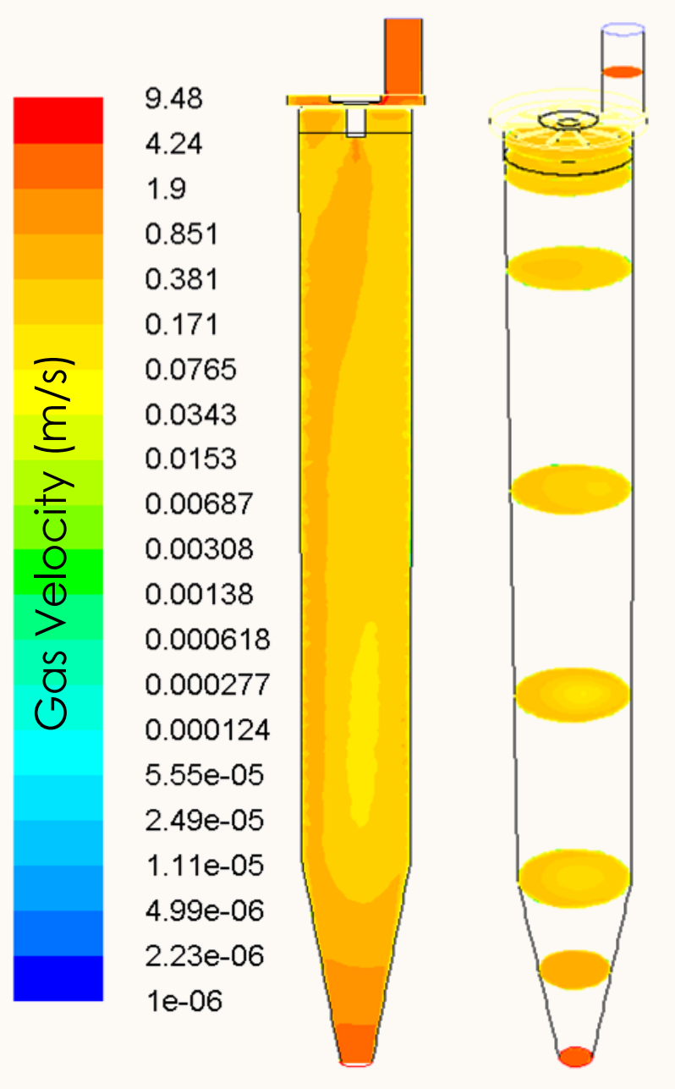

Gas Velocity Profile

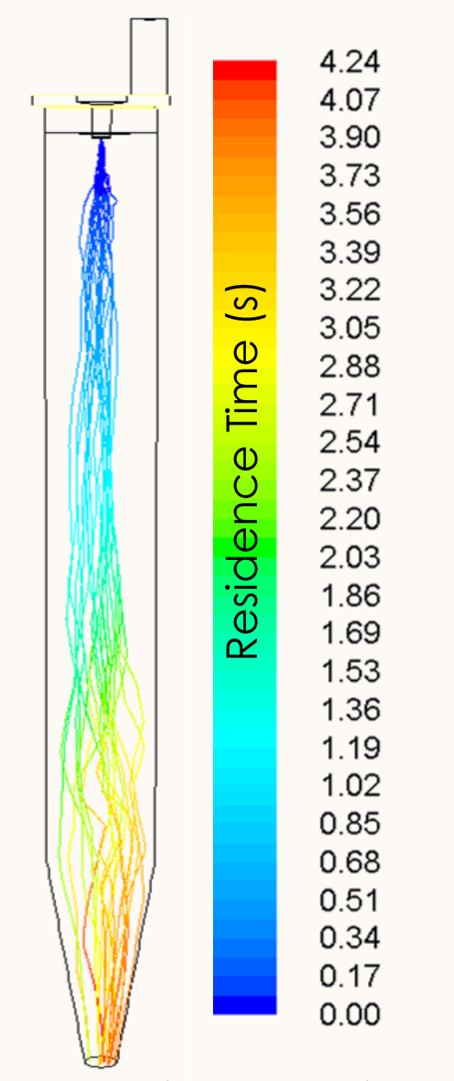

Droplets Residence Time

4 Spray Dryer Heat Loss

Position of thermocouples for temperature mapping on top of spray dryer

Temperature Profile for an Inlet Temperature of 80°C (Air Speed: 0.3 m³/min)

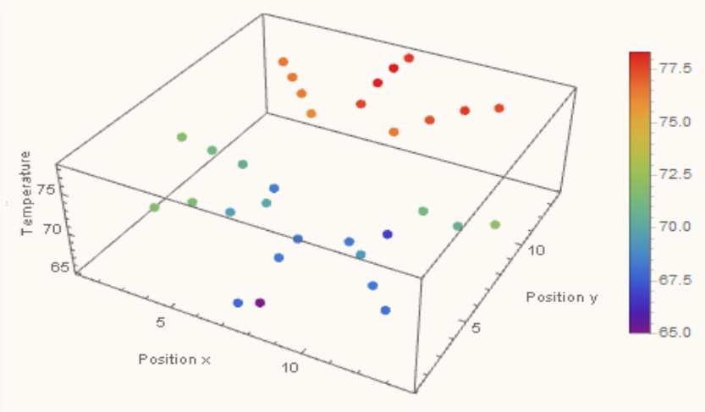

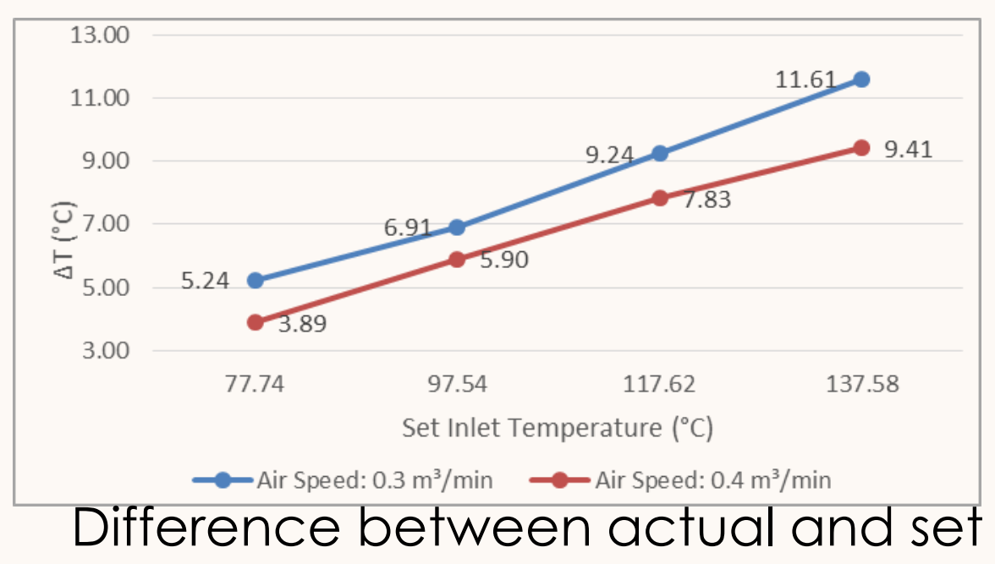

Difference between actual and set temperature

5 Droplet Generator Rig

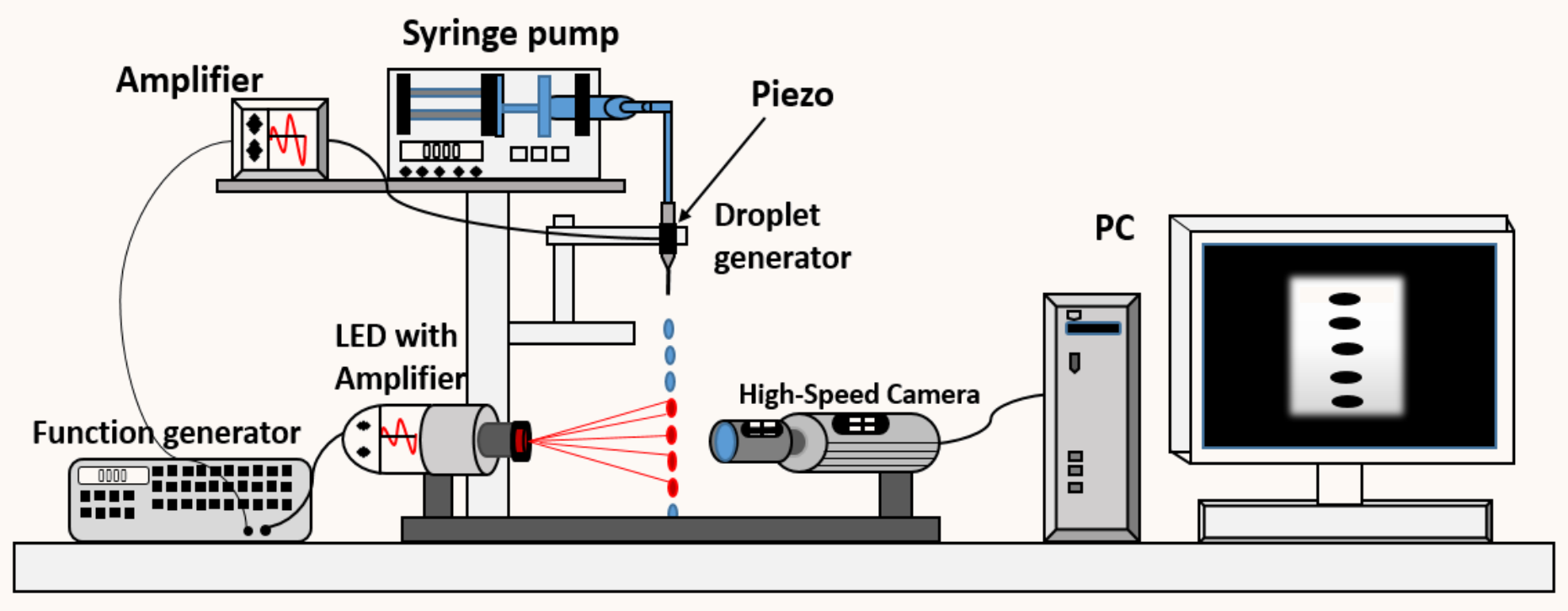

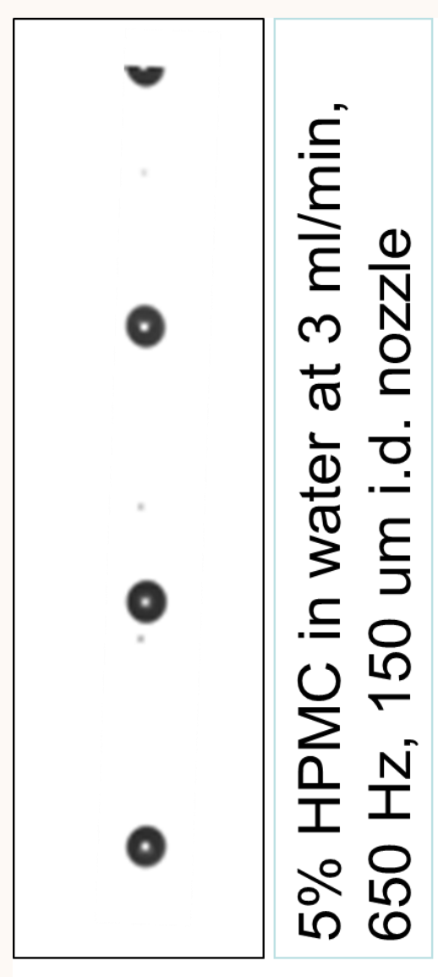

Examples of Jet break-up

Nozzle D_{in}= 0.159 mm		Nozzle D_{in}= 0.337 mm	
Flow rate (ml/min)	***f*** **(ms)** @ δ₀ = 3mVpp	**Flow rate (Ml/min)**	***f*** **(ms)** @ δ₀ = 4mVpp
3	1.52	6	Low flow rate
4	1.7	7	1.1
5	2.16	8	1.5
6	No break-up	10	Difficult to break-up

6 Schematic of Filament Drying Rig

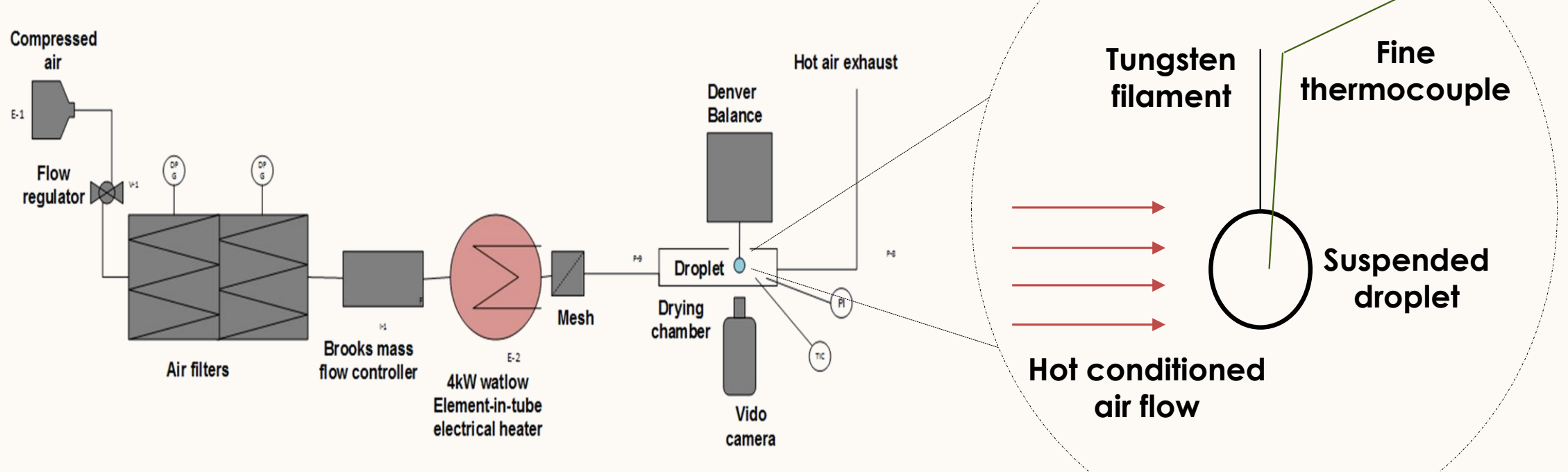

Process flow diagram of a developed single droplet drying rig

7 Experimental Results

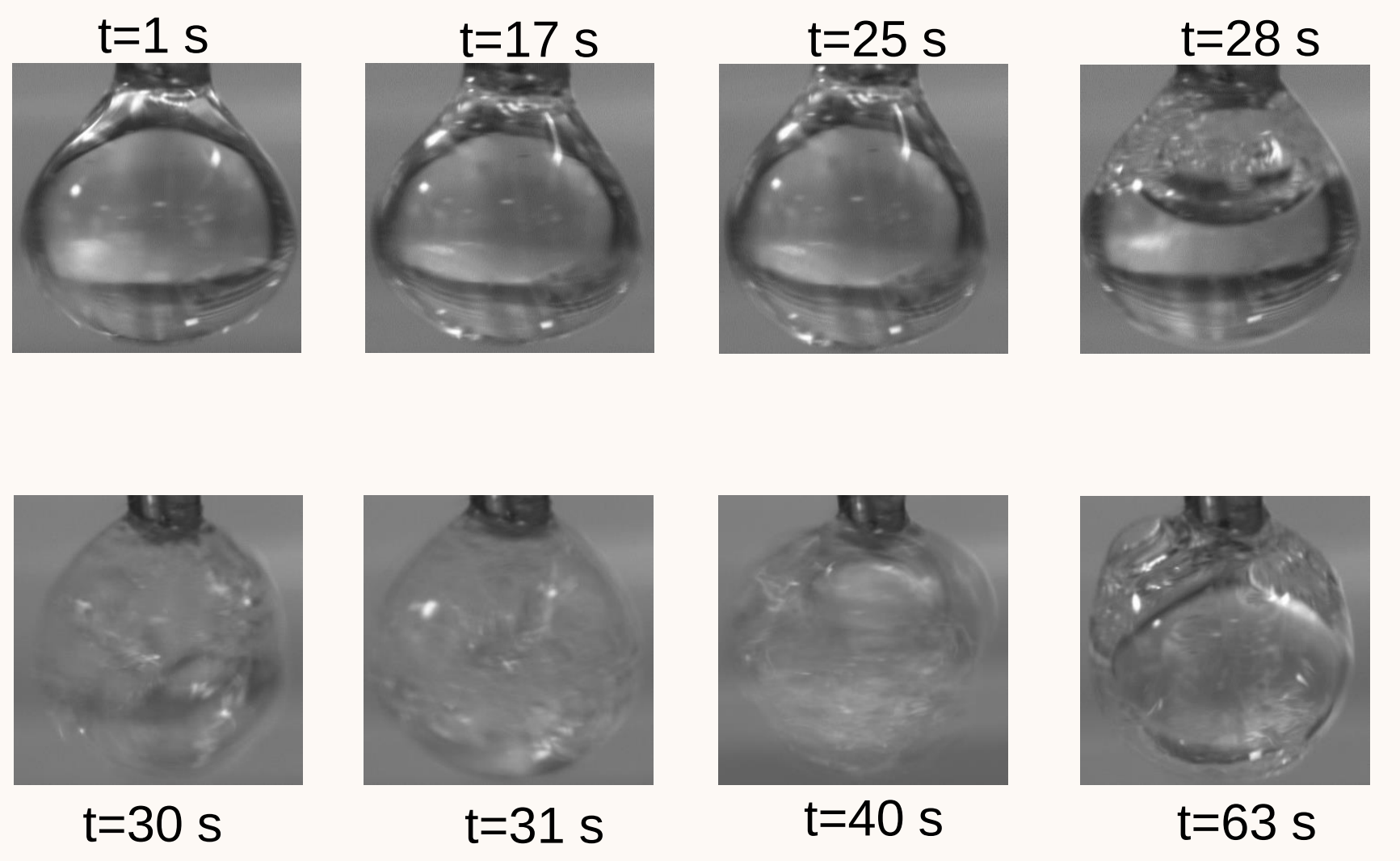

Drying of Sucrose droplet
$D_{initial}$=1.5 mm
$C_{initial}$= 45%
Drying progress: Inflation and Deflation cycles

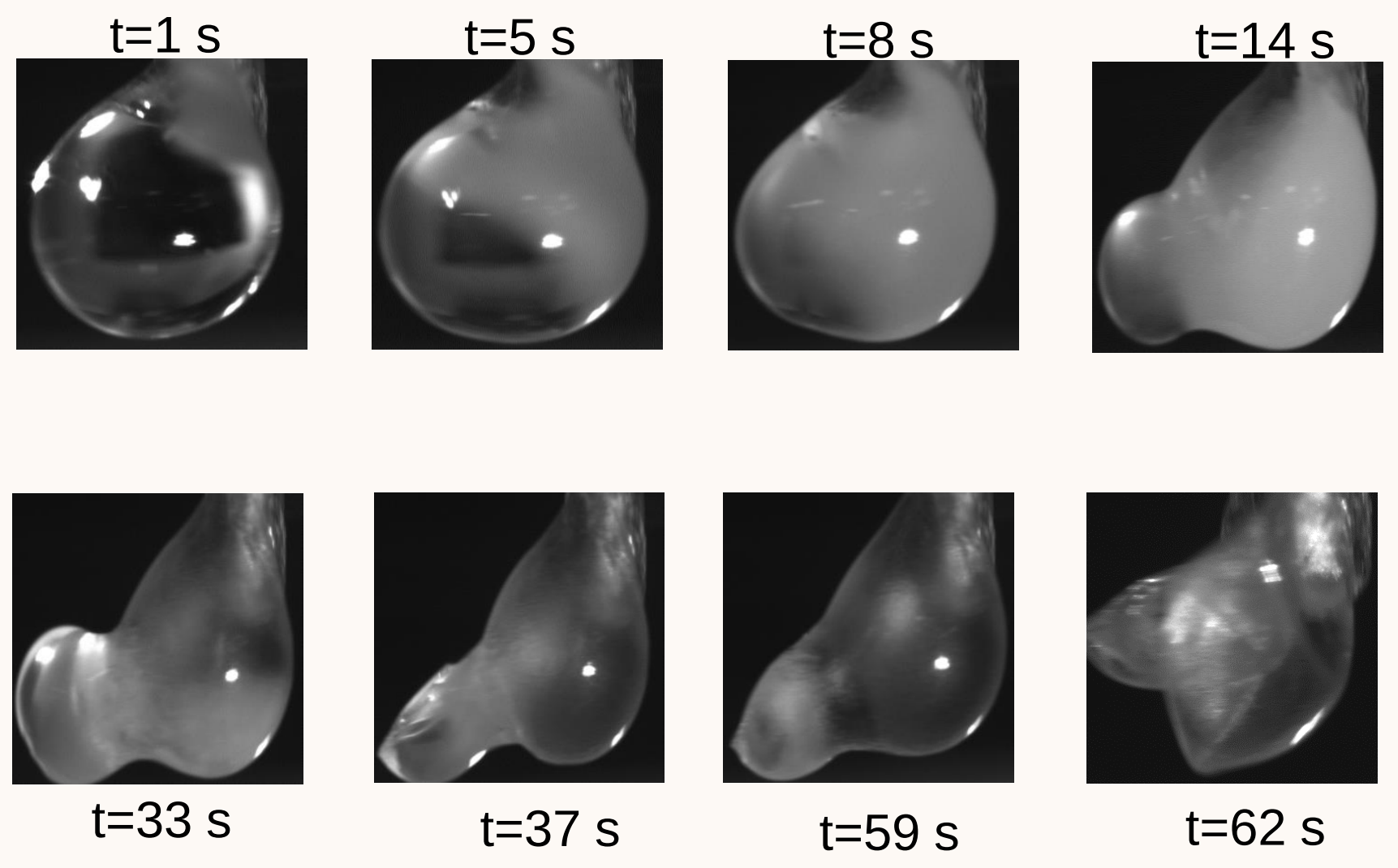

Drying of HPMC droplet
T_{air}= 190°C;
$D_{initial}$=1.4 mm
$C_{initial}$= 5%
Drying progress: Inflation and Ruptures

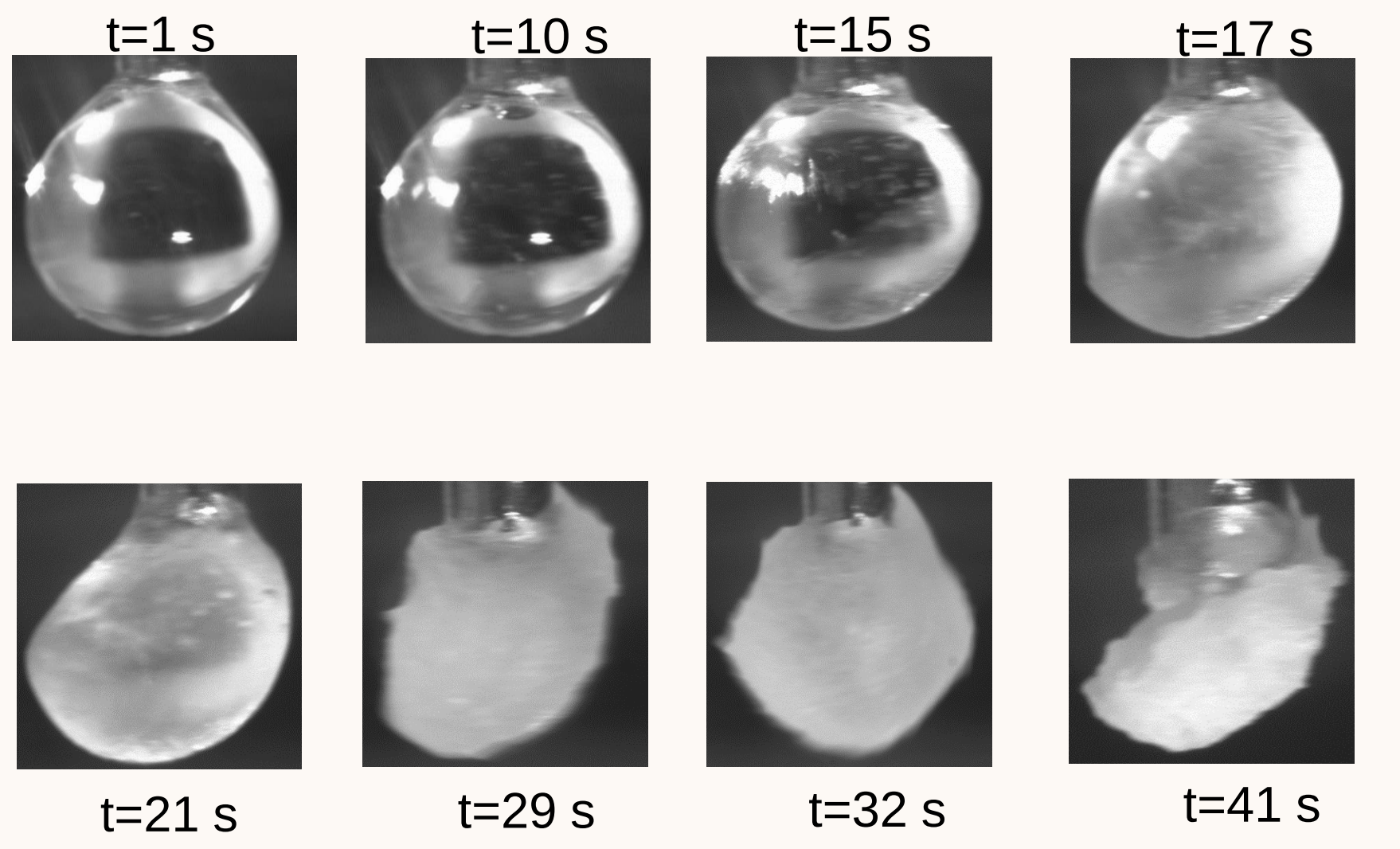

Drying of Na_2SO_4 droplet
T_{air}= 190°C;
$D_{initial}$=1.4 mm
$C_{initial}$= 10%
Drying progress: Supersaturation and crystalization

8 Single Droplet Drying Modelling Goal

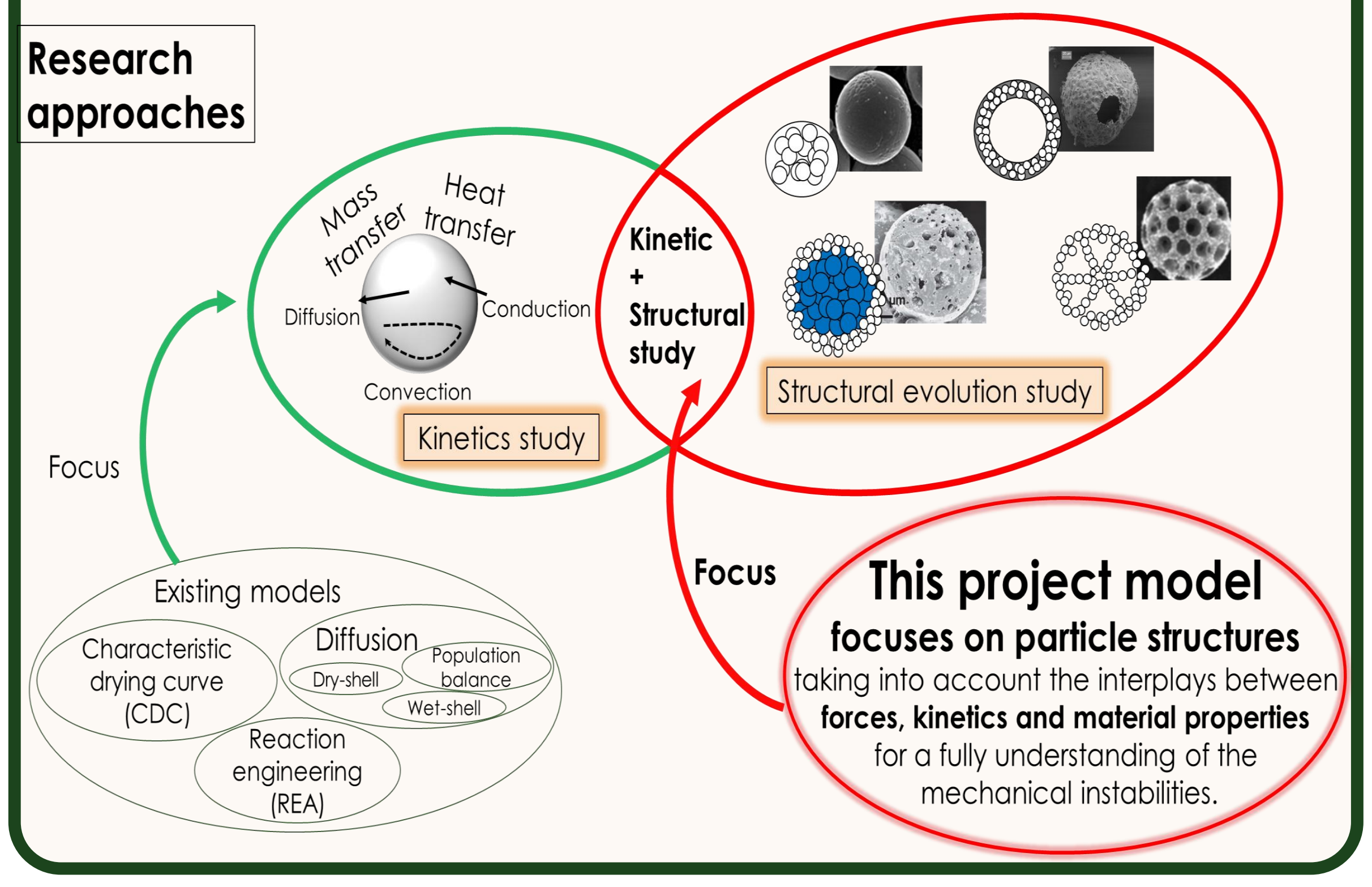

This project model focuses on particle structures taking into account the interplays between **forces, kinetics and material properties** for a fully understanding of the mechanical instabilities.

9 Structural development during drying

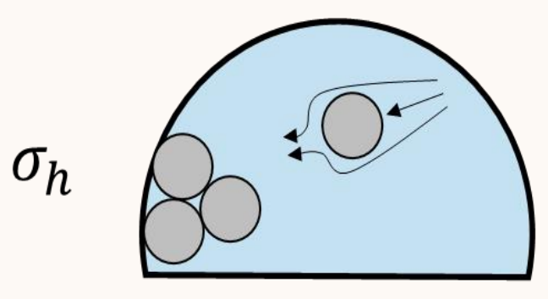

Hydrodynamic stress (σ_h)- **compressive** forces on the shell[1] →

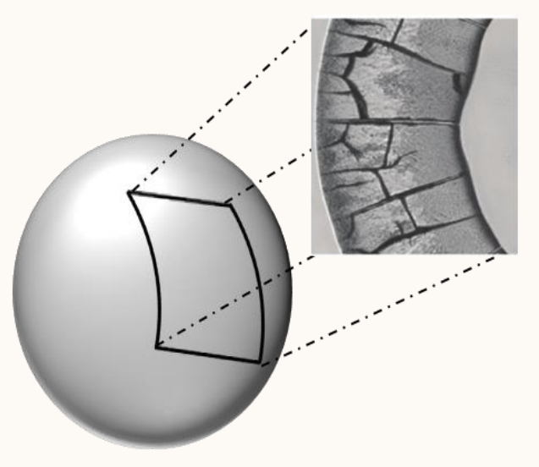

Shell thickening or 'Cracked'

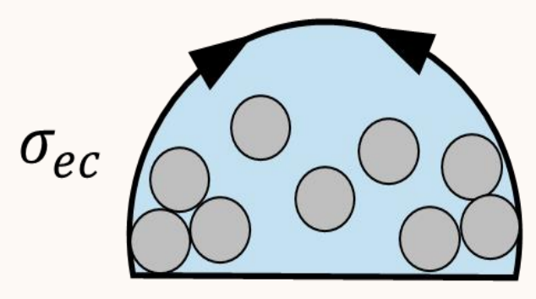

Elasto-capillary stress (σ_h)- inwards **surface tension** causing wrinkling[1] →

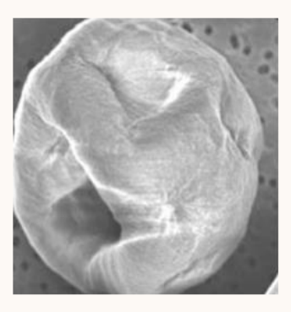

Surface wrinkle[2]

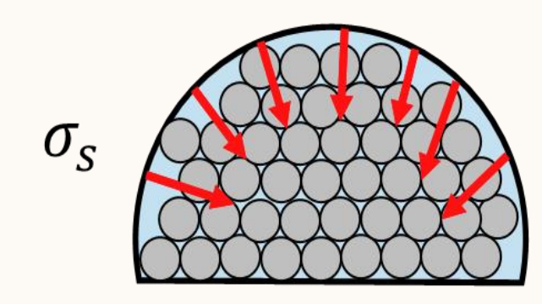

Shrinkage stress (σ_h)- **compressive forces** due to evaporating particle[1] →

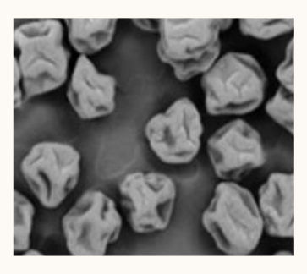

Buckling or Crack [2]

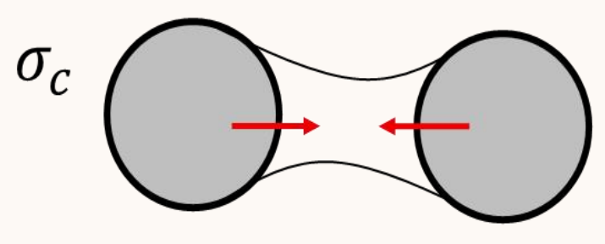

Capillary stress (σ_h)- force caused by liquid bridge between particles[1] →

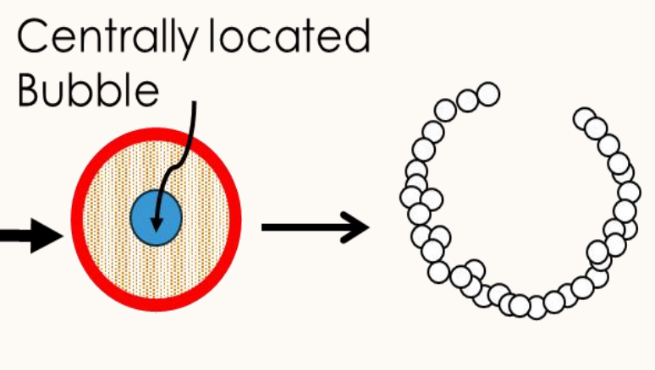

Inflated and Surface ruptured

Low internal pressure→ bubble nucleation

10 Single Droplet Drying at High Temperatures Modelling

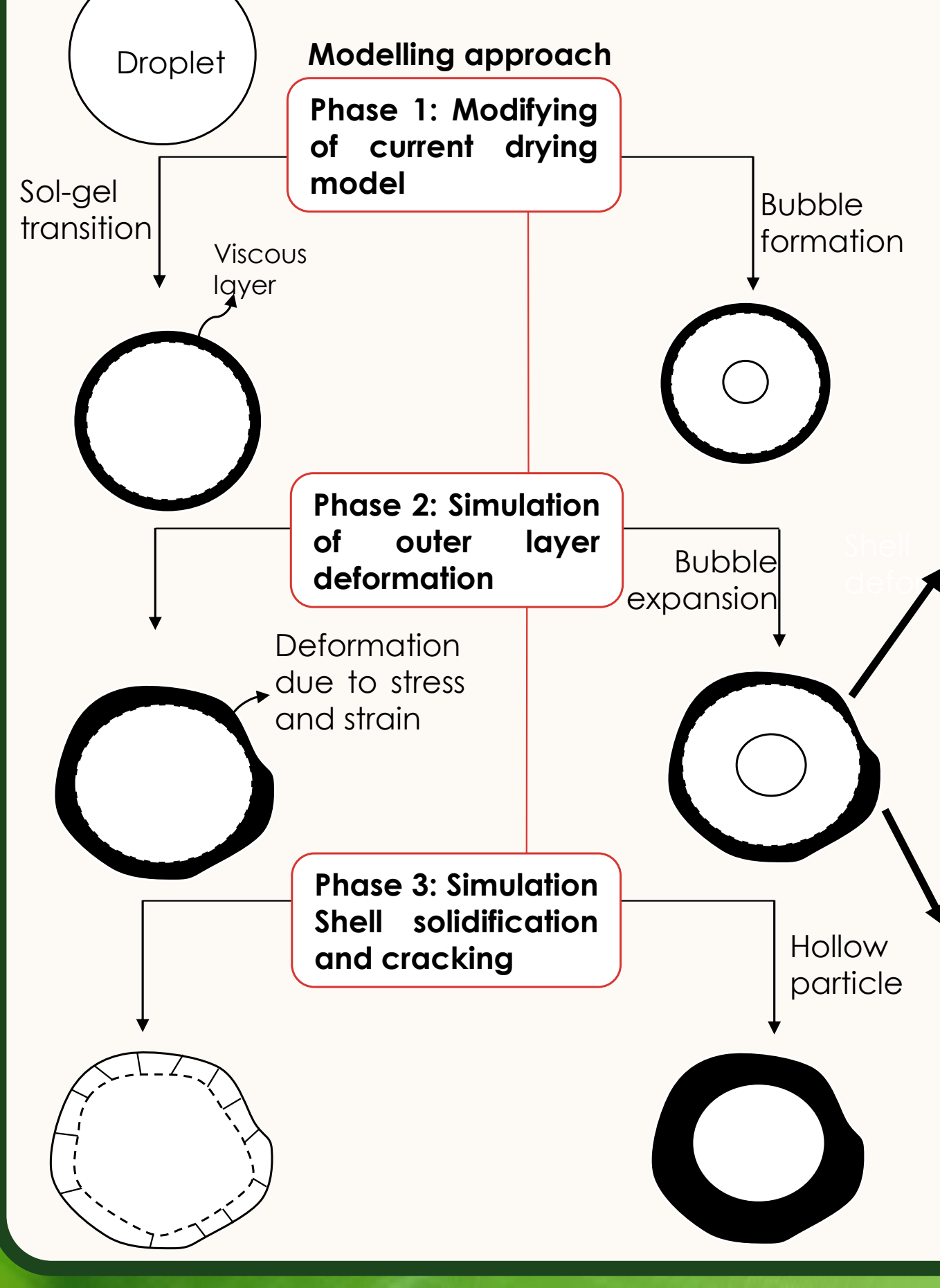

Bubble Expansion Model

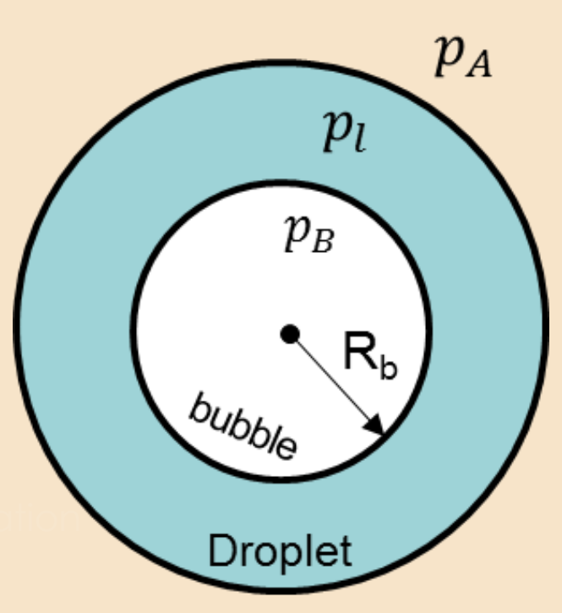

$$p_B - p_A = \left[R_D\rho_A + \rho_L\left(1-\frac{R_D}{R_B}\right)\right]\frac{d^2R}{dt^2}$$
$$+\left[\frac{3}{2}(\rho_A+\rho_L)\pm 2\rho_L\frac{R_B}{R_D}+\frac{\rho_L}{2}\left(\frac{R_B}{R_D}\right)^4\right]\left(\frac{dR}{dt}\right)^2$$
$$+2S\left(\frac{1}{R_B}+\frac{1}{R_D}\right) \longrightarrow \text{Surface tension term}$$
$$+4\left(\frac{\mu_A}{R_D}+\frac{\mu_L}{R_B}\right)\frac{dR}{dt} \longrightarrow \text{Viscous term}$$

- **Aim**: to formulate the bubble expansion rate as a function of internal bubble pressure and air pressure.
- **Approach**: Rayleigh-Plesset methods.
- **Boundary conditions:** no mass transfer across bubble-liquid and liquid-air interfaces.

Bubble rising study

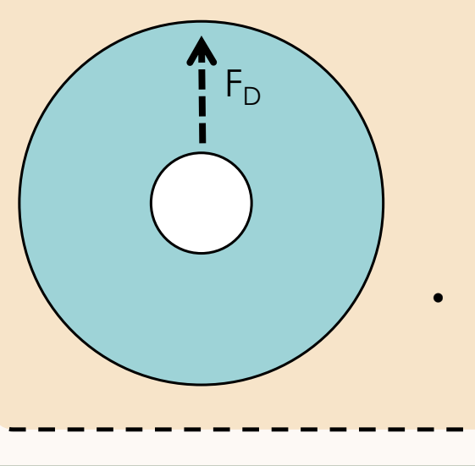

$$Drag\ coefficient, C_D = \frac{1}{18}\frac{d_0^2 g(\rho_{bubble}-\rho_{gas})}{\mu}$$

$$Drying\ time, \tau_{dry} = \frac{\lambda\rho r_0^2}{2k(T_g-T_p)}$$

- A comparison between how fast the bubble moves to the droplet surface and how fast the droplet shrinks due to evaporation

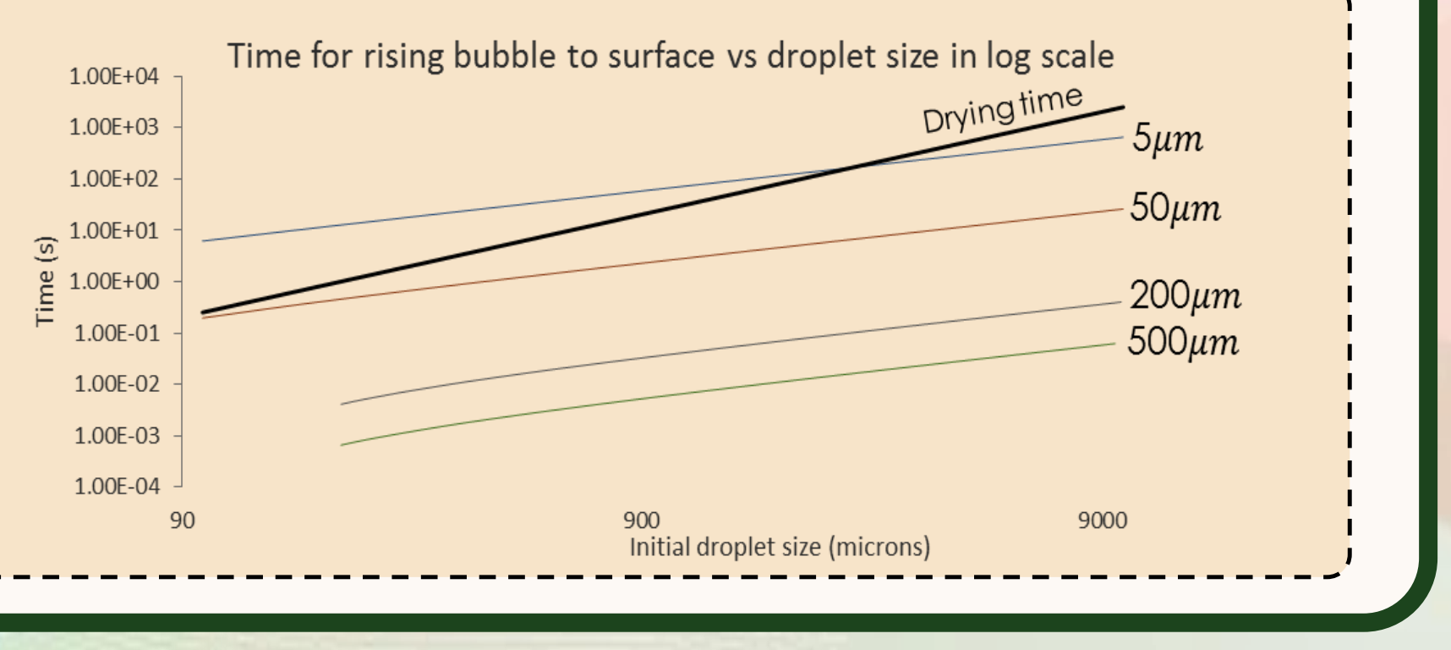

11 Summary and Future Plan

- Filament rig – experimental mapping
- Drying rig development – drop tube
- Material property method evaluation
- Modelling – developing a resolved model

A main goal is to develop a regime map which links material properties and drying conditions to final morphology.

Acknowledgements

- Prof. Phil Threfall Holmes, Prof. Nik Kapur
- Dr. Muzammil Ali, Karrar Al-Dirawi, Khairul Mohd Faris , Daniella De La Vega , Dan Wesley , Leeds technicians
- Funding also received from EPSRC and the University of Leeds

References

[1]: van der Kooij HM, van de Kerkhof GT, Sprakel J.. 2016;12(11). doi:10.1039/C5SM02406D.

[2]:Rogers S, Wu WD, Lin SXQ, Chen XD. Biochem Eng J. 2012;62:92-100. doi:10.1016/j.bej.2011.11.002

Nonlocal Rheology of Dense Granular Flow

Zhu Tang[1], Ted Brzinski[1,2], Michael Shearer[3] and Karen E. Daniels[1]
1: Department of Physics, North Carolina State University, USA
2: Department of Physics and Astronomy, Haverford College, USA
3: Department of Mathematics, North Carolina State University, USA

Local rheology

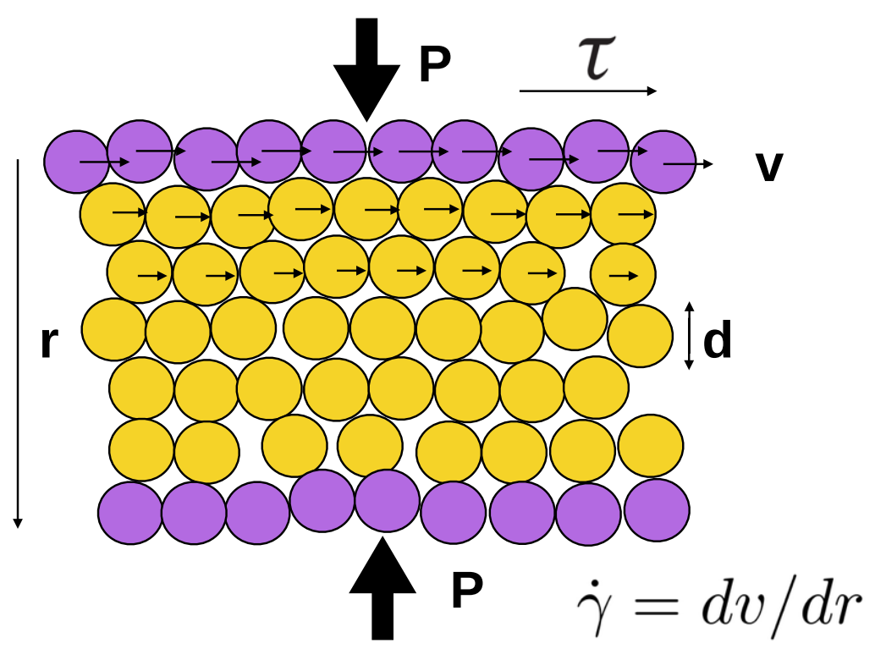

$\dot\gamma = dv/dr$

Granular materials flow in response to external loading: Inertial number I describes the flow (high I is more rapid)

$$I = \frac{|\dot\gamma| d}{\sqrt{P/\rho}}$$

and is often observed to be in an one to one relationship with applied stress ratio

$$\mu = \frac{\tau}{P}$$

. Some failures of local rheology:

- cannot quantitatively capture the transition from inertial to quasistatic (but still creeping) flow [2]
- dimensions of shear bands formed by boundary-driven flows depend on geometry and grain size [3,4]
- shear/vibration in one region of a granular material can fluidize regions from the perturbation [5,6]

Two nonlocal rheologies

Fitting parameters are in green

Measured values are in red.

cooperative model: (Kamrin & Koval [7])
granular fluidity g:

$$g_{loc}(\mu, P) = H(\mu - \mu_s)\frac{\mu - \mu_s}{b\mu}\sqrt{\frac{P}{\rho d^2}} \tag{1}$$

cooperative length ξ:

$$\xi = A(\frac{1 + H(\mu_s - \mu)}{|\mu - \mu_s|})^{\alpha} d \tag{2}$$

$$\xi^2 \bigtriangledown^2 g = (g - g_{loc}) \tag{3}$$

gradient model: (Bouzid et al. [8])
I_g determines the constitutive relation:

$$I_g(f) = \frac{Tf}{1 - aTf} \tag{4}$$

granular fluidity f:

$$\dot\gamma - \frac{I_g(f)}{T} + l^2 \bigtriangledown^2 f = 0 \tag{5}$$

- both models include a Laplacian term to account for nonlocal effects
- cooperative model: based on extending a local Bagnold-type granular flow law
- gradient model: based on gradient expansion
- cooperative model: nonlocal length scale ξ has a divergence around μ_s
- gradient model: nonlocal length scale l is a constant

Aim: to compare experimental and theoretical $\mu(I)$, speed profiles and length scale.

	experimental	theoretical
g or f	$\dot\gamma_e/\mu$ or $\mu_s\dot\gamma_e/\mu$	solved by eq.(1-3) or (4-5)
v	particle tracking	$\int_{R_o}^{r} g\mu dr$ or $\int_{R_o}^{r} \frac{f\mu}{\mu_s} dr$
ξ^2	$\frac{(g_e - g_{loc})}{\bigtriangledown^2 g_e}$	eq.(3)
I	$\frac{\|\dot\gamma_e\| d}{\sqrt{P/\rho}}$	$\frac{g\mu d}{\sqrt{P/\rho}}$ or $\frac{f\mu d}{\mu_s\sqrt{P/\rho}}$

The variables with subscript e are from experimental measurement.

Contact Information

Web: nile.physics.ncsu.edu
Email: ztang2@ncsu.edu
Thanks: IFPRI and NSF DMR-1206808

Apparatus

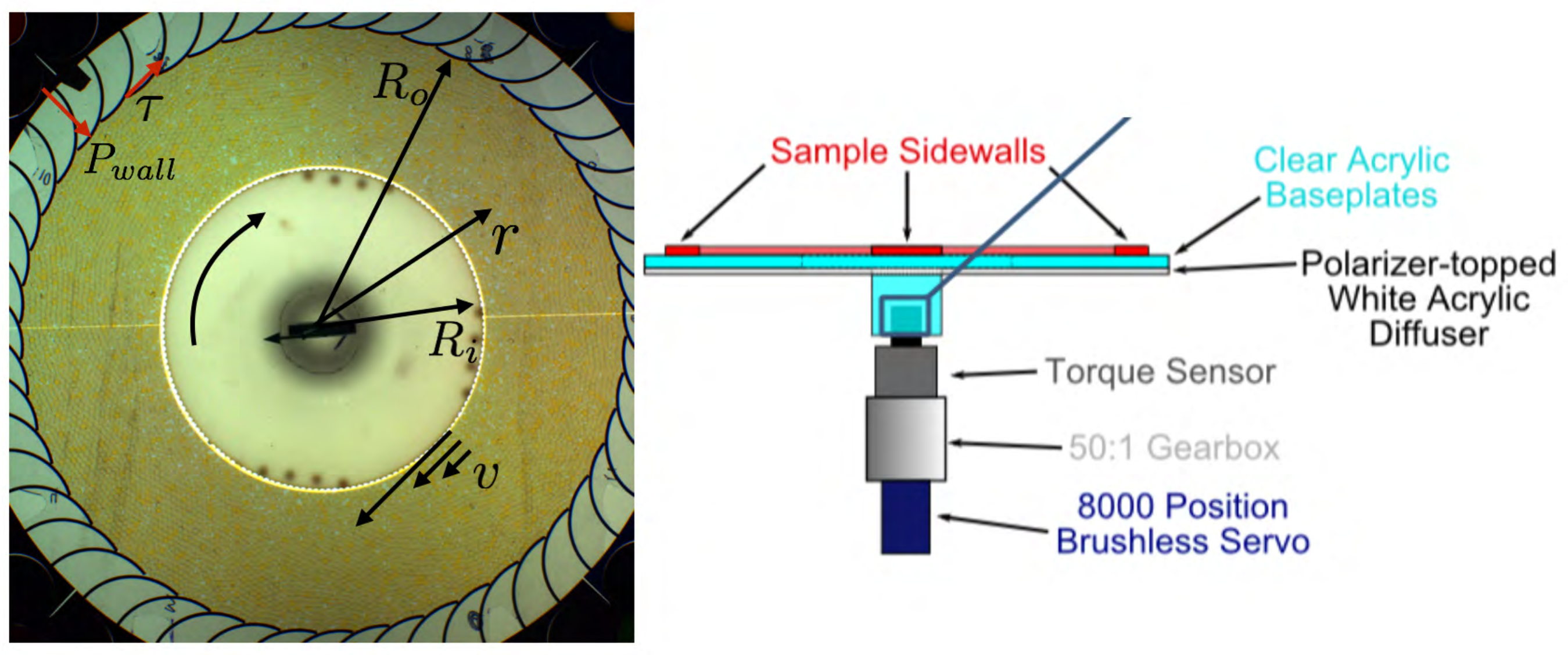

Figure 1: quasi-2D apparatus with leaf spring wall

- a fixed outer wall ($R_o = 28$ cm) and a rotating inner wall ($R_i = 15$ cm), with 5610 or 5760 particles in a flat layer
- packing density ϕ = fraction of area occupied by particles
- can run indefinitely
- wall torque sensor on the inner wall shaft measures torque
- change inner wall rotation speed and number of disks

Measuring Forces: μ

$$\tau(r) = \tau_{wall}\left(\frac{R_i}{r}\right)^2 + \tau_0\left[1 - e^{-(r-R_i)/r_0}\right]$$

- first term: shear stress at inner wall τ_{wall} calculated from torque sensor
- second term: basal friction (which is proportional to $\phi(r)$) Best fit: $\tau_0 = 250$ Pa and $r_0 = 1.67$

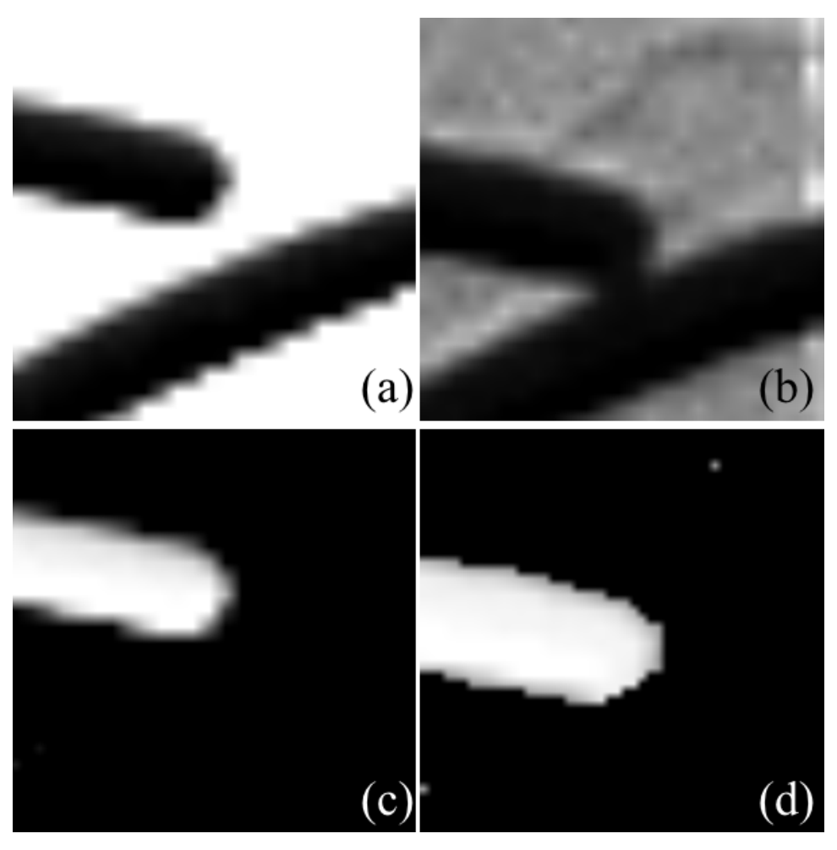

- leaf springs: measure pressure P deformation via calibration [11]
- assume the radial pressure is uniform everywhere
- $\mu(r) = \frac{\tau(r)}{P}$

Tracking Particles: I

- find the locations of grains in each frame with Hough Transform [9]. Use particle tracking code [10] to track the trajectory for each particle
- calculate the speed profile and $\dot\gamma = \frac{1}{2}(\frac{dv}{dr} - \frac{v}{r})$ via Fourier derivative
- compare experimental $g = \dot\gamma/\mu$ and $f = \mu_s\dot\gamma/\mu$ with theoretical $g(r)$ and $f(r)$solved by eq.(1)-(3) and eq.(4)-(5) via matlab code bvp4c

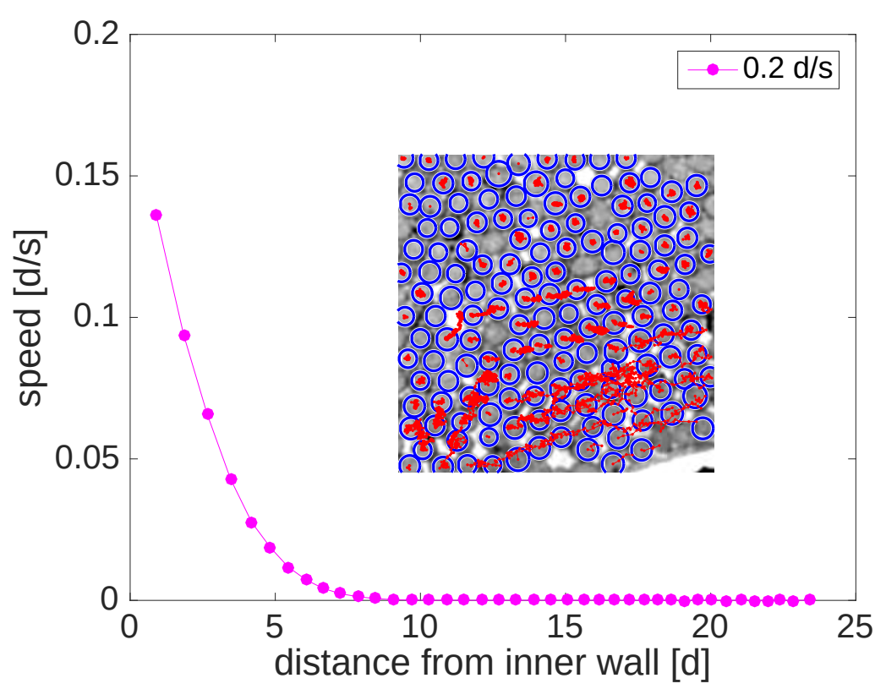

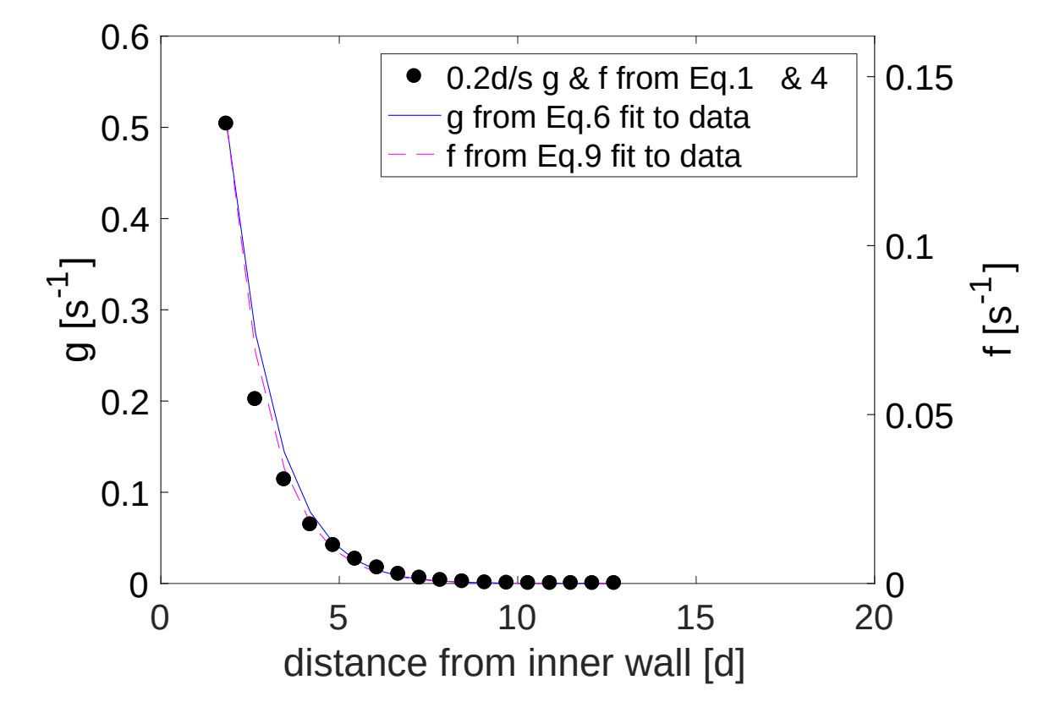

Results: evaluate the two models

- **cooperative model:** parameters $A = 0.26$, $\mu_s = 0.27$, $b = 1.1$ were optimized by least squares method one by one and work well for all data sets Kamrin's parameters [2]: $A = 0.31$, $\mu_s = 0.26$, $b = 1.05$.
- **gradient model:** parameters $l = 1.08$, $\mu_s = 0.27$, $a = 7.2$ were optimized by Levenberg-Marquardt algorithm and work well for all data sets.

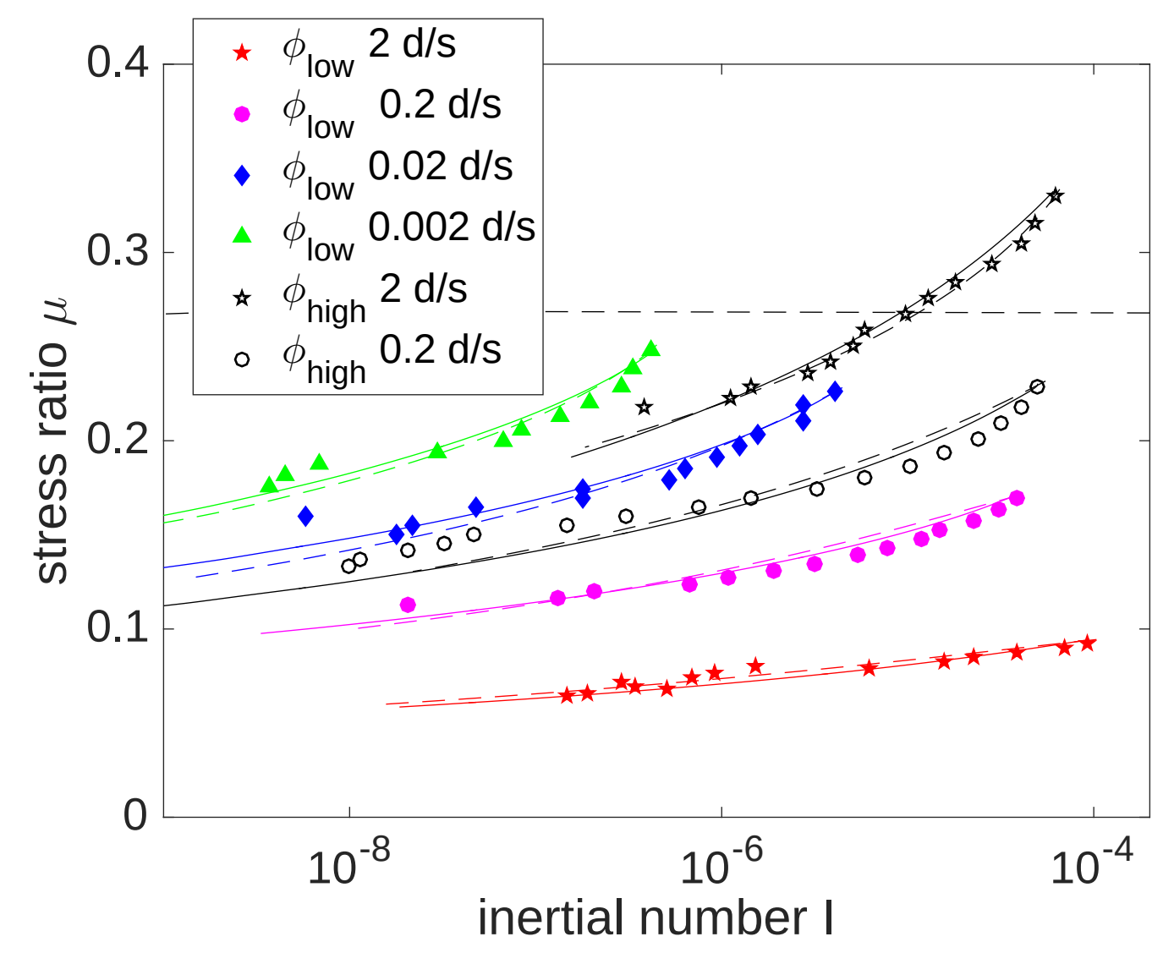

Figure 2: For the four low ϕ, the one with higher inner wall rotation speed, have lower μ under the same I. However, for the high ϕ, the situation is reversed. For the same inner wall rotation speed, higher ϕ leads to higher μ under the same I.

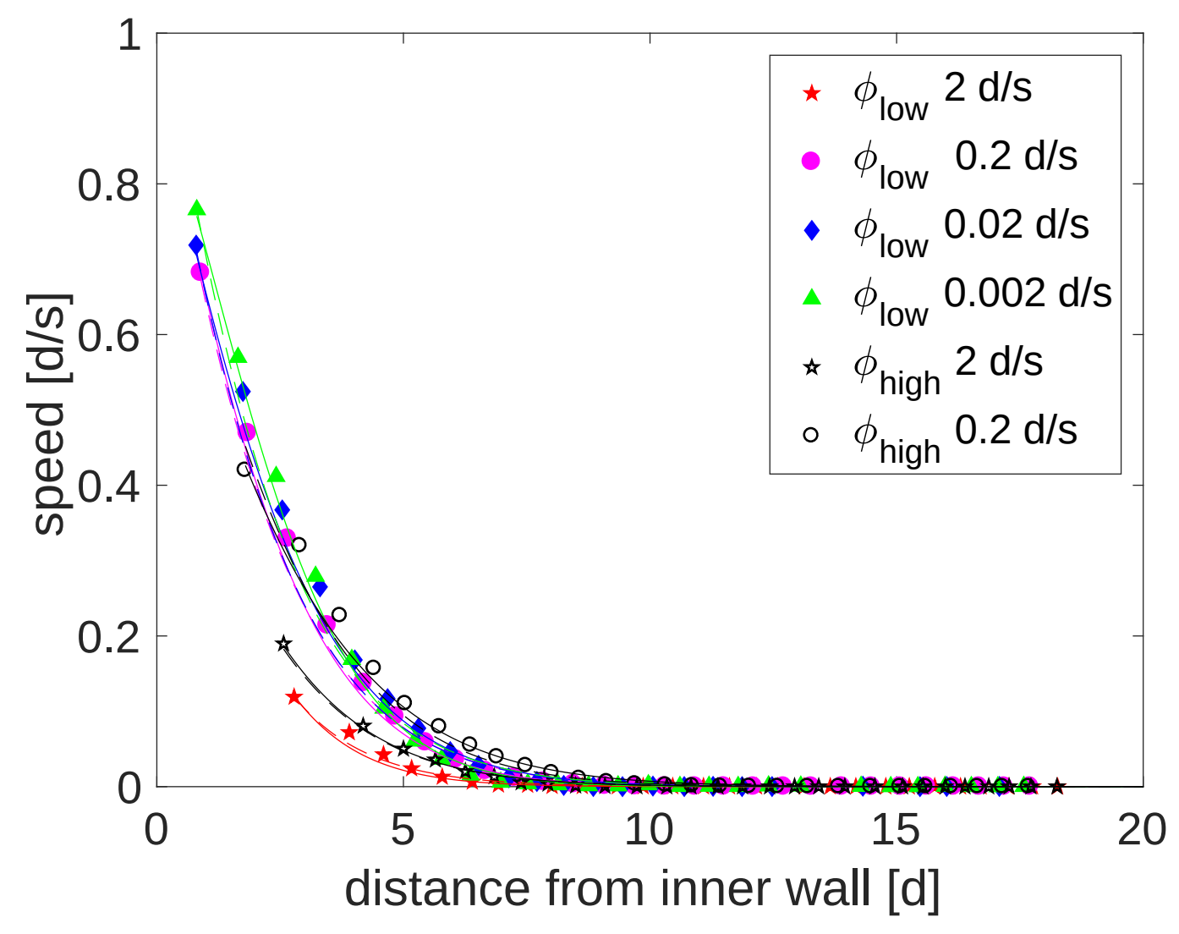

Figure 3: Both of the nonlocal models match our experimental $\mu(I)$ and speed profiles well, using a single set of parameters.

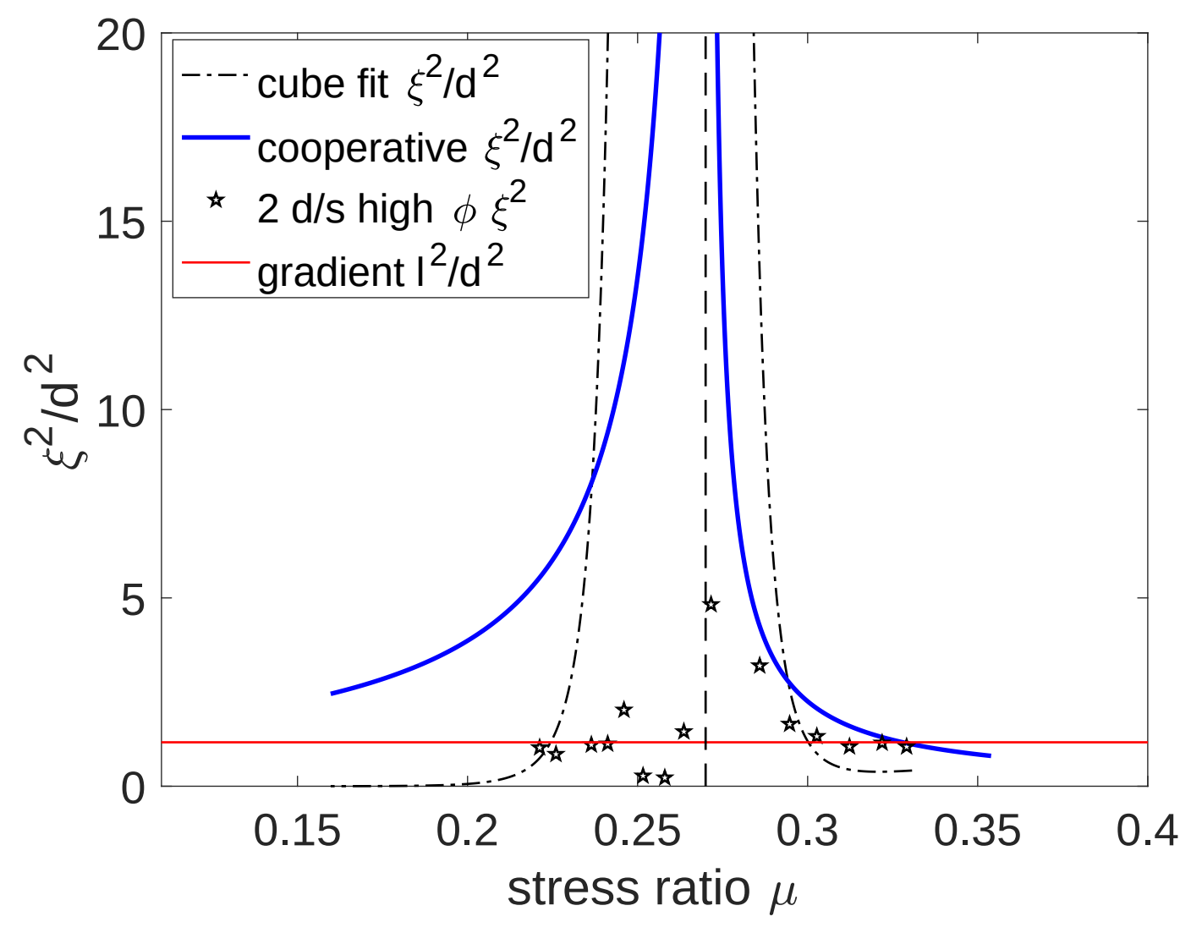

Figure 4: We test for a divergence in $\xi(\mu)$, shown by solid line, using two methods. (1) Numerical derivatives of $v(r)$, shown by ☆. (2) Analytical derivatives of exponential fit to $v(r)$, shown by dash-dot curves.

Conclusion

- new experimental apparatus with spring boundaries allows for monitoring pressure during shear
- adapt existing models to account for basal friction
- both models are able to fit the measured $\mu(I)$ data, using a single set of parameters across all (ϕ, v)
- evidence for a diverging length scale at μ_s supports the cooperative model
- next step: test the rheology for particles of different shapes

References

[1] Forterre, Pouliquen, Annu. Rev. Fluid Mech. 2008
[2] Koval, Roux, Corfdir, Chevoir, Phys.Rev.E. 2009
[3] GDR MiDi, Eur.Phys.J.E. 2004
[4] Cheng, Lechman, Fernandez-Barbero, Grest, Jaeger, Karczmar, Möbius, Nagel. Phys.Rev.Lett 2006
[5] Nichol, Zanin, Bastien, Wandersman, van Hecke. Phys.Rev.Lett 2010
[6] Reddy, Forterre, Pouliquen. Phys.Rev.Lett 2011
[7] Kamrin, Koval, Phys.Rev.Lett. 2012
[8] Bouzid, Trulsson, Claudin, Clément, Andreotti, Phys.Rev.Lett. 2013
[9] http://www.mathworks.com/help/images/ref/imfindcircles.html
[10] http://site.physics.georgetown.edu/matlab/
[11] Tang, Brzinski, Daniels. Powder and Grains 2017 (arXiv:1704.08295)

Creating Tuneable Agglomerates via 3D Printing

Ruihuan Ge[1], Mojtaba Ghadiri[2] and Karen Hapgood[1,3]
[1]Monash Advanced Particle Engineering Laboratory, Chemical Engineering, Monash University, Australia
[2]Institute of Particle Science and Engineering, University of Leeds, UK
[3]School of Engineering, Deakin University, Australia

Introduction & Objective

- ➢To explore the mechanical properties and breakage characteristics of agglomerates, it is essential to produce test agglomerates with controlled properties to replicate the complex structure, and validate simulation models.
- ➢Agglomerates with defined and tuneable properties were produced using 3D printing technology.
- ➢Quasi-static and impact breakage tests were conducted to vary strain rate under controlled conditions.
- ➢DEM breakage simulations with agglomerate properties matching the 3D printed agglomerate were conducted and compared with experimental results.


Create agglomerate structures


Replicate agglomerates by Solidworks


3D printed agglomerates

1. Agglomerate design

- 3D printed agglomerates (approx. 25-30 mm size) have rigid primary particles (d_p= 4mm) connected by cylindrical inter particle bonds.
- Two different inter-particle bond strengths were investigated by printing the agglomerate using either rigid Verowhite bonds, or ductile DM 9895 polymer.
- Three different agglomerate structures were printed.
  - Cubic tetrahedral structure (L_b =4.25 mm, r_b=1.3 mm)
  - Random spherical structure ε=44% (L_b ~4 mm, r_b=1 mm)
  - Random spherical structure ε=57% (L_b ~5.6 mm, r_b=1 mm)

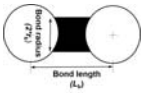

	Cubic structure	**Dense structure (ε=44 %)**	**Loose structure (ε=57 %)**
Rigid bond (VeroWhitePlus^{TM})			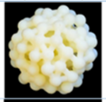
Soft bond (DM 9895)	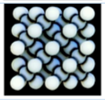		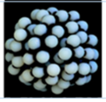

2. Agglomerate breakage

Quasi-static compression tests -0.02 mm/s platen loading rate

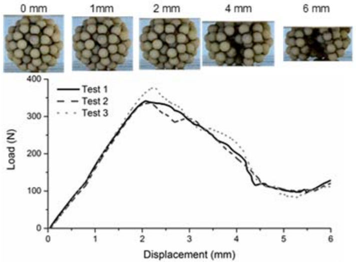

- Dense structured agglomerate (ε=44%) shows meridian crack.

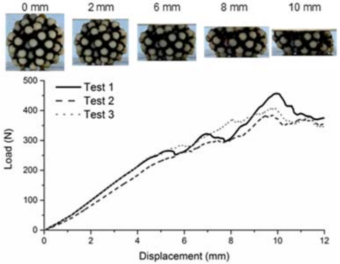

- Loose structure (ε=57%) is crushed progressively via ductile failure.

Impact test -4 m/s drop weight impact velocity

- The rigid material bonds show brittle breakage characteristics, the dense structure show meridian crack while the loose structure show oblique crack.
- The agglomerates with soft bonds show rebound behavior.

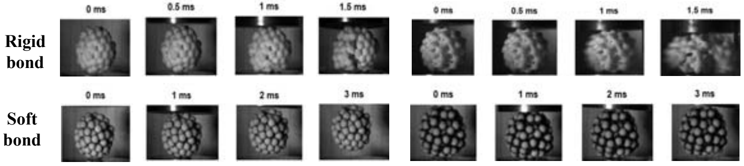

(a) Dense (ε=44%) structure (b) Loose (ε=57%) structure

3. DEM simulation

- DEM simulations using Timoshenko Beam Bond Model (TBBM)
- In the TBBM model, a Timoshenko beam element is used to connect the centres of two primary particles, denoted particle A and particle B.
- Bonding & particle parameters were based on experimental measurement and data offered by the vendor.

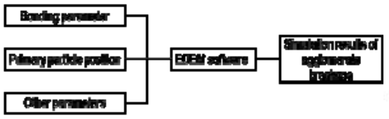

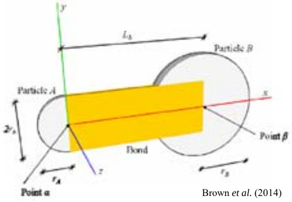

Brown *et al.* (2014)

- To compensate the different in bond geometry in TBBM, the bond Young's modulus E_b was corrected using the doublet tensile test results considering different printing layer directions.
- The corrected E_b is shown below.

$$E_b = \frac{k_t \cdot L_b}{A_b}$$

k_t: Bond stiffness determined by doublet tests.
L_b : Bond length in TBBM model.
$A_b = \pi r_b^2$: Bond cross-sectional area.

Doublet type	Parallel loading	Perpendicular loading
Cubic tetrahedral structure (L_b =4.25 mm, r_b=1.3 mm)	E_b = 116 MPa	E_b = 142 MPa
Spherical random structure (L_b =4 mm, r_b=1 mm)	E_b = 254 MPa	E_b = 195 MPa

	Parameter	Value
Bonds	Young's modulus (MPa)	Varies with different bond geometry
	Poisson's ratio	0.4
	Compressive strength (MPa)	50
	Tensile strength (MPa)	10
	Shear strength (MPa)	10
Steel platen	Static friction coefficient	0.3
	Coefficient of restitution	0.9
	Density (kg/m^3)	7800
	Poisson ratio	0.3
	Shear modulus (GPa)	70
Particle	Diameter (m)	0.004
	Static friction coefficient	0.3
	Coefficient of restitution	0.9
	Density (kg/m^3)	1200
	Poisson ratio	0.3
	Young's modulus (GPa)	1.0

4. Comparison of breakage patterns

- Simulation & experiments show similar breakage patterns for each agglomerate structure.
- For the cubic tetrahedral structured agglomerate, the bonds fail along slip planes.
- The spherical random structured agglomerate fails through the meridian plane.

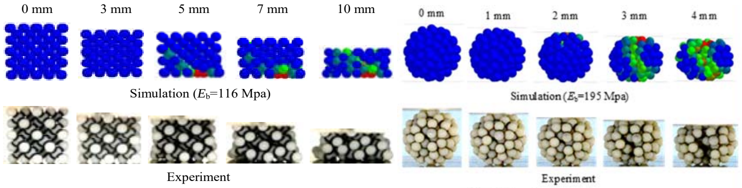

(a) Cubic tetrahedral structure (b) Spherical random structure

5. Comparison of load-displacement curves

- For the cubic tetrahedral structure agglomerate, simulation predictions are within the range of the experimental measurement results.
- For the spherical random structured agglomerate, the predicted compressive loads are far lower than the corresponding experimental results.

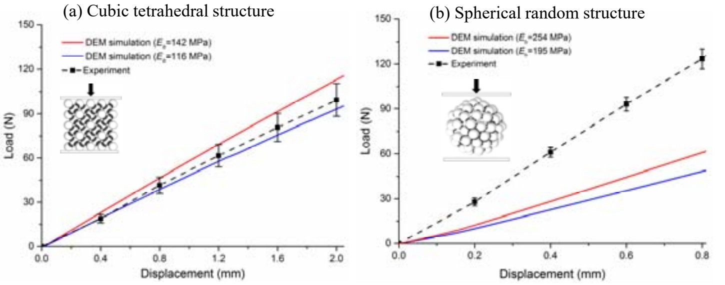
(a) Cubic tetrahedral structure (b) Spherical random structure

- DEM underestimation of compressive loads for spherical random structures attributed to
  - Different definitions of bond geometry.
  - Non-linear behavior of polymer bridge particle contacts.

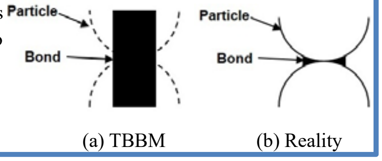

(a) TBBM (b) Reality

Summary

- Several well defined particle structures &bond properties were 3D printed.
- Experimental breakage results were obtained under different strain rates.
- Macroscopic agglomerate breakage experiments were compared with DEM simulation results to validate the newly developed TBBM contact model.
- DEM underestimated compressive load for spherical random agglomerates which attributed to TBBM bond geometry definition differences & non-linear polymer behavior.

Australian Government
Australian Research Council

International Fine Particle Research Institute

Flowability of Weakly Consolidated Powders

Alexandros Stavrou[1], **Colin Hare**[1], **Ali Hassanpour**[2]

[1]Department of Chemical and Process Engineering, Faculty of Engineering and Physical Sciences, University of Surrey, Guildford, Surrey, GU2 7XH, UK

[2]School of Chemical and Process Engineering, Faculty of Engineering, University of Leeds, Leeds, West Yorkshire, LS2 9JT, UK

1. Project brief

Measurement of unconfined yield strength of powders can be made with a variety of commercially available shear testing devices. Traditional flowability measurement devices have a number of short comings:

- Reproducibility of unconfined yield strength is greatly reduced at low stresses
- Or sometimes measurement is inconsistent with observed behaviour
- Materials found to be cohesionless may still have practical differences
- Generally the onset of flow is measured, which may not be a complete flow description

IFPRI seek to develop a theoretical understanding of flow of weakly consolidated and weakly cohesive powders

- Development of practical means of making measurement to support theory
- Results should be generalisable to a broad class of powders

2. Ball indentation

Many processes expose particles to very low consolidation stresses (<1 kPa), such as dry powder inhalers, feeders for packing and tableting machines and filling and dosing of powders in capsules. To address the aforementioned issue, the ball indentation technique was developed.

Ball indentation[1] is a method for assessing powder flow under low stresses and varying strain rates that requires only a very small amount of material. The experimental procedure comprises of three steps:

- A powder bed is consolidated to a desired stress
- The powder bed is penetrated by a spherical indenter, until a desired penetration depth has been reached
- The indenter is unloaded

Flowability is determined by calculating hardness (Eq. 1), which represents flow stress and is the resistance of a material to plastic deformation, from the force-displacement response of the bed (Fig. 1). Provided that the bed does not consolidate, hardness can be linked to the unconfined yield strength, which is derived by the commonly used shear testers, via the constraint factor (Eq. 3). Currently there is no understanding of how *C* varies with particle properties.

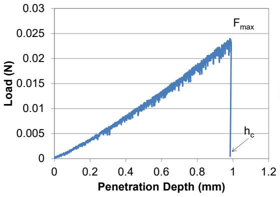

Figure 1. Force-displacement curve

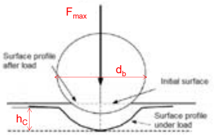

Figure 2. Bed surface profile

$$H = F_{max}/A \quad \text{(Eq. 1)}$$

$$A = \pi\left(d_b h_c - h_c^2\right) \quad \text{(Eq. 2)}$$

$$H = CY \quad \text{(Eq. 3)}$$

3. Powder flowability determination

For this research, five consecutive single sieve cuts of silanised glass beads, along with three inorganic powders; alumina CT800SG, limestone BCR 116 and titania, and three organic powders; maize starch, a sweetener (maltitol), and pea protein.

Powder flow behaviour was assessed using shear testing (FT4 Shear Cell) and ball indentation (criteria specified elsewhere[2,3]). Specifically, the unconfined yield strength (UYS) was measured at 2, 4, 6 and 8 kPa pre-shear normal stress.

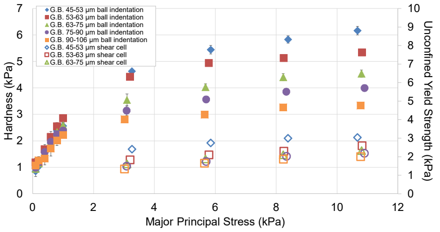

Figure 3. Silanised glass beads: hardness/UYS vs MPS

Figure 3-5 show the dependency of hardness and UYS on the major principal stress for all the materials tested. Both flow indices are observed to increase with applied stress, due to an increased packing fraction. The increase is sharper in the range of low stresses (<1 kPa). From Figure 3 it can also be seen that the smaller the particle size, the larger the exhibited hardness. This trend is clear among consecutive sieve cuts at high stresses, whereas at low stresses the difference is less clear.

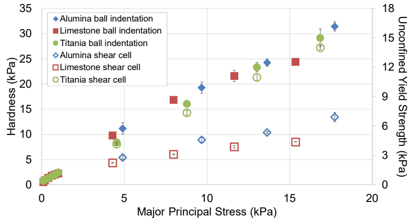

Figure 4. Inorganic powders: hardness/UYS vs MPS

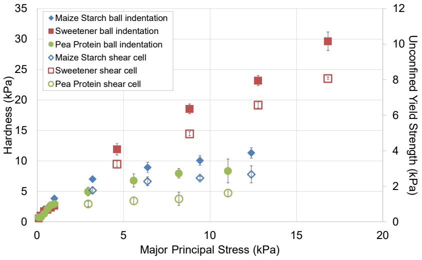

Figure 5. Organic powders: hardness/UYS vs MPS

4. Constraint factor & flow at low stresses

In order to use ball indentation to assess powder flow, it is important to be able to infer the unconfined yield strength from the measurement. Therefore the constraint factor, *C*, (Eq. 3) needs to be established in order to relate the hardness to the yield strength. To quantify the constraint factor, unconfined yield strength measurements by the shear cell are used. *C* is found to be almost constant for all the materials tested (Figs. 6-7). Also, it is observed that it increases as particle size decreases, as shown in Figure 6. However the span of the size distribution appears to have limited effect.

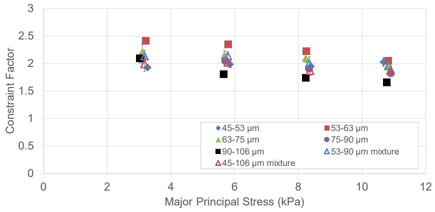

Figure 6. Silanised glass beads: constraint factor vs MPS

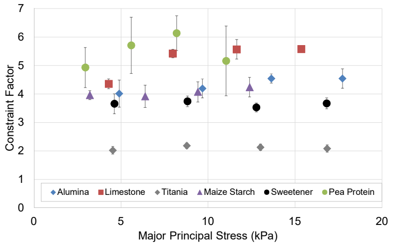

Figure 7. Inorganic and organic powders: constraint factor vs MPS

In order to calculate the unconfined yield strength at low consolidation stresses, it is assumed that the constraint factor remains constant at low stresses. Using the hardness values, the unconfined yield strength is calculated at low stresses, showing that an extrapolation of higher stress shear cell results would lead to an overestimation of UYS (Figs.8-10).

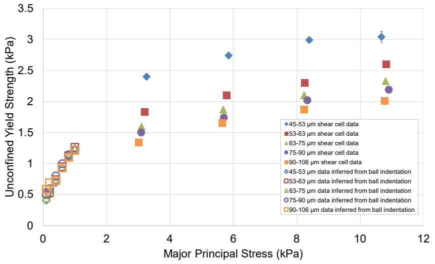

Figure 8. Silanised glass beads: UYS vs MPS

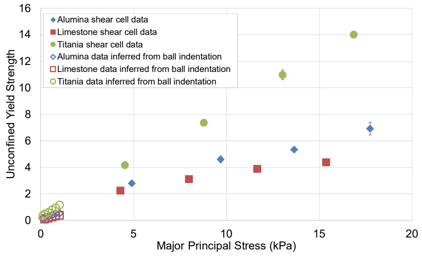

Figure 9. Inorganic powders: UYS vs MPS

Shear Cells usually fail to provide reliable results at low consolidation pressures[4]. For one of the glass bead single sieve cuts, the 45-53 µm, shear tests with acceptable repeatability were carried out using the FT4 Shear Cell down to 0.1 kPa pre-shear normal stress. The shear cell results follow a similar trend to those inferred from ball indentation in the low stress region (Fig. 11), however the shear cell appears to underestimate the unconfined yield strength.

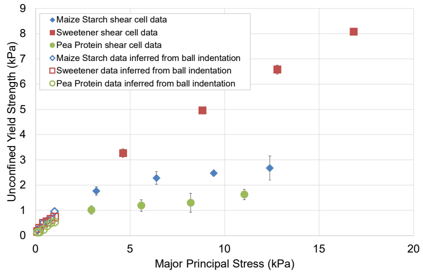

Figure 10. Organic powders: UYS vs MPS

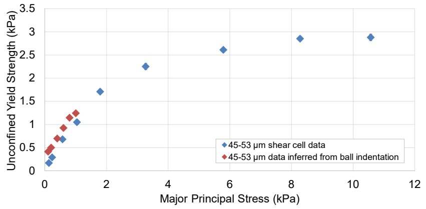

Figure 11. Shear cell and ball indentation UYS correlation

5.Conclusions-future work

- Ball indentation results exhibit very good reliability at both high and low stresses
- Ball indentation provides a very good sensitivity of hardness to particle size
- All the materials exhibit a sharper increase of hardness in the region of low stress, with it being more pronounced in the case of silanised glass beads and the three food powders
- For the materials tested, the constraint factor is found to be approximately constant throughout the range of stresses tested, except for limestone and pea protein
- Constraint factor is found to increase as particle size is decreased
- In the case of silanised glass beads, the unconfined yield strength measured in the shear cell and inferred from ball indentation correlates well at low stresses

Future work:

- Two talc powders and three copper powders with different particle shape (Fig. 12), are going to be tested to further assess the influence of particle shape on the constraint factor

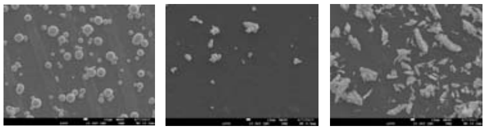

Figure 12. SEM micrographs of three copper powders

- Glass beads will be silanised with different functional groups and tested in order to assess the influence of surface energy on the constraint factor
- Shear cell and indentation results will be compared to uniaxial compression tests. Preliminary results for the sweetener are shown in Figure 13.

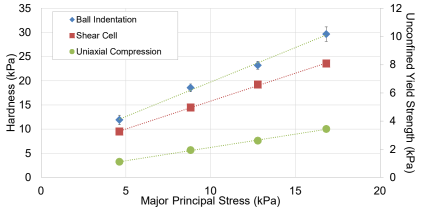

Figure 13. Comparison of ball indentation, shear cell and uniaxial compression results for sweetener

- DEM will be utilised to investigate the behaviour of *C* at low stresses

6. References

[1] Hassanpour, A. & Ghadiri, M., 2007, Characterisation of Flowability of Loosely Compacted Cohesive Powders by Indentation, *Particle and Particle Systems Characterization*, **24**(2), 117–123.

[2] Zafar, U., Hare, C., Hassanpour, A., Ghadiri, M., 2017, Ball Indentation on Powder Beds for Assessing Powder Flowability: Analysis of Operation Window Powder Technology, *Powder Technology*, **310**, 300-306.

[3] Pasha, M., Modelling of Flowability Measurement of Cohesive Powders Using Small Quantities, University of Leeds, *PhD Thesis*, 2013.

[4] Schulze, D., 2008, Powders and bulk solids. Behaviour, Characterization, Storage and Flow. Springer.

Contact: a.stavrou@surrey.ac.uk (A. G. Stavrou), c.hare@surrey.ac.uk (C. Hare), A.Hassanpour@leeds.ac.uk (A. Hassanpour)

UNIVERSITY OF HOHENHEIM
Institute of Food Science and Biotechnology
Process Engineering and Food Powders

International Fine Particle Research Institute

Powder Structure Control

Fluid bed agglomeration, simulation and overview

J. Harnacke, R. Kohlus

Introduction

Granule structure of homogeneous (no porosity) and porous particles has been summarized by particle-particle distance of non-soluble primary particles. Porous material was generated by a sinter method as well as fluid bed agglomeration: Strength and dissolution were investigated as powder properties.

Additionally dissolution was investigated by a simulation approach, allowing detailed assessment of single particle behaviour. Dissolution of highly pre-dissolved particles varies very much. Particle strength, especially of fluid bed agglomerates was tested by an impact test. An influence of the ratio of primary particle size to granule size was not found.

Random close

Granules with different particle-particle distances but same packing densities were generated to investigate the main influencing factors.

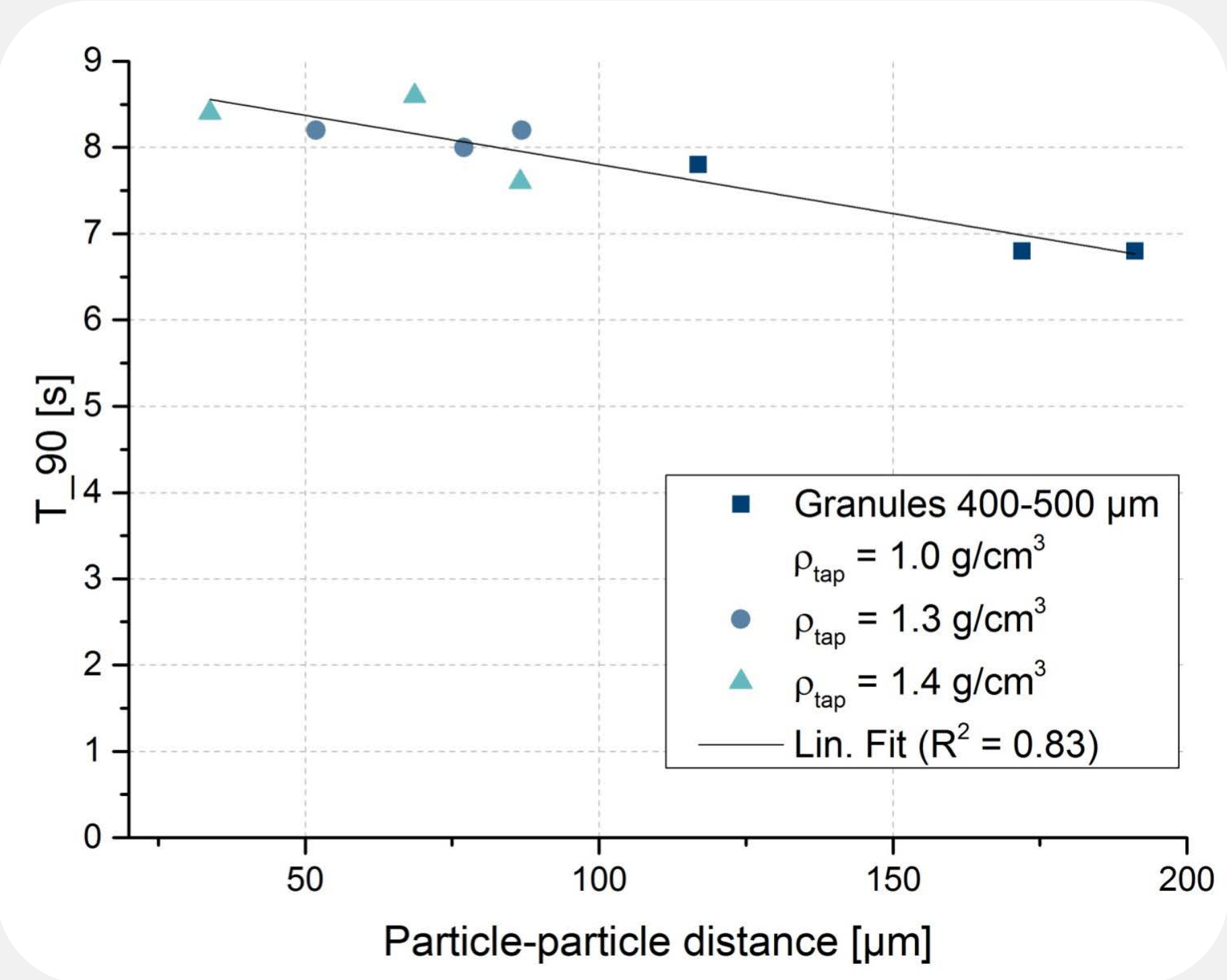

high particle-particle distance
→ large pore space of dissolving material
→ fast dissolution

Structure description

Structure measured by volume fraction, CVF and CLD of disperse and continuous phase.
(Covariance function, chord length distribution)

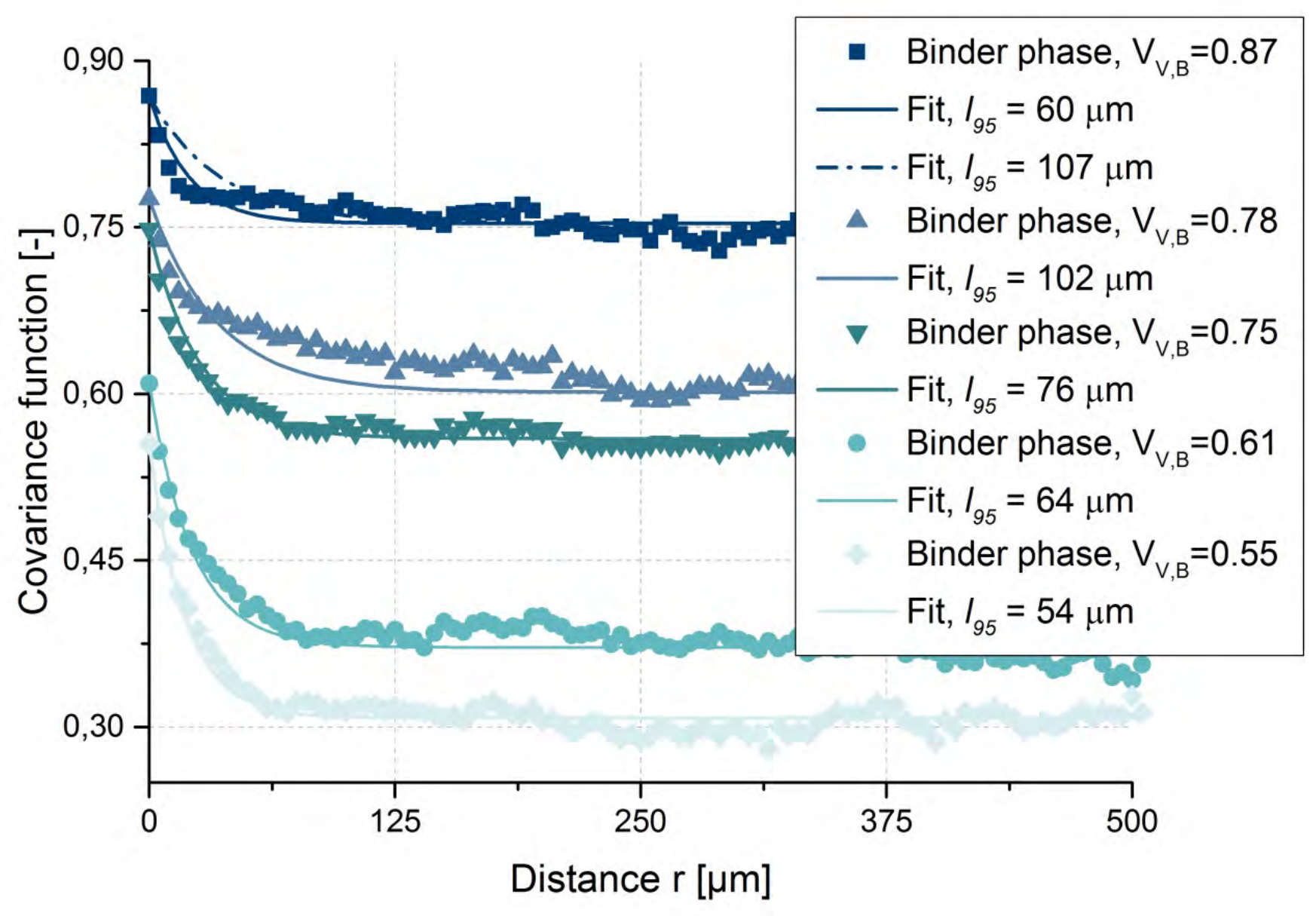

Random loose

Structure of powder with high degree of porosity was generated using a sintering technique and single particle strength was measured (Weibull Approx.)

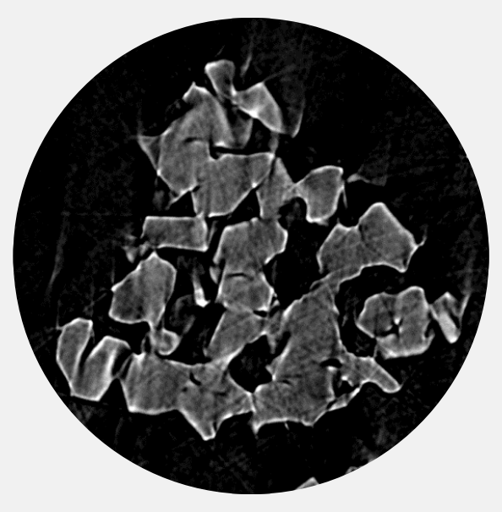

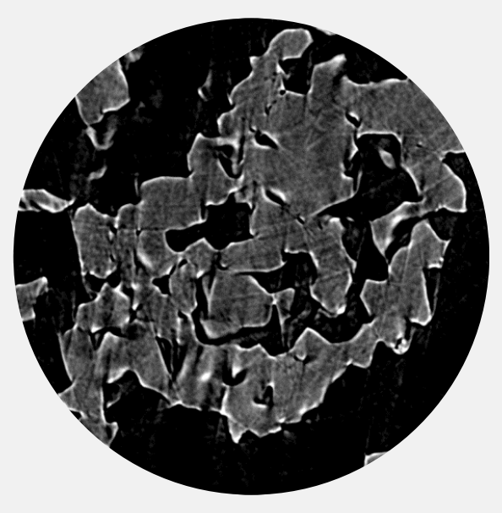

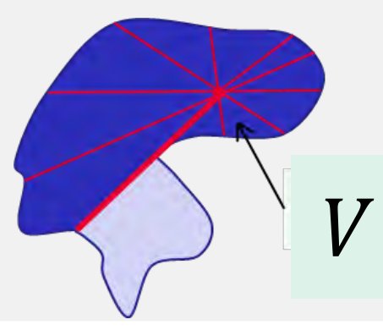

$$V^* = \frac{\pi}{3}\overline{l^3}$$

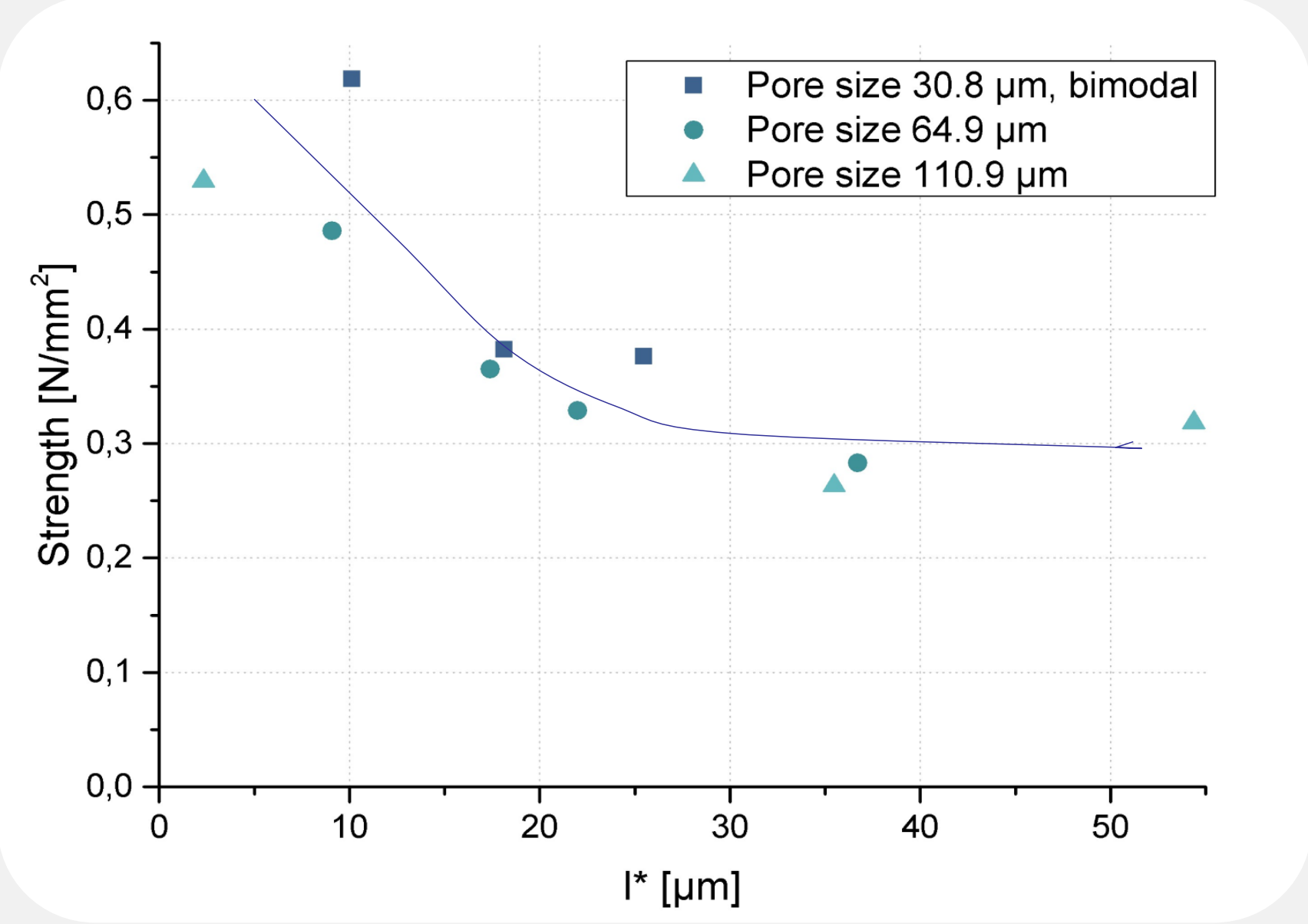

High water uptake
→ higher no. of bridges
→ more stable granules

Prediction of structure descriptors

Particle-particle distance calculation was used as structure measure for dissolution characterization.

$$d_{pp} = d_{3,0} \cdot \left(\sqrt[3]{\frac{\phi_{max}}{\phi_c \cdot \rho_{tap}/\rho_{solid}}} - 1 \right)$$

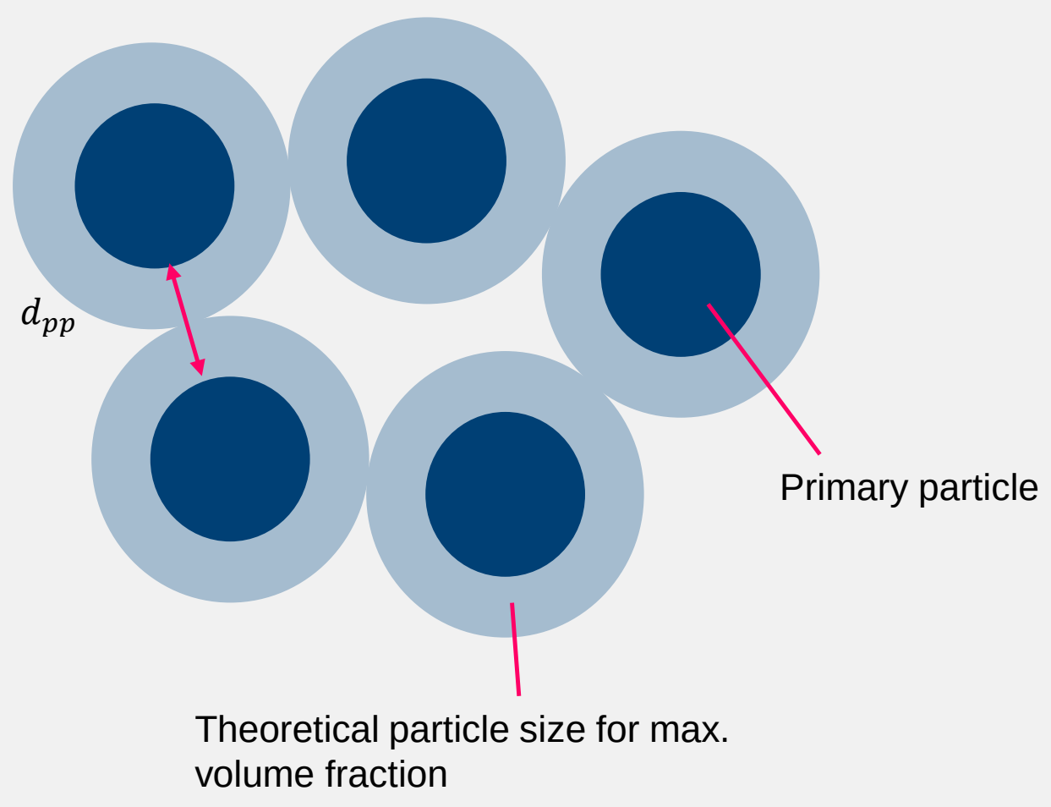

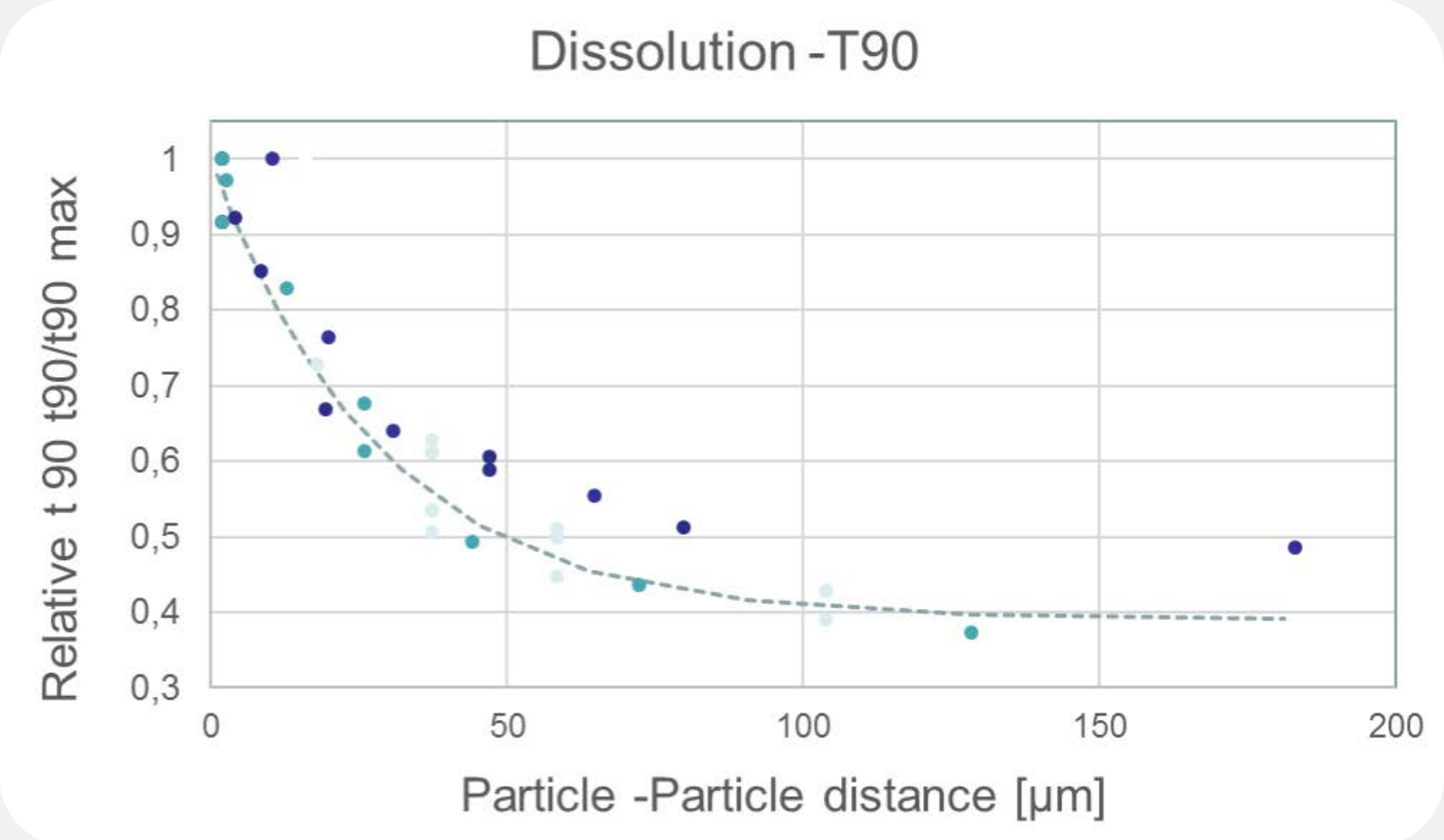

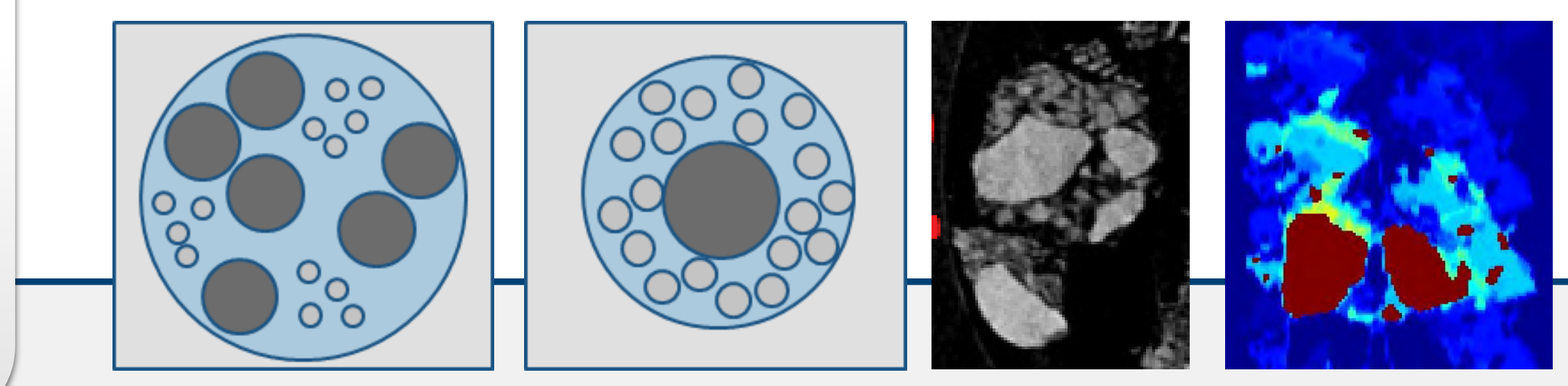

Simulation

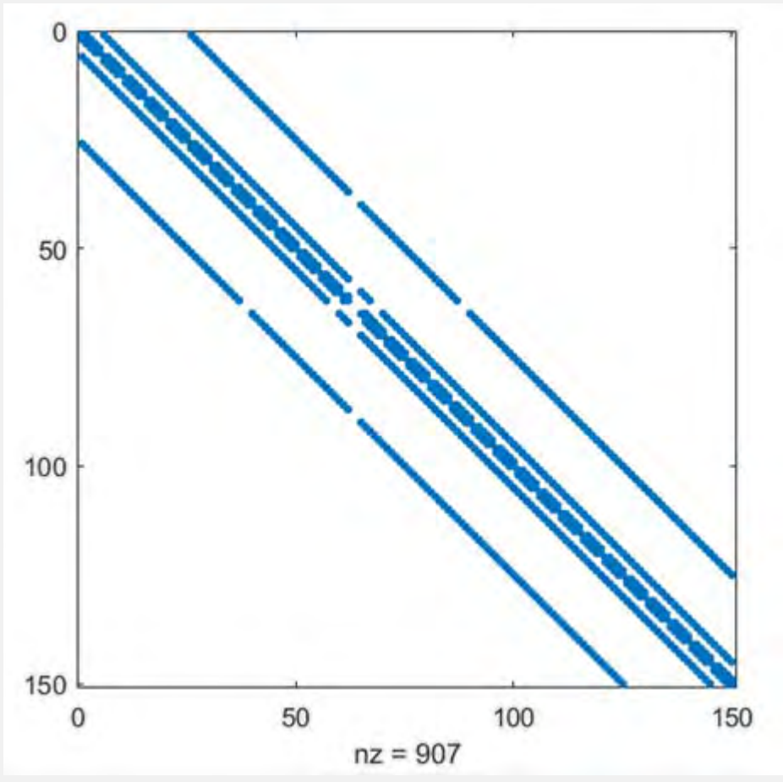

A “Volume of fluids” VOF program has been set up to simulate the dissolution of single structured particles based on a finite differences scheme. The structure is captured by 3d- XRT images.

Summary

Powder structure was characterised by stereological methods, i.e. covariance function. Particle size distribution and phase volume ratio define the stochastical particle structure for most granulation techniques. The covariance function allows to predict the size distribution of free volume between the particles and related effects like capillary pressure curve. Strength and dissolution behaviour scale with average particle –particle distance.

39th IFPRI Annual General Meeting, 18th-22nd June 2016, Philadelphia, USA

International Fine Particle Research Institute

Quantitative Prediction of Segregation at Process Scale

Joseph J. McCarthy

Department of Chemical and Petroleum Engineering University of Pittsburgh, Pittsburgh PA 15261

ABSTRACT: Segregation rate models hold promise for scale-up via continuum-level analysis using device-specific transport equations. Our approach involves both a unique experimental"equilibrium" between mixing and segregation via flow perturbations as well as a focus on models that are written expressly in dimensionless form with an aim at transparent scale-up. We are using our experimental segregation validation framework both to benchmark existing segregation rate models as well as to test our new and developing models. Using our scaling approach we have recently established the first analytical connection between density-based segregation to granular rheology. This model is based largely on first principles and fits data from a variety of boundary conditions, density ratios, shear rates, gravitational conditions, and material properties. Moreover, we have begun building complementary segregation models for size, shape, and cohesive segregation and have validated our shape model.

Project Brief

- Identify **material and process parameters** that control the *extent* of powder segregation
- Develop **quantitative models that predict** segregation
- **Validate** models with appropriate experiments
- Demonstrate that the models are applicable to **full-scale** processes
- Add'l considerations: (1) Cohesive powders, (2) Particle shape

Competing Timescales

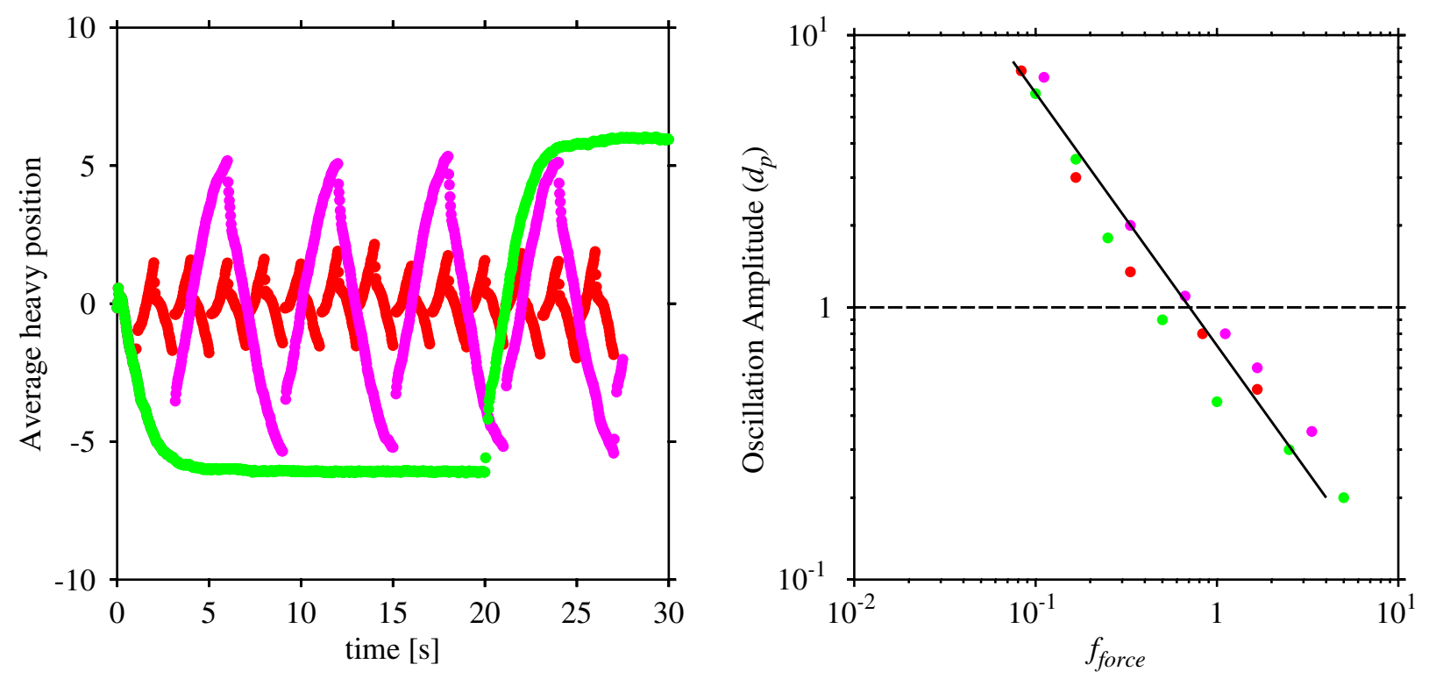

- "Asymptotic" segregation ↓ with ↑ forcing frequency
- If $t_{seg} \approx t_{forcing}$ balance of rates

Evaluating Models for Segregation

Density Segregation

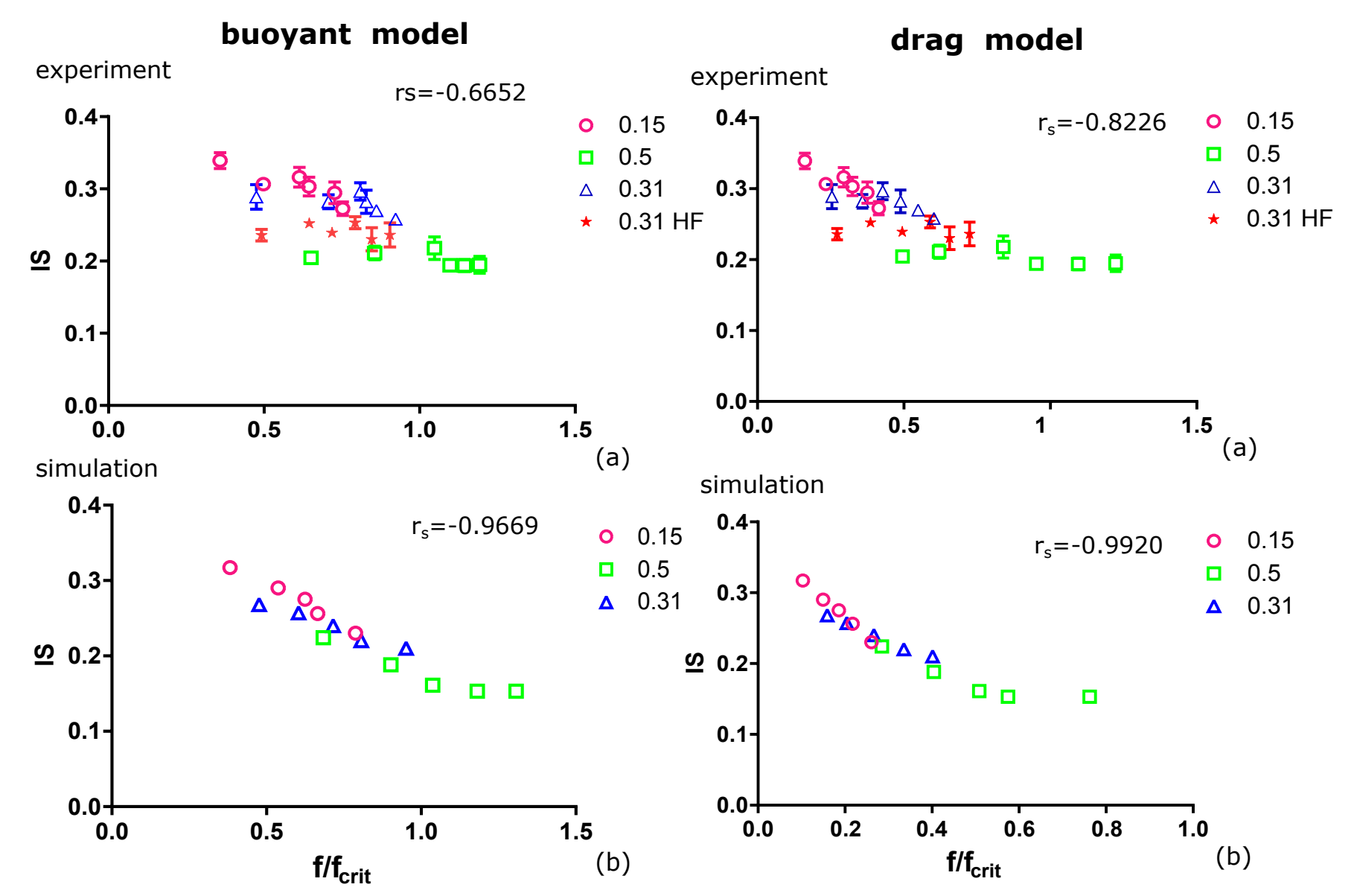

Size Segregation

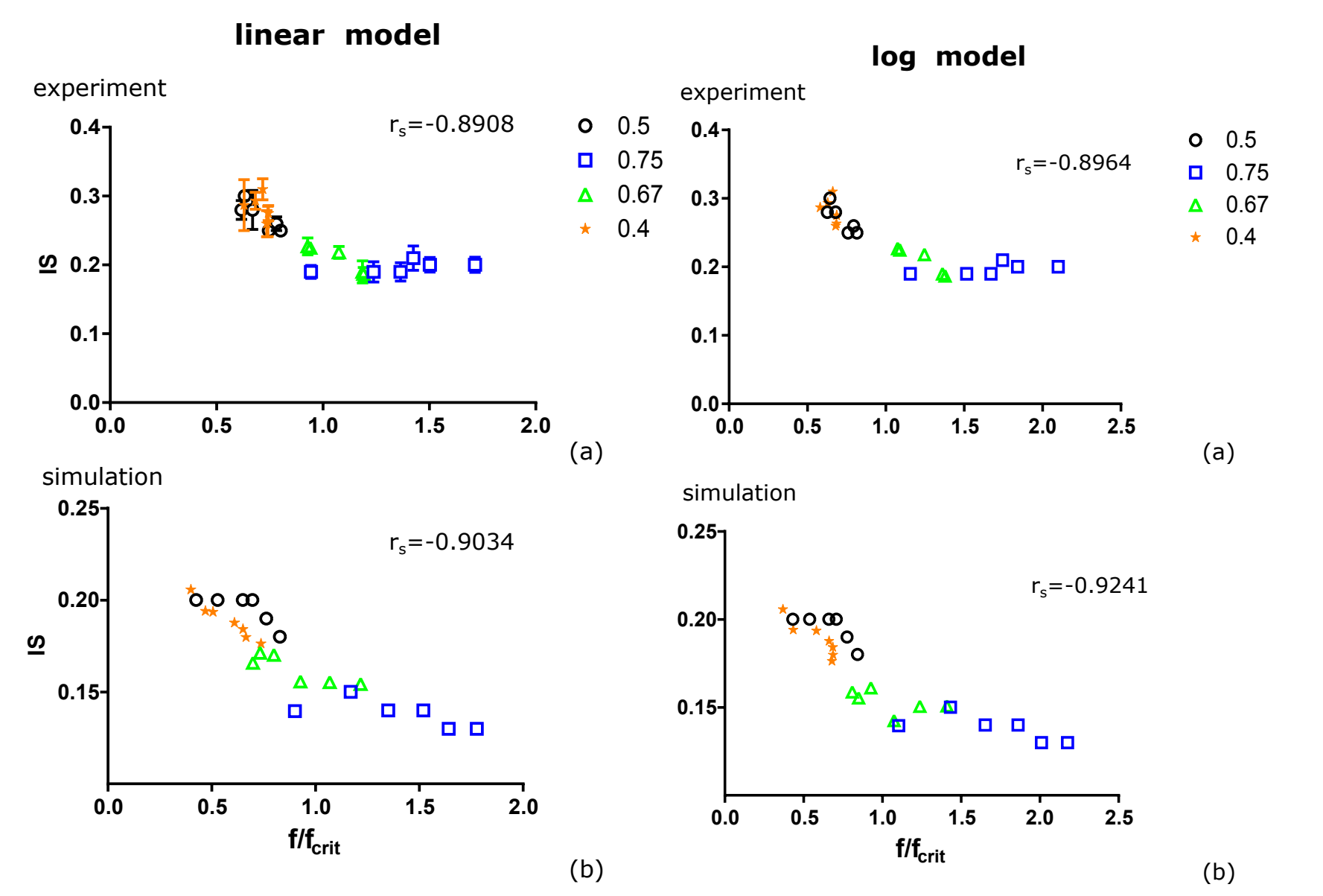

- "Proper" model will yield monotonic change in IS vs f/f_{crit}
- r_s for quantitative measure (1 → monotonic)

Building New Models for Segregation

Direct Forcing for Rigorous Segregation Testing

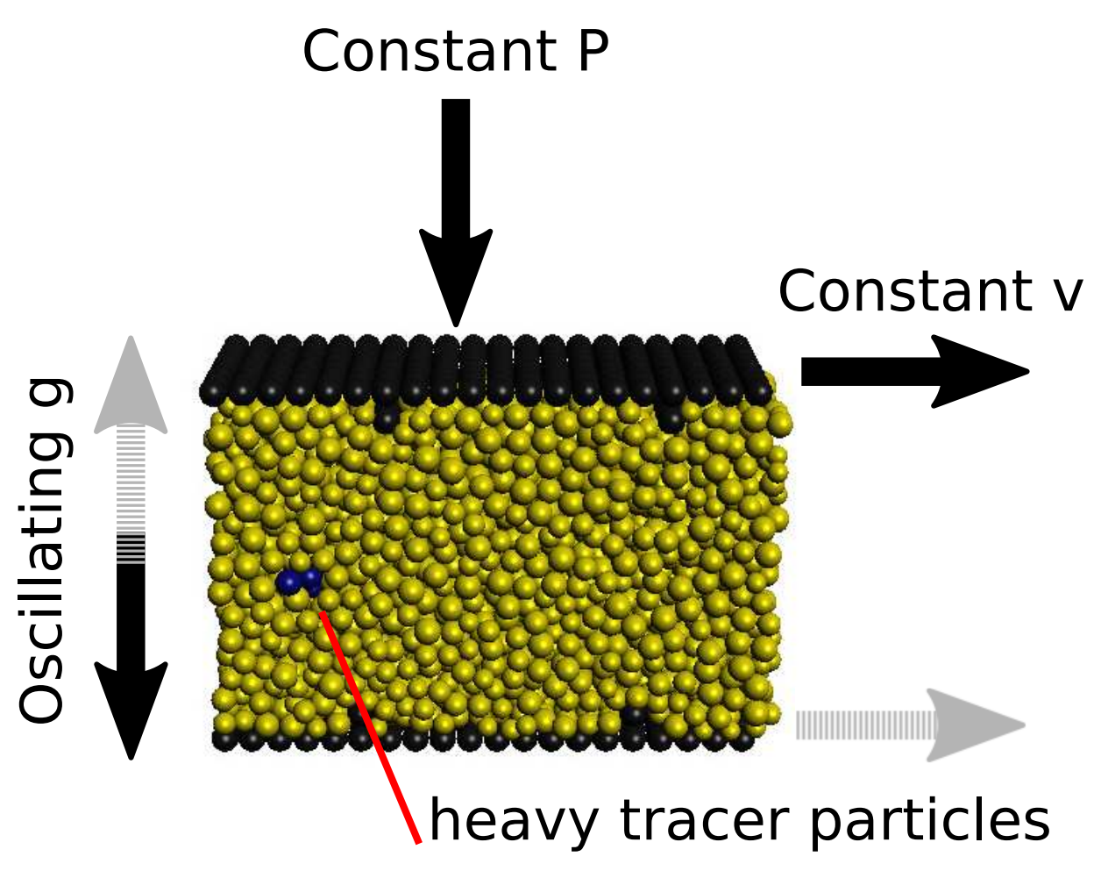

- Vary density ratio
- Vary shear rate (velocity)
- (Mostly) Constant pressure BC

Density Segregation – Built for Scale-Up

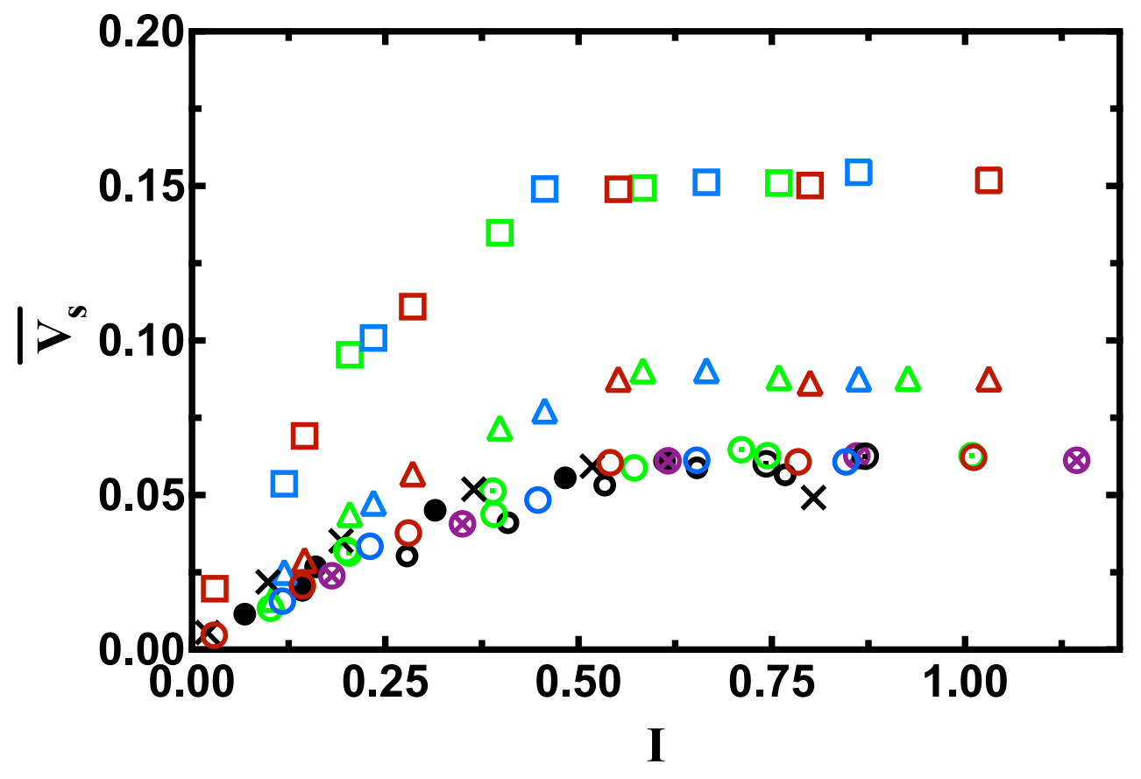

- Dimensionless segregation rate: $\bar{v}_s = \frac{v_s}{\sqrt{d_p g}}$
- Dimensionless "flow" parameter: $I = \dot{\gamma} d_p \sqrt{\rho/P}$
- Collapses results for different d_p, $\dot{\gamma}$, g, and BC's (P and CV)

Interesting Density Ratio Dependence

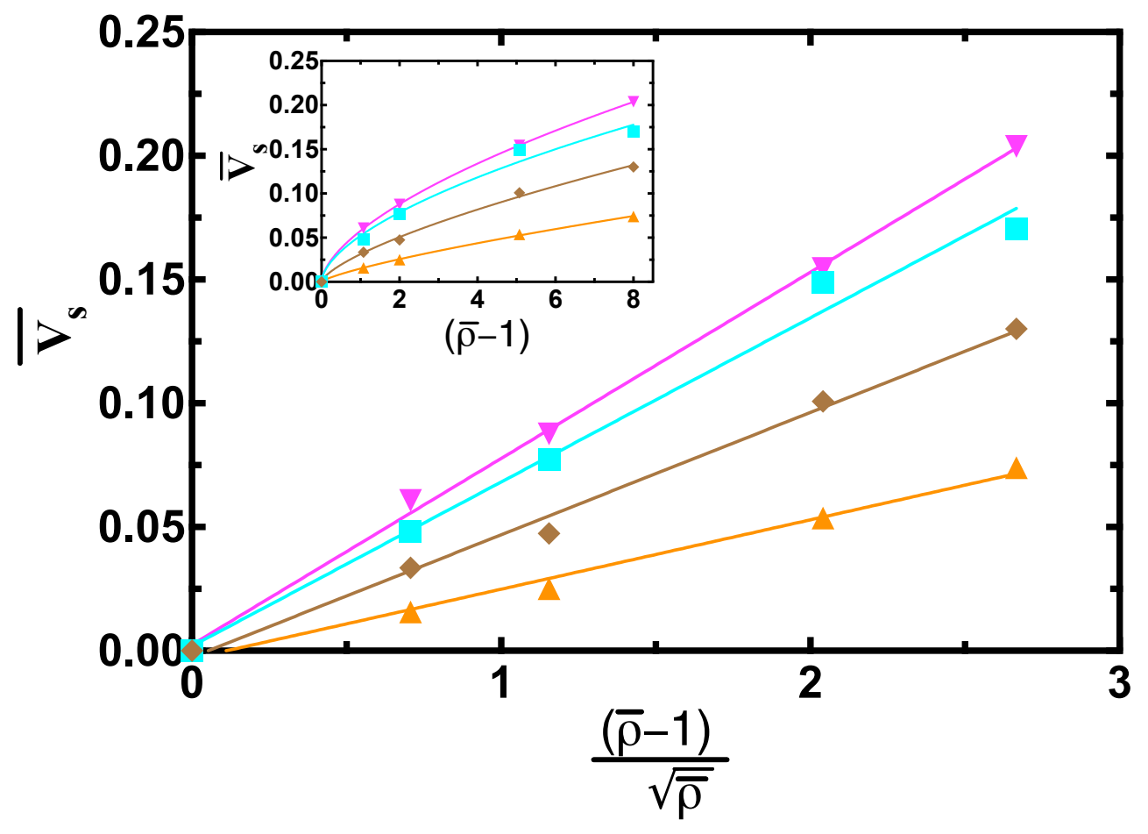

- "Extra" density dependence results from "added mass" from particle collisions (energy balance)

Origin of Our Scaling

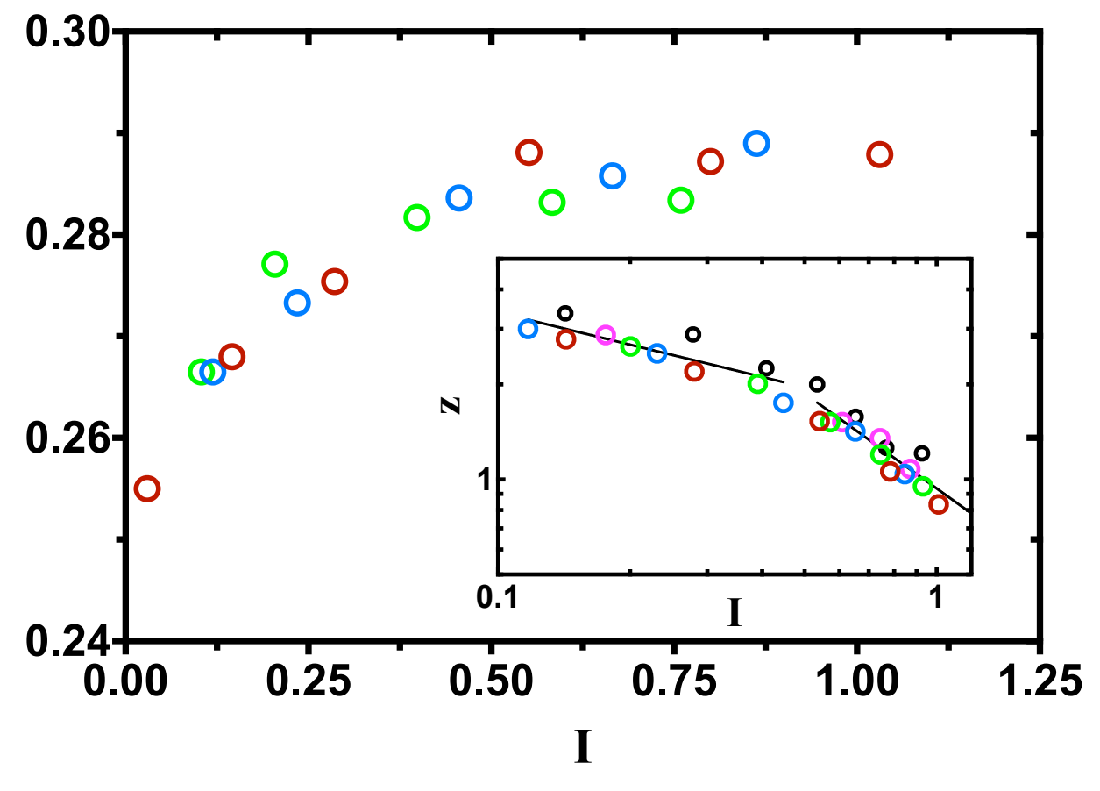

- Force balance: $0 = F_w - F_b + F_d$
- Solve for v_s: $v_s = \frac{g d_p^2 (\rho_h - \rho_l)}{\beta_s \eta}$
- Scaling for η: $\eta \sim \frac{\rho_h g d_p^2}{v_o \left(\frac{\rho_h}{\rho_l}\right)^{1/2}}$, where v_o is a (pre)-collision velocity

A Novel Rheology-Focused Density Model

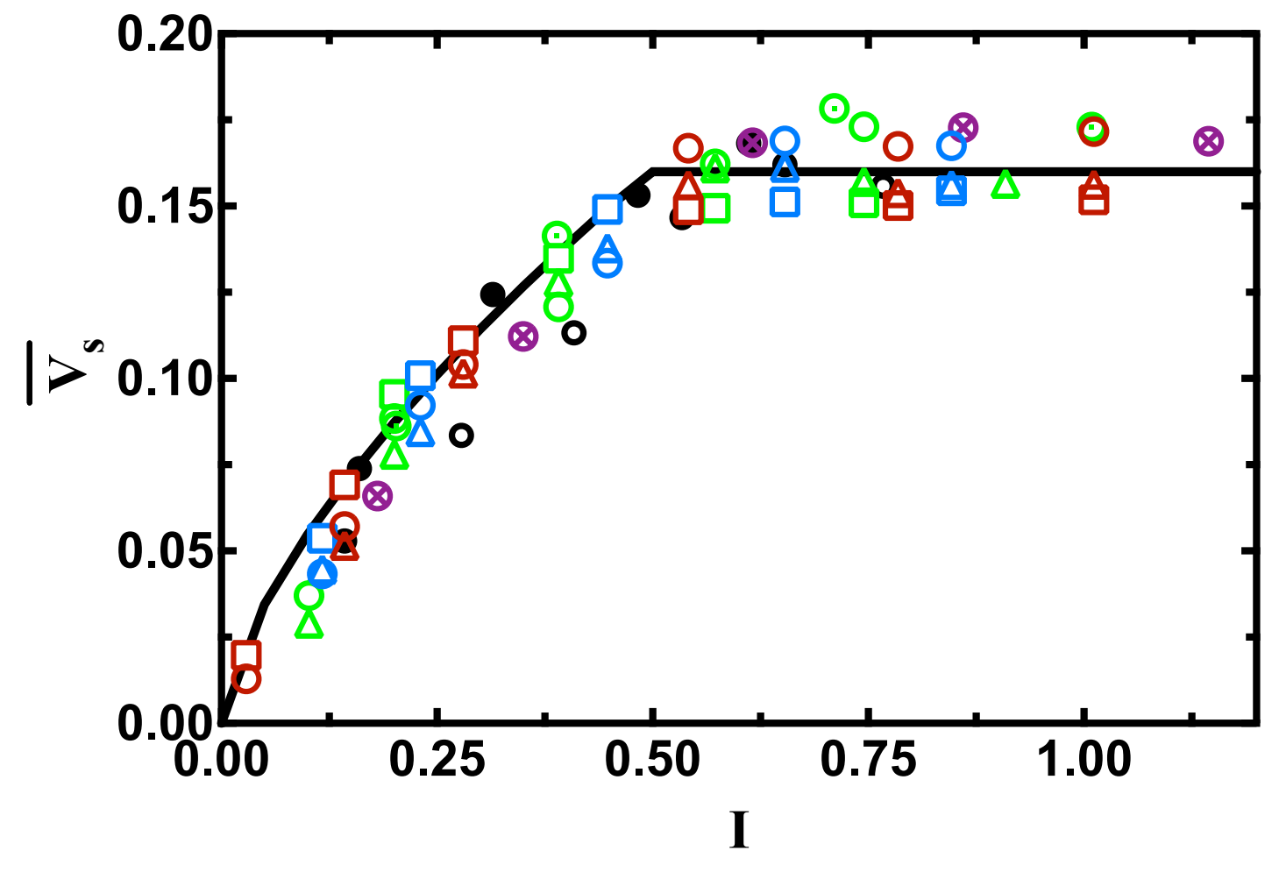

- Taking v_o to come from "frustrated free-fall" yields:

$$v_o \sim (\sqrt{d_p g}) z \dot{\gamma} t_c = (\sqrt{d_p g}) z I$$

- Combining scaling: $\bar{v}_s = \frac{v_s}{\sqrt{d_p g}} = \frac{z(\bar{\rho}-1)}{\beta_n \sqrt{\bar{\rho}}} I$
- Fits all data with only "fitting" parameter is $\beta_n = \frac{1}{6}$

Next for Density

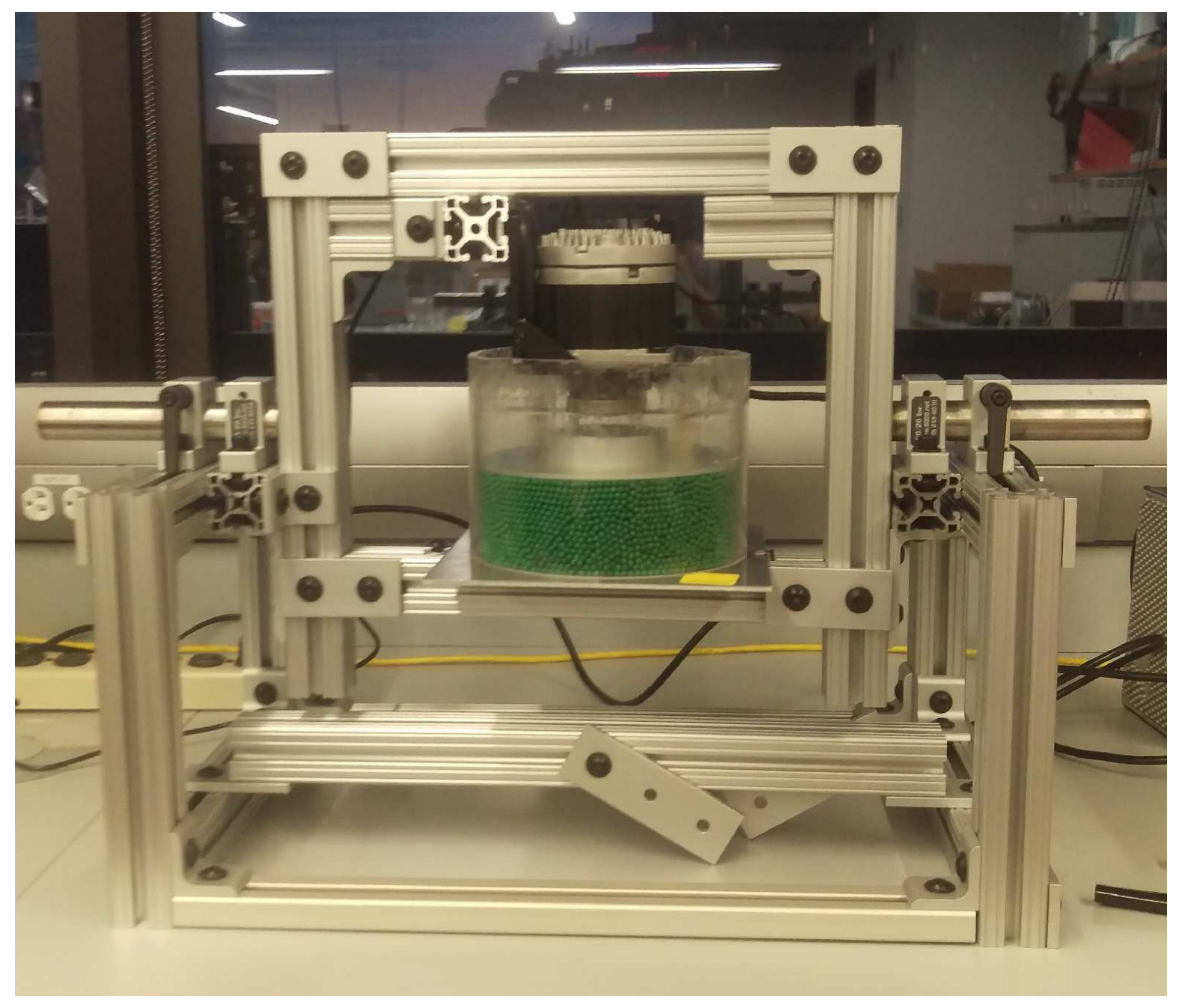

- Experimental apparatus for continuous shearing
- Can be run in both "perturbation mode" and traditional shear

New Directions

Testing Size Segregation

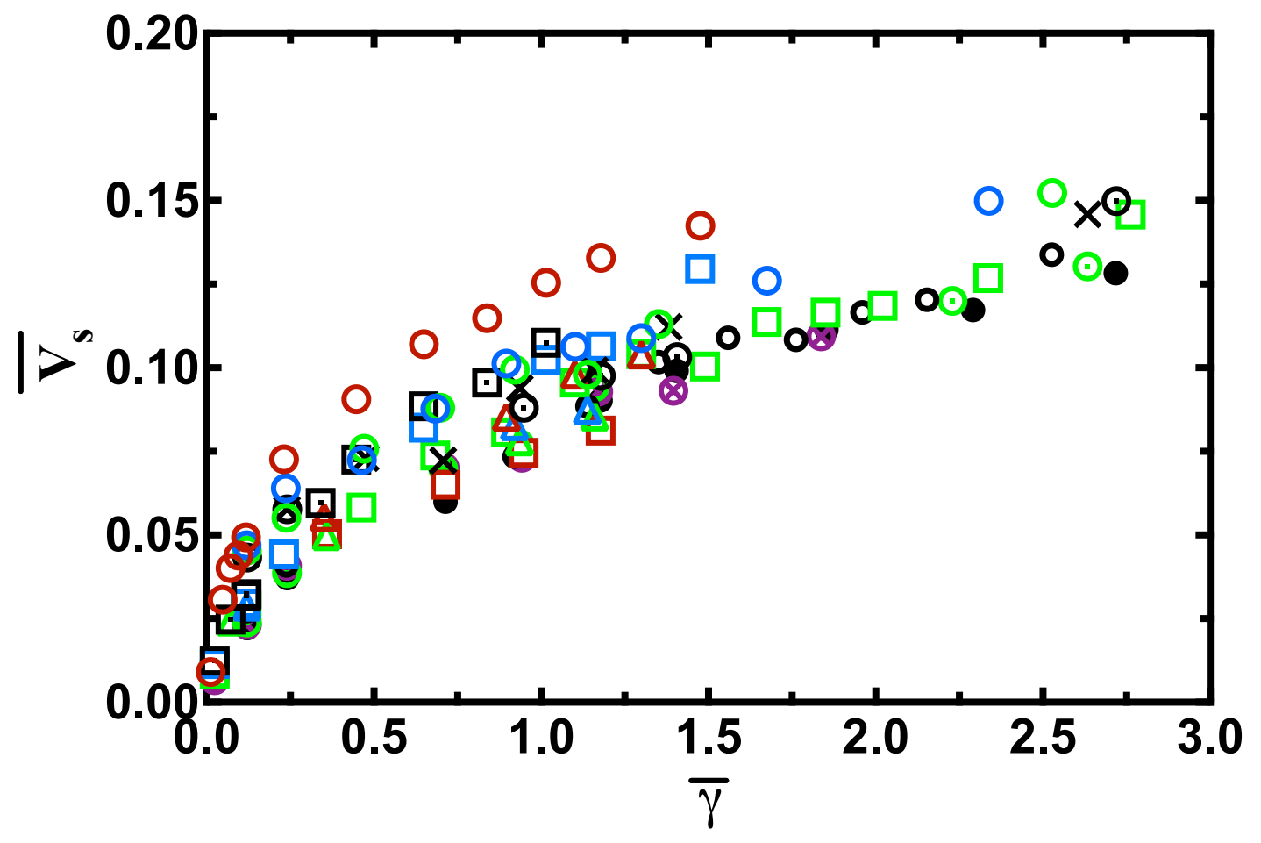

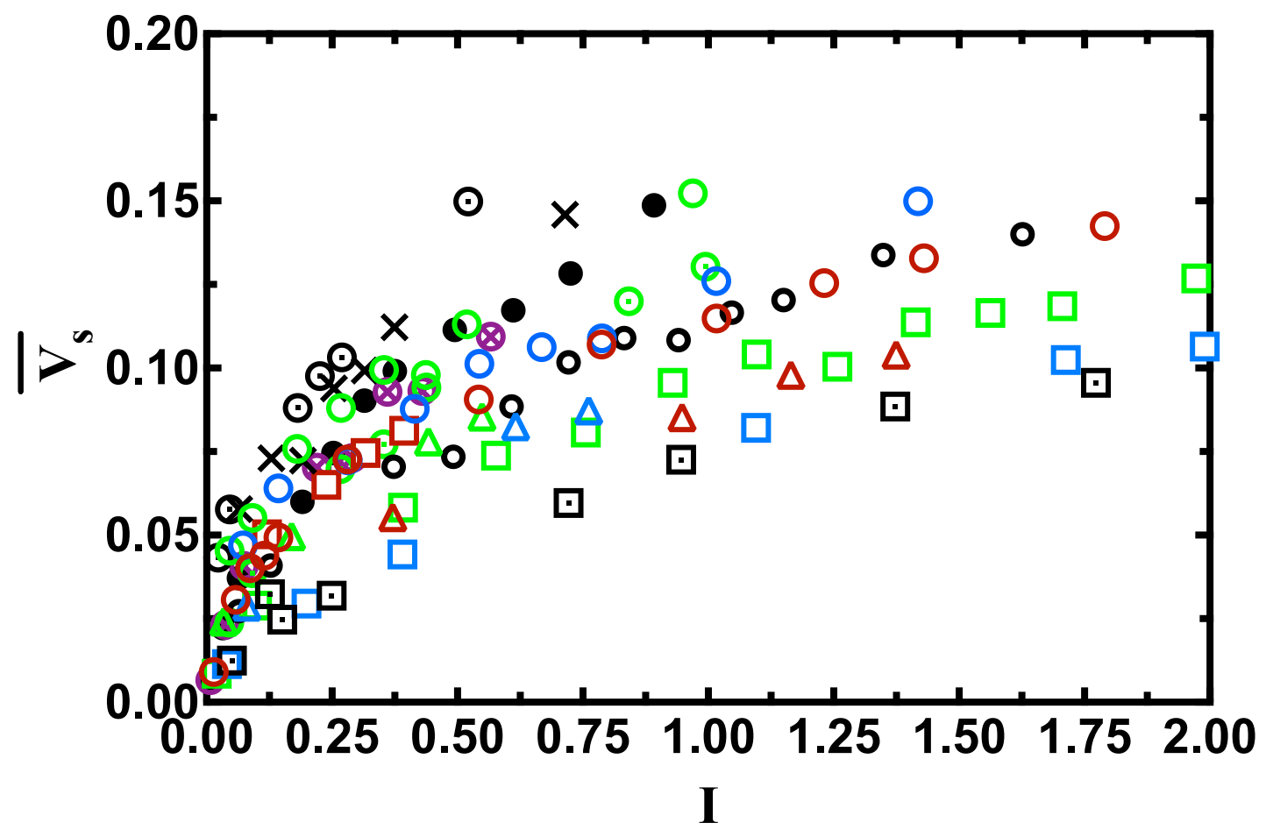

- Results are not linear with *either* $\dot{\gamma}$ or I
- Clearly we are missing some other rheological effect ...
- New modeling efforts are promising (See Student Poster session)

A **Proposed** Approach for Shape Segregation

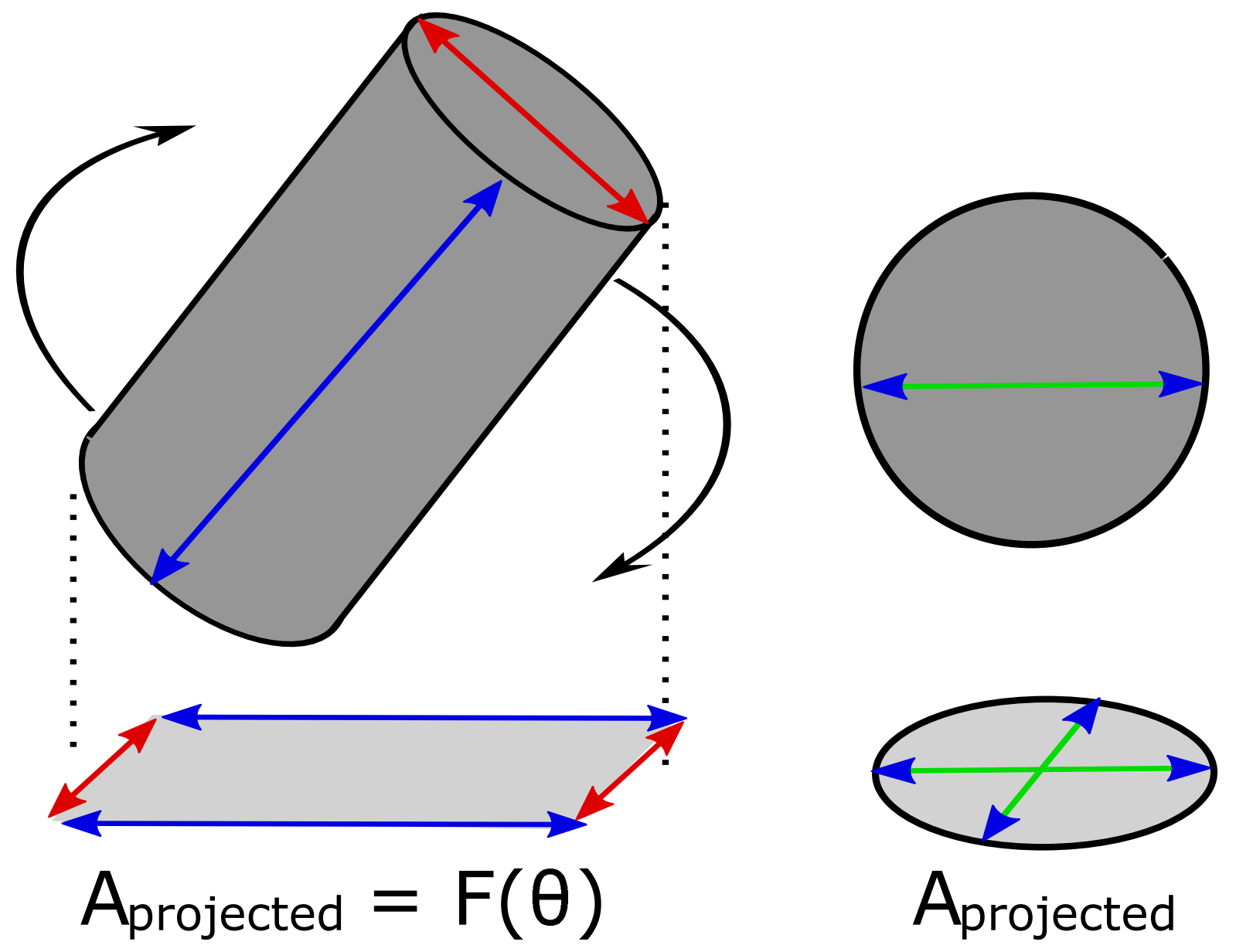

- If particles are able to freely rotate:

$$A_{eff} = A_{avg_\theta}$$

- Use this approach to predict segregation direction

Experimental Work on Shape Segregation

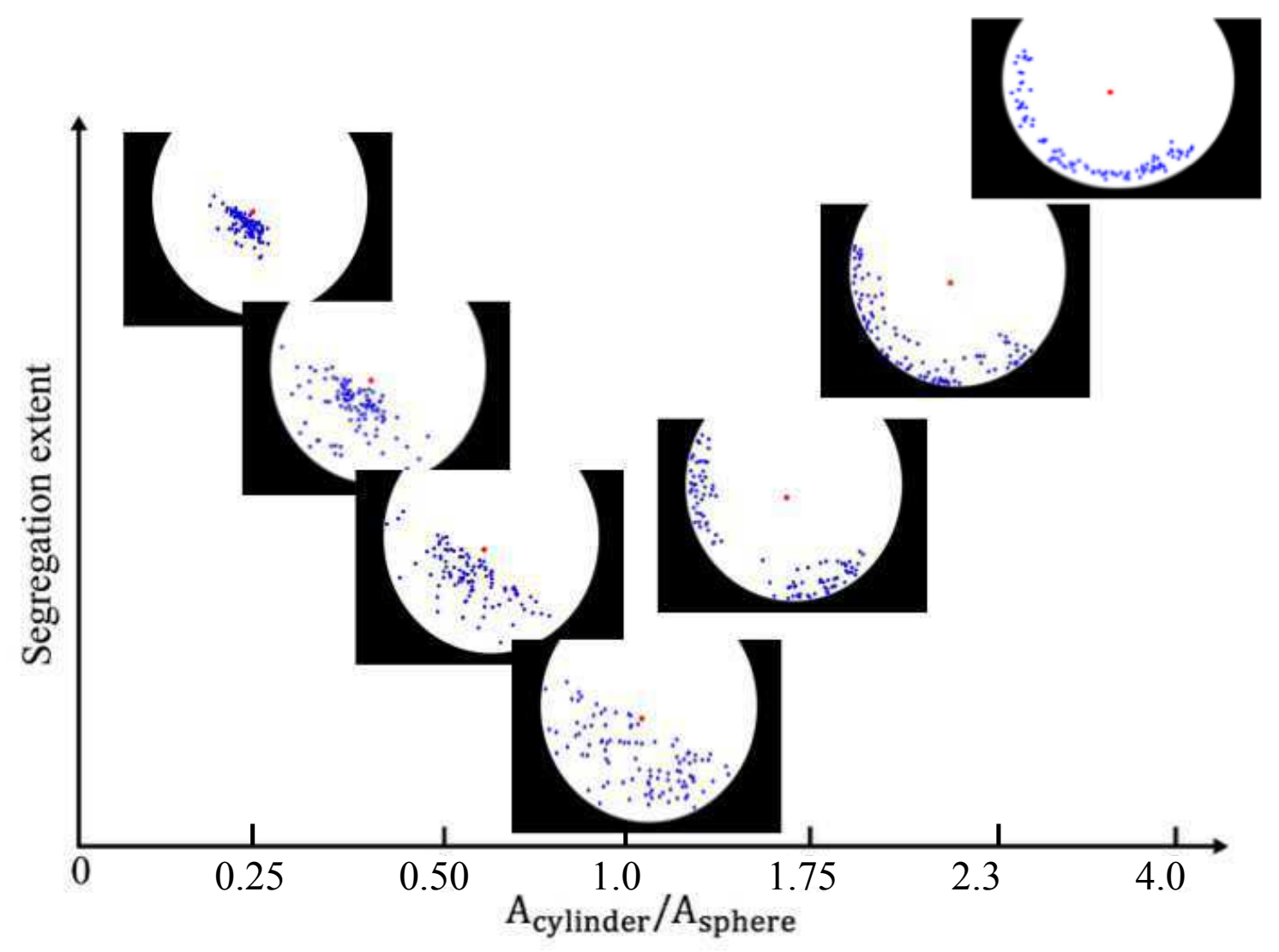

Cohesive Effects on Segregation Rate

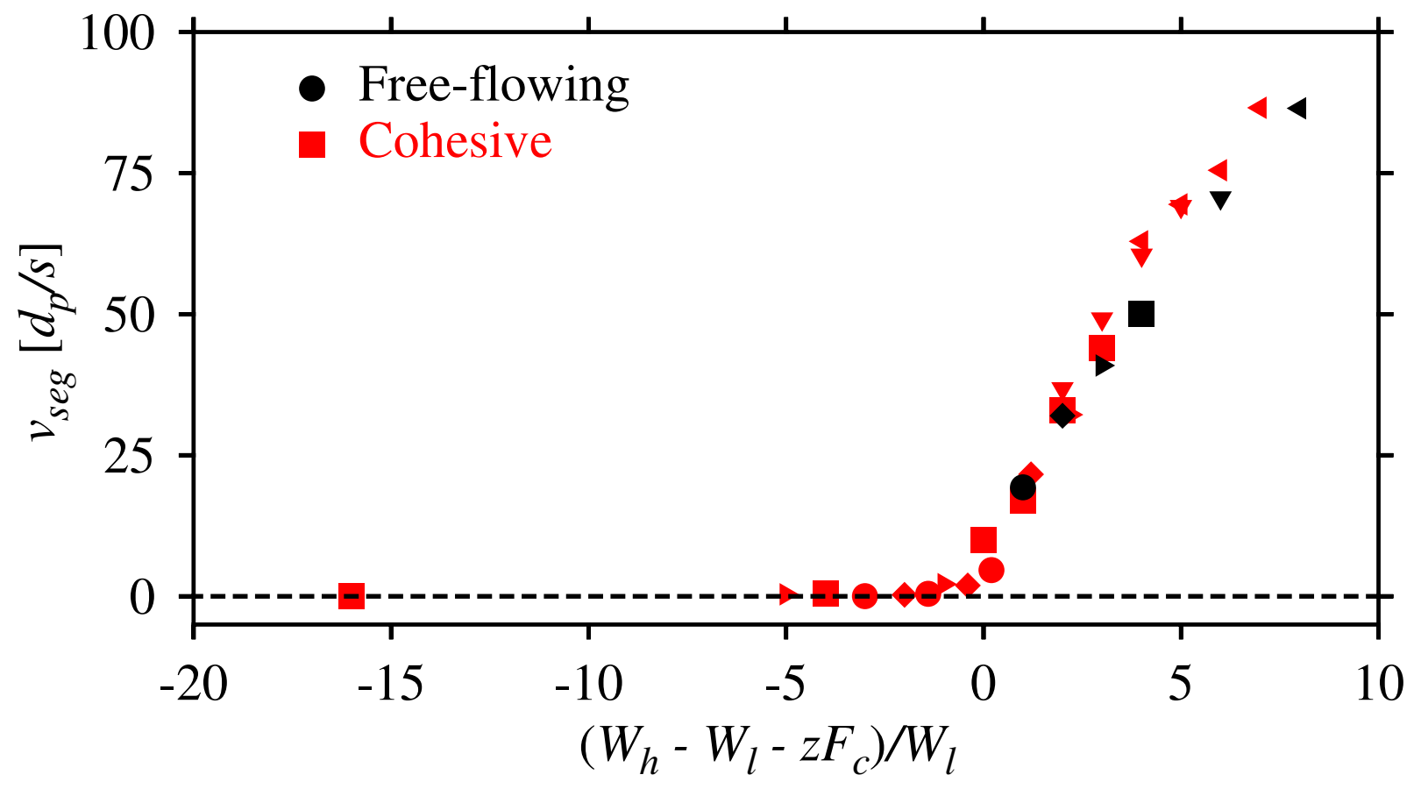

- Proposed model matches "new" model well
- Neither have been tested experimentally
- Segregation control framework should (finally) make this "easy"!

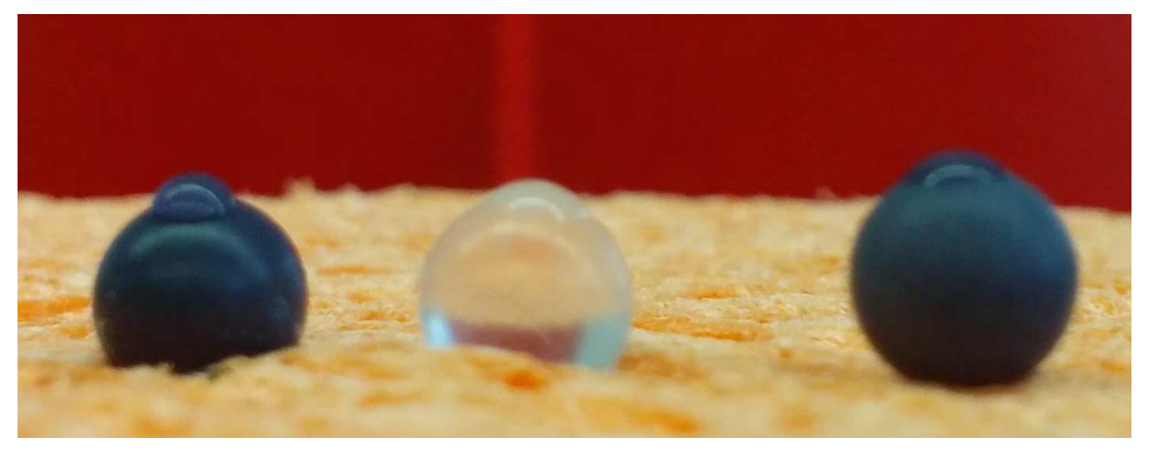

- Changing density → changing wetting
- Use TEOS to build a "silica skin"
- Further surface modification allows additional control

What's next?

- Run experiments with the direct forcing apparatus
- Perform cohesion experiments/simulations (in baffled tumbler and direct forcing)
- Perform shape segregation simulations (to compliment our experiments)
- Test multi-modal size and density (and mixed-mode) segregation in direct forcing

A Holistic Approach for the Model-based Control of Crystal Size, Shape and Purity in Integrated Batch and Continuous Crystallization - Wet Milling Systems

Botond Szilagyi, Zoltan K. Nagy

Purdue University, Davidson School of Chemical Engineering, West Lafayette

Specific aims. This project aims to develop and provide the first proof-of-concept simulation and experimental demonstration of a real-time implementation of a full population balance model based nonlinear predictive control approach for batch and continuous crystallization processes integrated with wet milling and classification/recycle system, in order to achieve desired crystal size and shape distribution. Additionally the effects of impurity/additive mixtures on the size, shape and crystal purity distribution will be incorporated in the model.

Model and soft-sensor development

Implementation efficiency – the *CrySiV function*

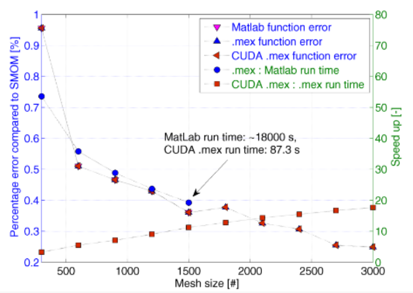

Soft-sensor design

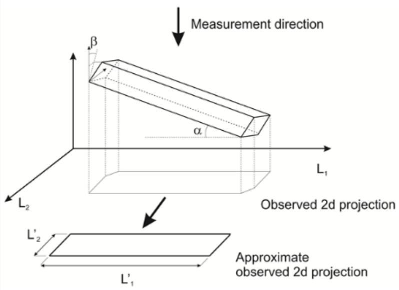

- High performance, ***GPU accelerated*** implementation of the high resolution finite volume method (HR-FVM) ***for 1D and 2D*** crystallization processes
- Soft sensor: based on random projection of pre-determined crystals (crystal dimensions used in the FVM solution)
- Mapping ***all*** possible chord lengths and aspect ratios of ***all*** possible projections (***off-line calculation***)
- ***Weighted summing*** of individual crystal's CLDs and ARDs to generate the CLD and ARD of the crystals population (***on-line calculation***)
- Estimation of measurable AR of a crystal population (PVM-soft sensor) from mean crystal size data.

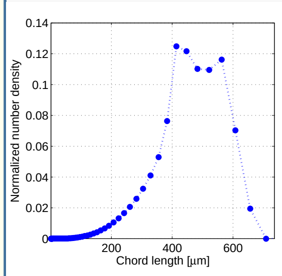

Simulated CLD (2D CSD)

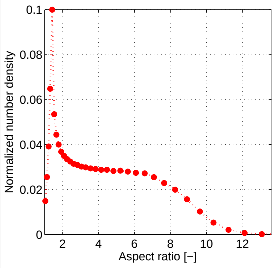

Simulated ARD (2D CSD)

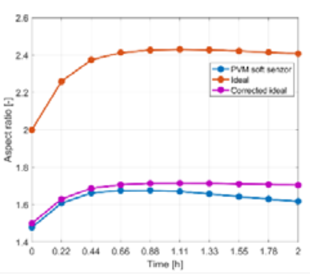

Mean AR calculation (2D CSD)

CrySiV 1.2

simulating crystallization easier

crysiv.github.io

Integrated system optimization

Integrated system, 1D PBM

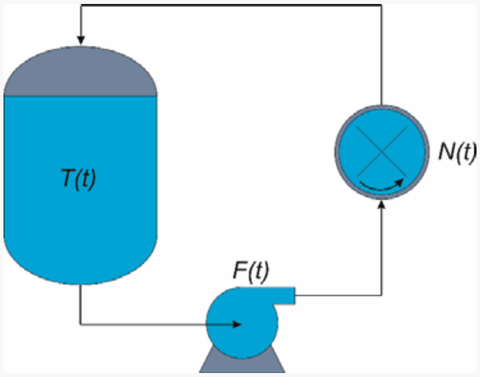

Numerical details

Accuracy	CFL	Mesh size	Compute platform
High	CFL < 0.3	N > 1000	CPU + GPU
Moderate	CFL > 0.3 CFL < 0.5	N > 500 N < 1000	CPU + GPU; CPU only
Low	CFL > 0.5	N < 500	CPU only

System optimization with multiple objectives

$$SSE(\mathbf{T},\mathbf{F},\mathbf{N}) = \underbrace{\int_0^{L_{max}} \left[\frac{|n_T(L,t_{end}) - n(L,t_{end})| + \varepsilon}{n_T(L,t_{end}) + \varepsilon}\right]^2 dL}_{\text{Target CSD realization}} + \underbrace{\int_0^{t_{end}} \left[w_1\left(\frac{dT}{dt}\right)^2 + w_2\left(\frac{dF}{dt}\right)^2 + w_3\left(\frac{dN}{dt}\right)^2\right] dt}_{\text{Smooth profiles}} + \underbrace{\int_0^{t_{end}} [w_4F + w_5N]\, dt}_{\text{Minimal flow and stirring}} + T_{fin} \overset{!}{=} min$$

Preliminary results

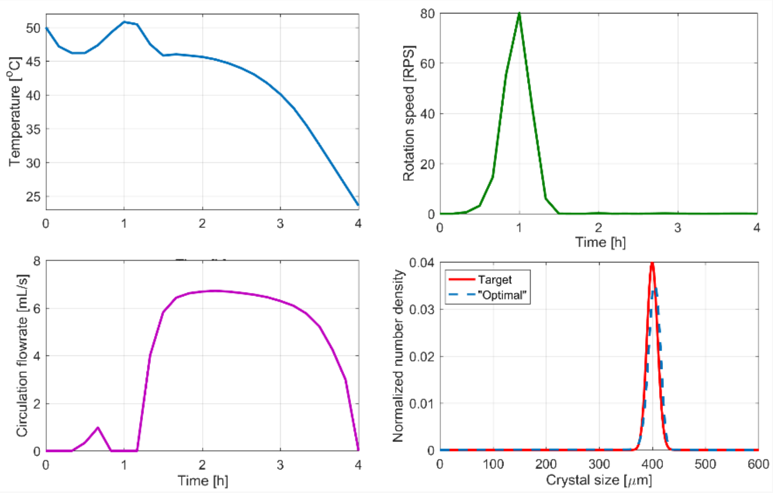

Conclusions. Projection-based soft sensors of PVM and FBRM for 2D rod-like crystals, with high real time applicability potential was created. GPU accelerated simulation of integrated batch-crystallizer-wet mill system, involving 1D PBM was applied for process optimization. The optimization revealed unexpected operation, using the wet-mill as in-situ seed generator and the recirculation stream as optimal dynamic seeder.

Publications. Szilagyi B., Borsos A., Simone E., Nagy Z. "***Model Based Estimation of 2D Crystallization Kinetics From Concentration and CLD Measurements***", Computer Aided Chemical Engineering, Accepted

Milling and Material Grindability

J.Y. Ooi, X.Z. Chen, L.G. Wang, J.F. Chen and J. Sun*

Institute for Infrastructure and Environment, School of Engineering, University of Edinburgh, Scotland, UK

*School of Planning, Architecture and Civil Engineering, Queen's University Belfast, UK

Project overview

The goal is to develop a generic methodology to link material grindability with particle dynamics in a mill.

Main objectives include:

- Understanding the local stressing events
- Characterising the comminution behaviour of particulates
- Establishing the dominant fragmentation mechanisms
- Validating through milling experiments

Impact pin mill

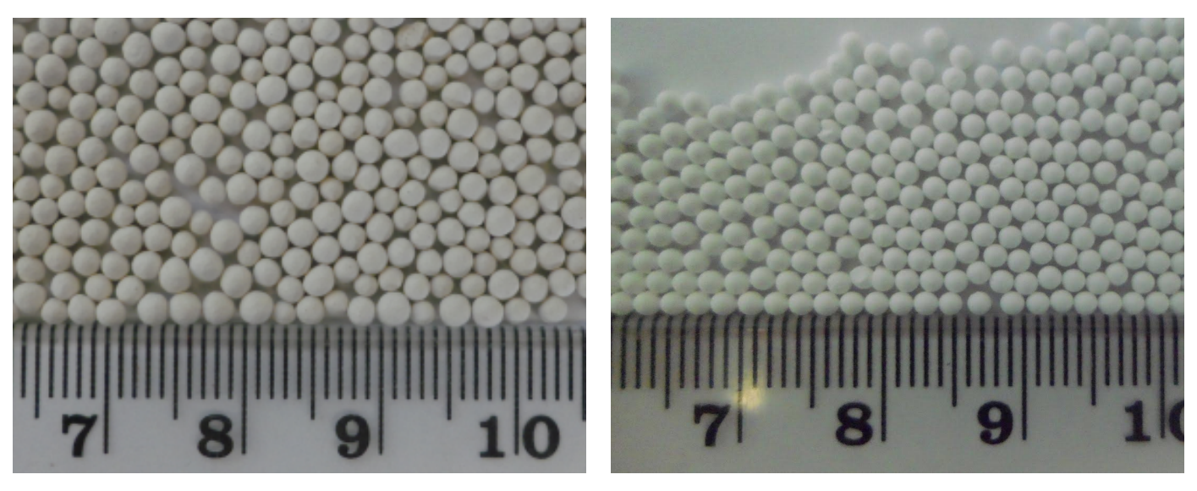

Synthetic zeolite (left) and alumina (right) sample

DEM-PBM multiscale modelling framework

- A multiscale modelling framework of DEM-PBM coupling was proposed to simulate the milling process
- DEM provides the impact velocity distribution from particle level; PBM provides the evolution of particle size distribution from process level

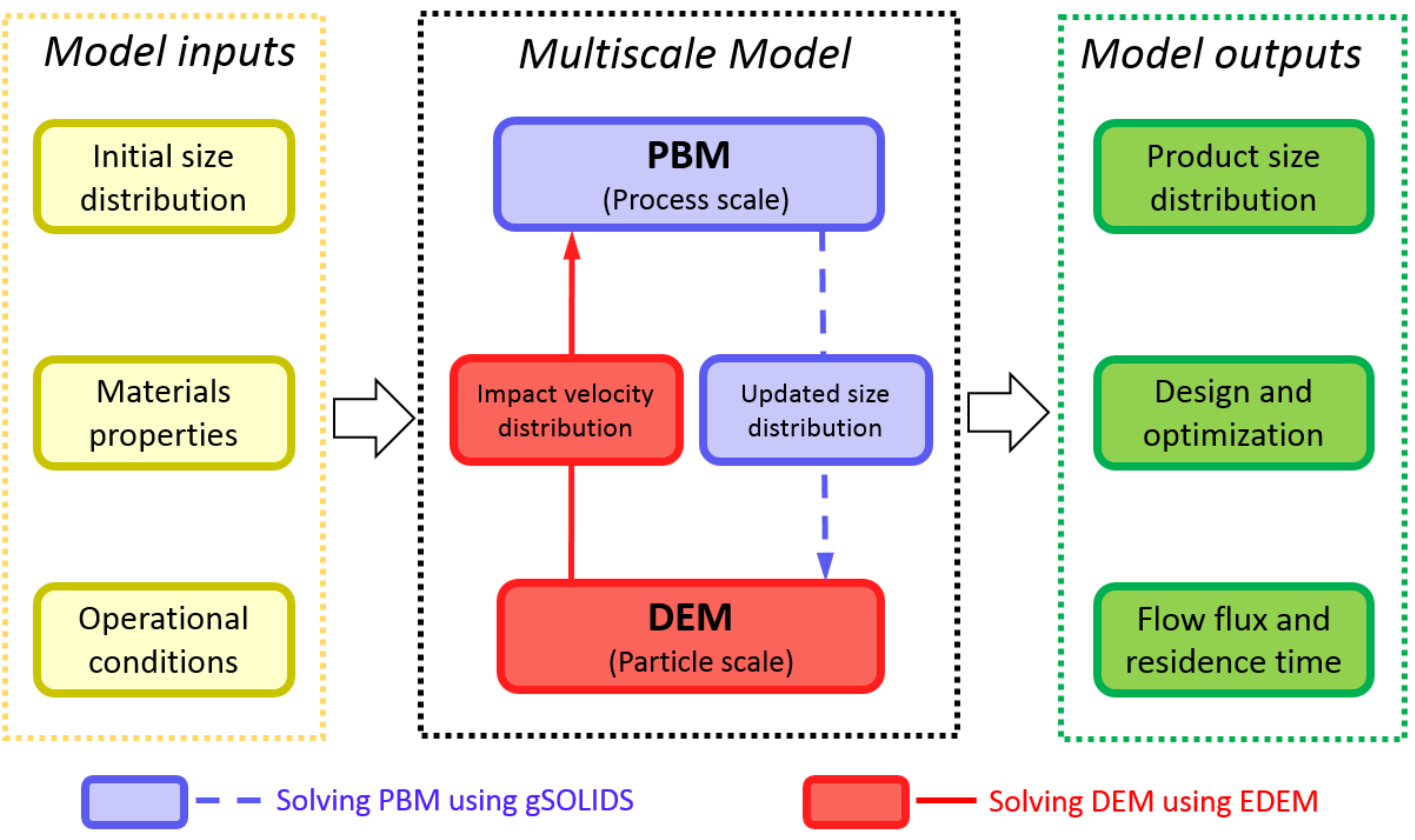

Model inputs

Initial size distribution

Materials properties

Operational conditions

Multiscale Model

PBM
(Process scale)

Impact velocity distribution

Updated size distribution

DEM
(Particle scale)

Model outputs

Product size distribution

Design and optimization

Flow flux and residence time

Solving PBM using gSOLIDS

Solving DEM using EDEM

Population balance model for milling

$$\frac{\partial M_p(x,t)}{\partial t} = -S_M(x)M_p(x,t) + \int_0^x S_M(y)M_p(y,t)b_M(x,y)\,dy$$

Breakage rate $S_M(x) = Sc_M\left[1-\exp\left(-f_{mat}x\left(W_{m,kin}-W_{m,\min}\right)\right)\right]$

Cumulative breakage Distribution $B_M(x,y) = \frac{1}{2}\cdot\left(\frac{x}{y}\right)^q\cdot\left(1+\tanh\left(\frac{x-x'}{x'}\right)\right)$

Blue variables---material dependent (fitted from one of the milling tests)

Red variables---machine dependent (obtained from DEM simulation of mill)

Impact milling tests

- Alumina particle was milled in the impact pin mill under varying rotary speed and feed rate

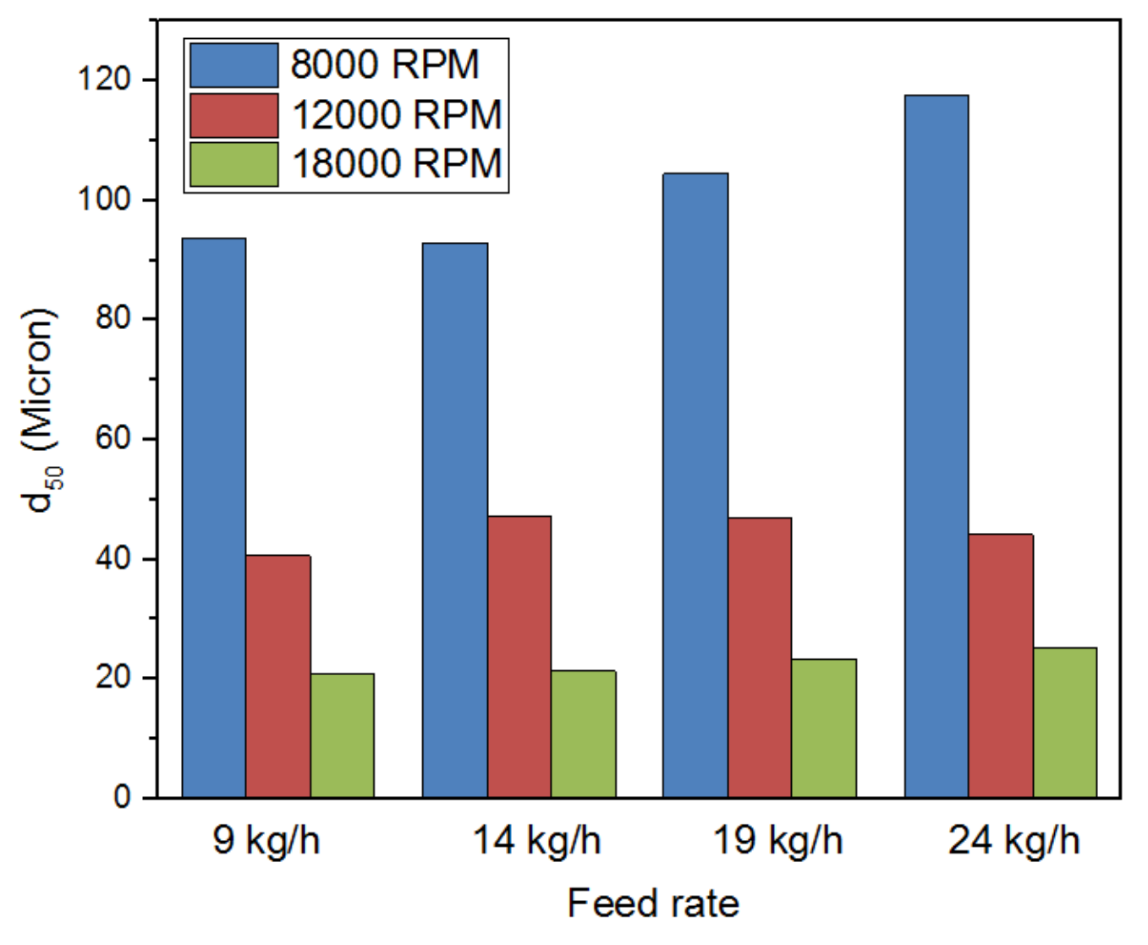

d_{50} of milled alumina particle

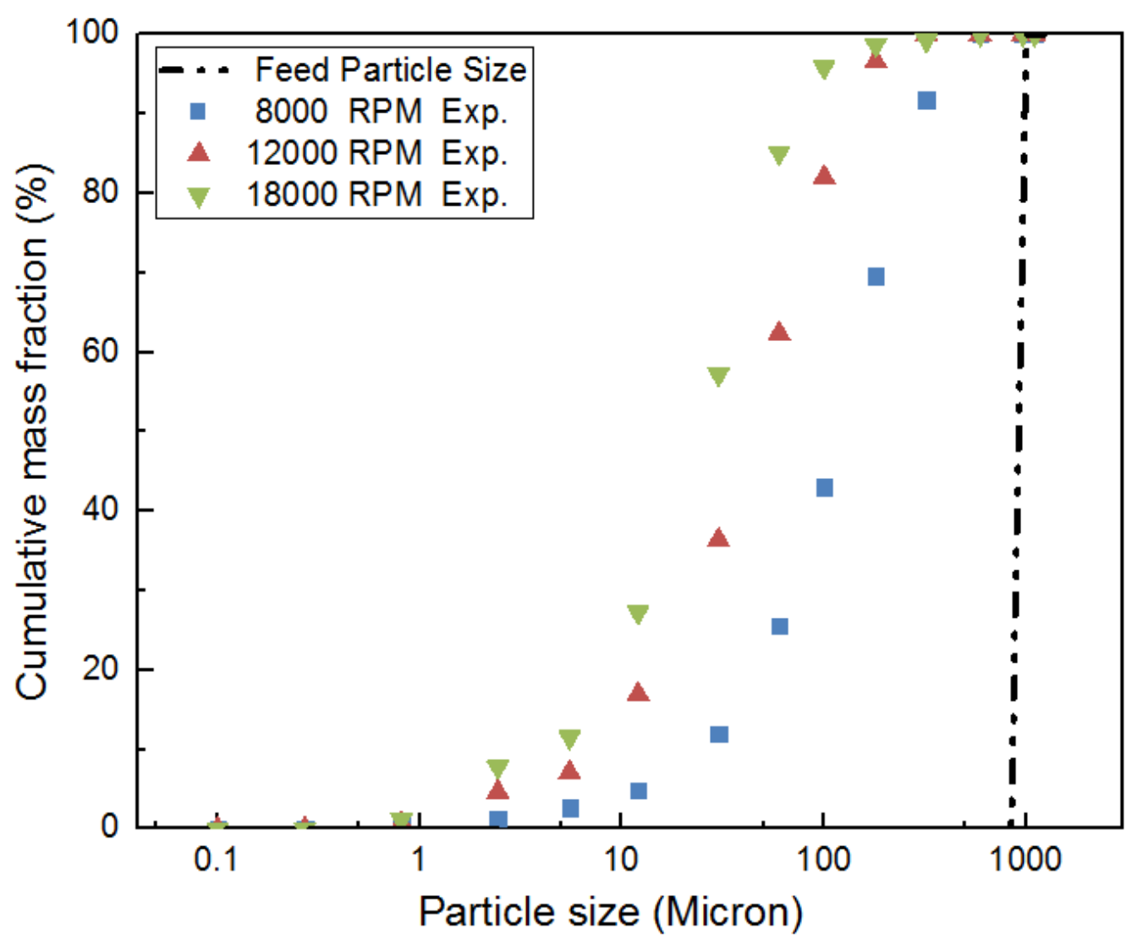

PSD of milled alumina at 24 kg/h

Particle dynamics from DEM simulation

- Real-geometry of impact pin mill UPZ100 was simulated using DEM
- The average impact velocity increases with the increasing rotary speed

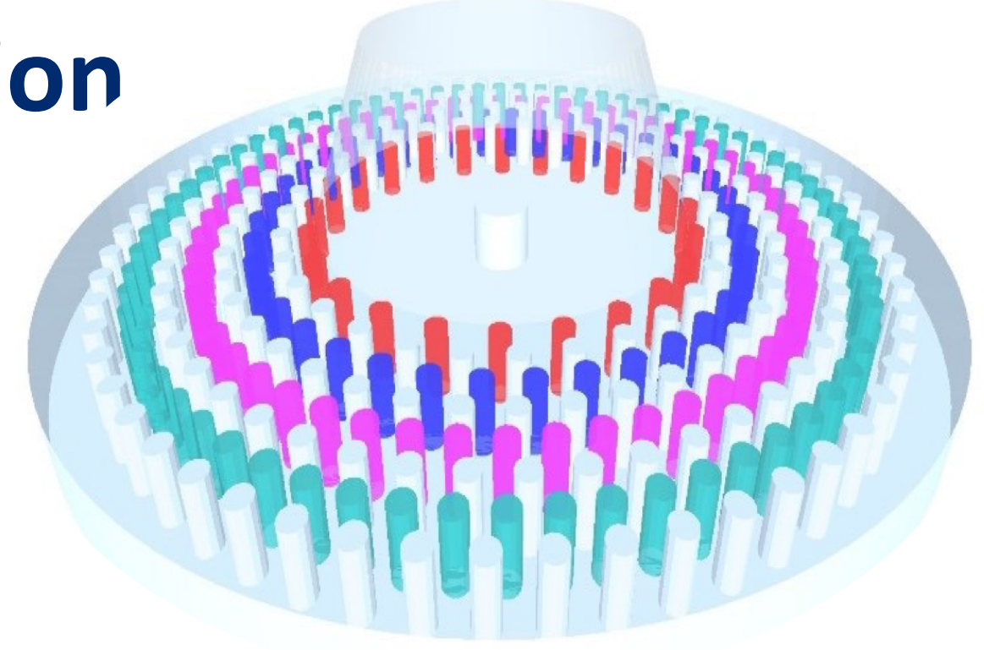

Layout of impact pin mill

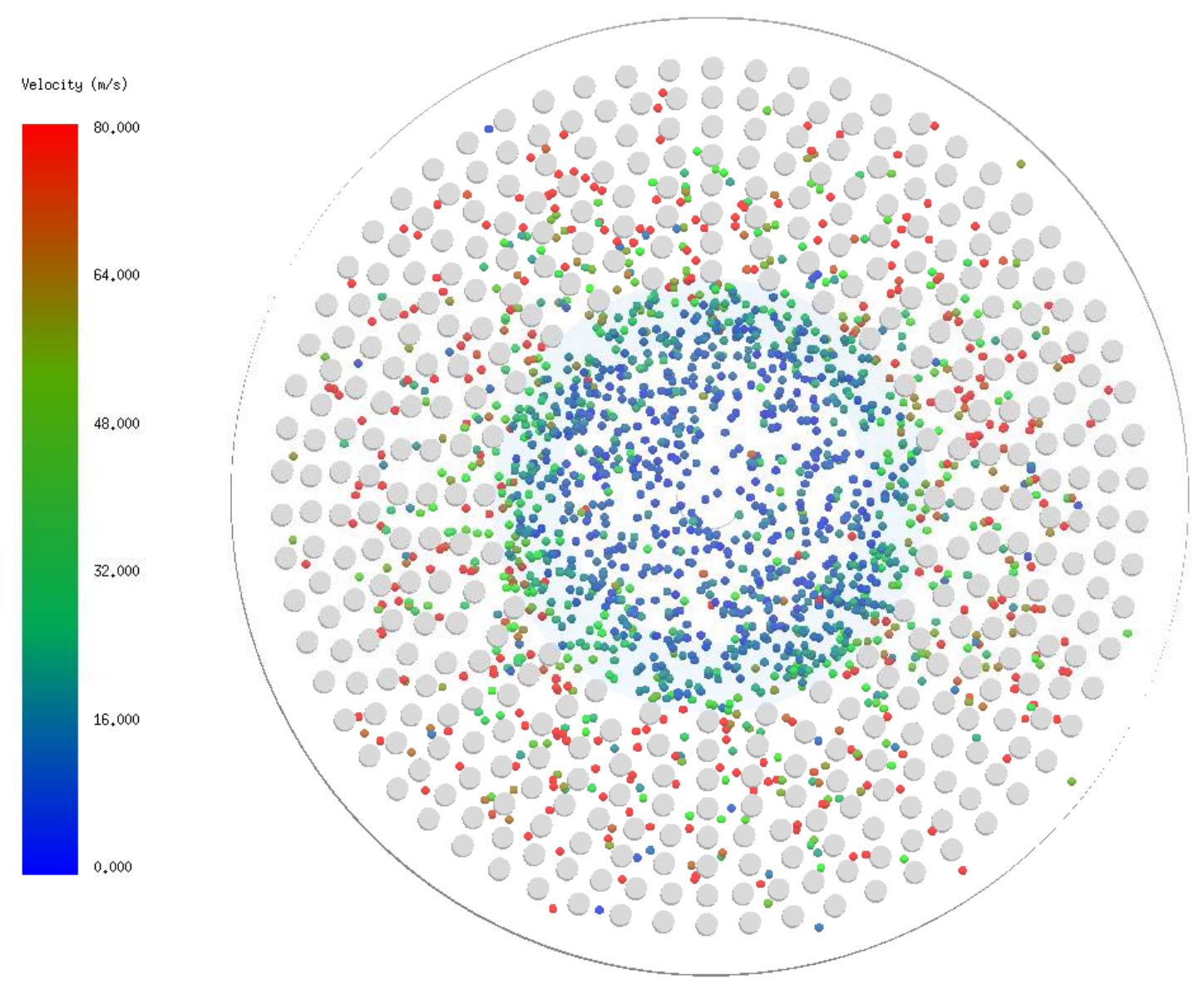

Velocity distribution of particles

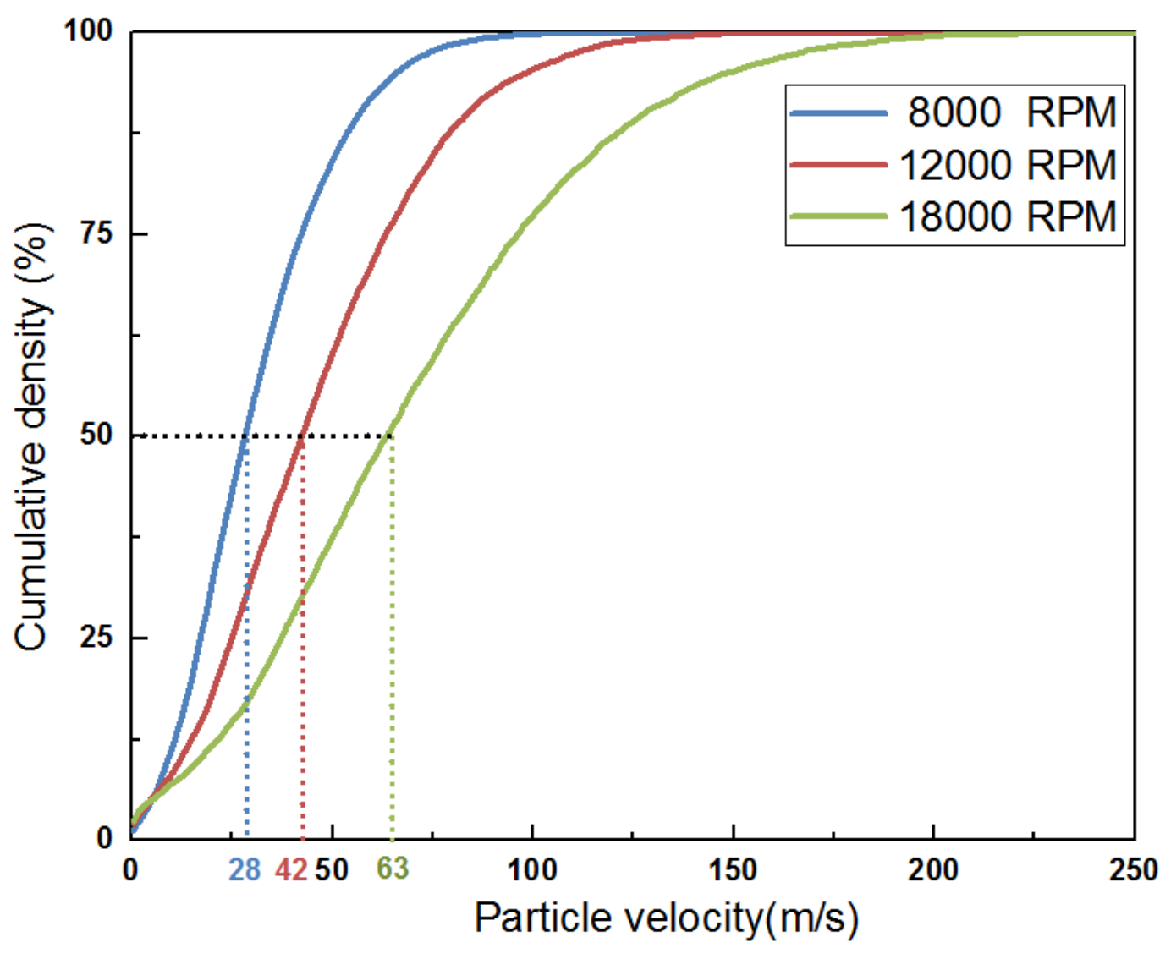

Particle velocity cumulative distribution

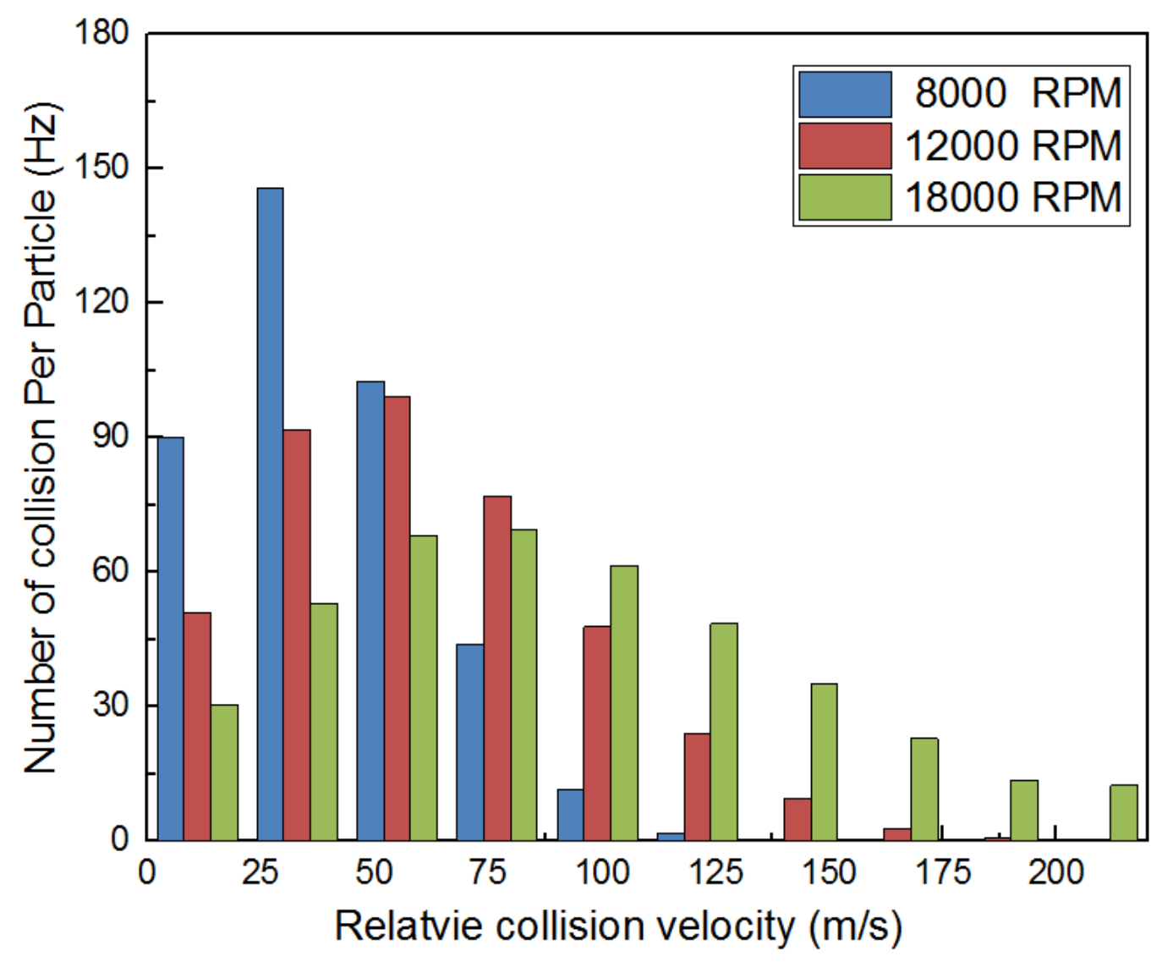

Impact velocity and number distribution

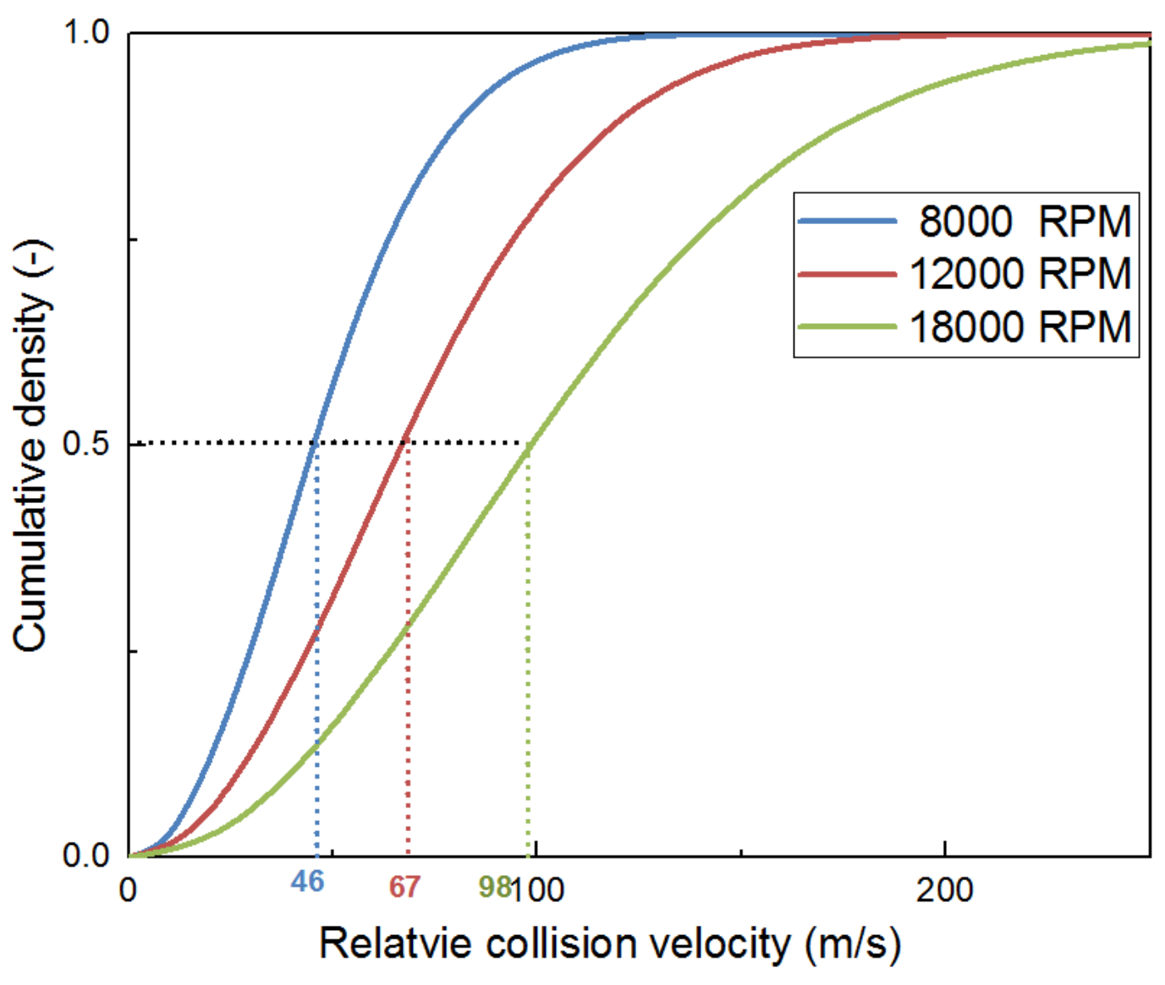

Impact velocity cumulative distribution

- Particle impact velocity increases with increasing of pin rotating speed

DEM-PBM coupling to predict PSD in an impact pin mill

- Parameters input from gSOLIDS are estimated based on the 12000 RPM of the milling tests
- With the impact velocity distribution from DEM, the prediction of PSD by gSOLIDS gives good agreement with the PSD in 8000 and 18000 RPM

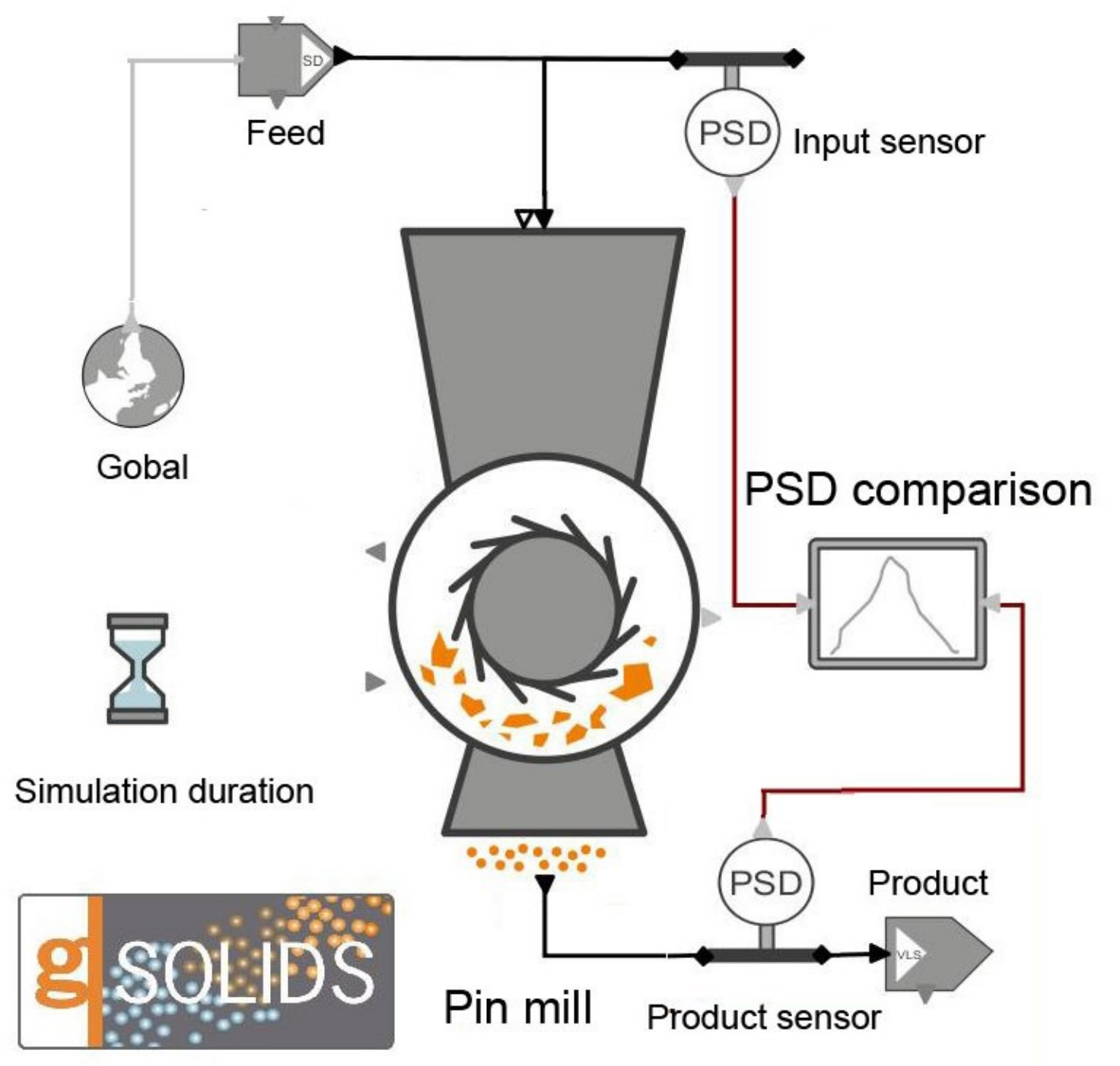

Flow chart of milling process in gSOLIDS

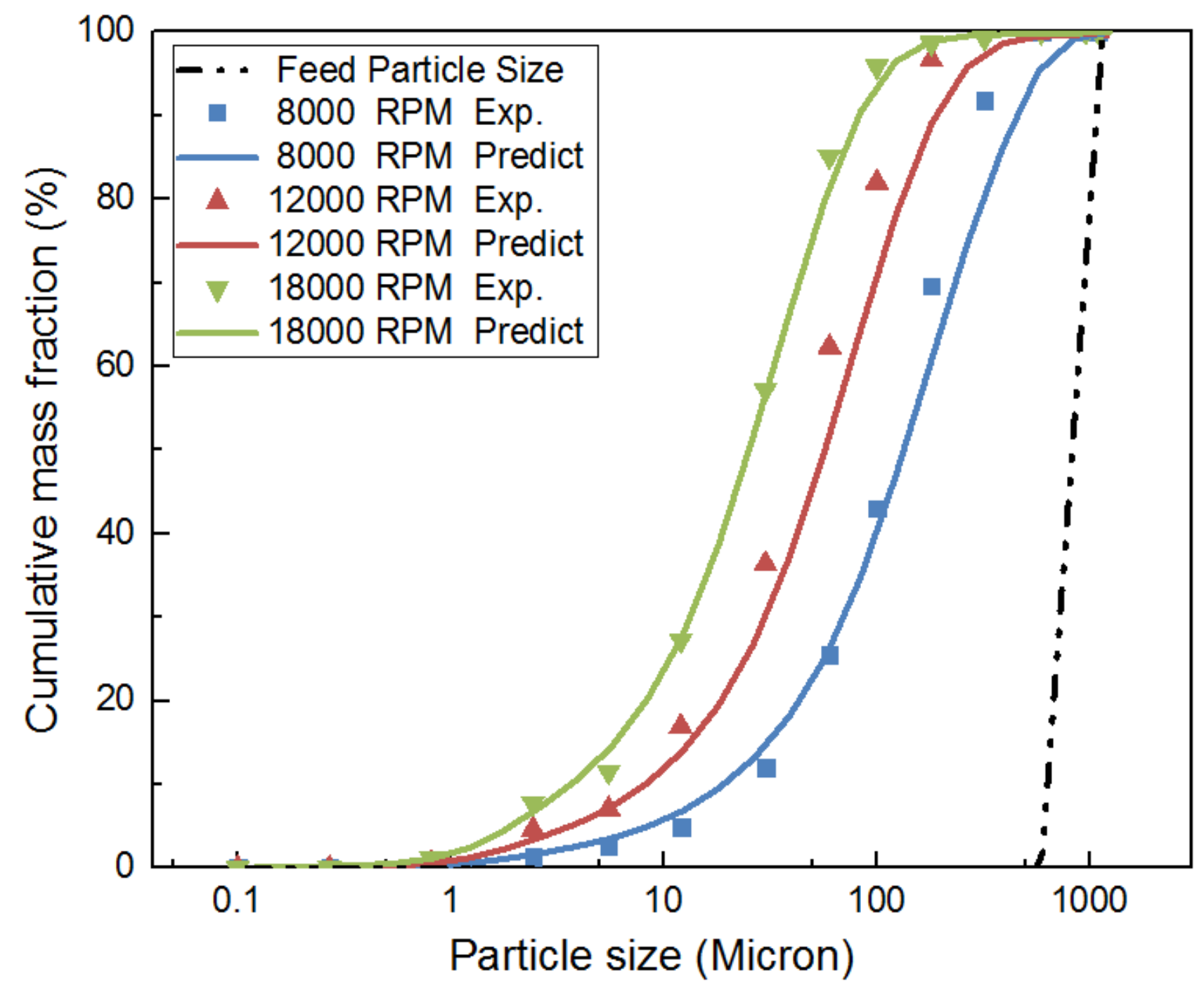

Product size distribution prediction

Concluding remarks

- A multiscale framework of DEM-PBM coupling to predict the milling behaviour of an impact pin mill has been established.
- The particle dynamics were computed from DEM and provides physical insights into the breakage kernel in PBM
- The DEM-PBM coupling shows good agreement in product size distribution prediction with the milling results
- Next steps: to improve parameter evaluation and compute PSD evolution with two-way DEM-PBM coupling

Acknowledgements

- Hosokawa Micron Ltd., UK
- Process System Enterprise, UK
- DEM Solutions Ltd, Edinburgh, UK
- The International Fine Particle Research Institute, IFPRI

Gravity and Hydrodynamics join forces to destroy Colloidal Gels

Xuemao Zhou, Joost de Graaf, Michiel Hermes, Wilson Poon

School of Physics and Astronomy, The University of Edinburgh, Edinburgh, United Kingdom

w.poon@ed.ac.uk

The stability of colloidal gels is a limiting factor to the shelf-life of many industrial products. Understanding the processes involved in the rapid collapse of gels under gravity is crucial to establish ways to improve this shelf-life. Here, we expand on our earlier analysis of the rapid collapse regime [1,2]. We experimentally demonstrate that by removing the meniscus, rapid collapse can be postponed, by removing dense particles falling through the gel. However, this does not eliminate rapid collapse. Turning to hydrodynamic simulations, we further show that pressure-driven hydrodynamic backflow alone can trigger rapid collapse, for which the onset time is related to the gravitational Péclet number of the colloids forming the gel.

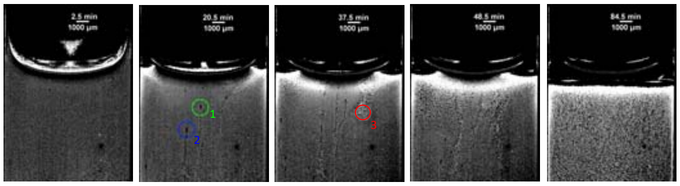

Microscopy side view of the experimental model system (1 μm PMMA particles + polystyrene polymer in water) showing the major features of rapid gel collapse: solvent droplets rising and finger like clusters falling.

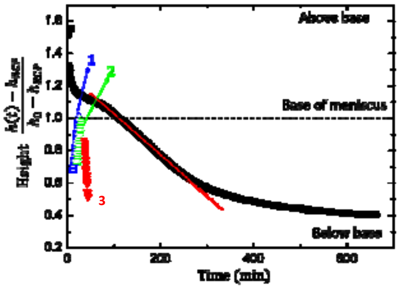

Position of the gel (black dots) with respect to the base of the meniscus as a function of time. The two droplets rising and the fingering event are also shown.

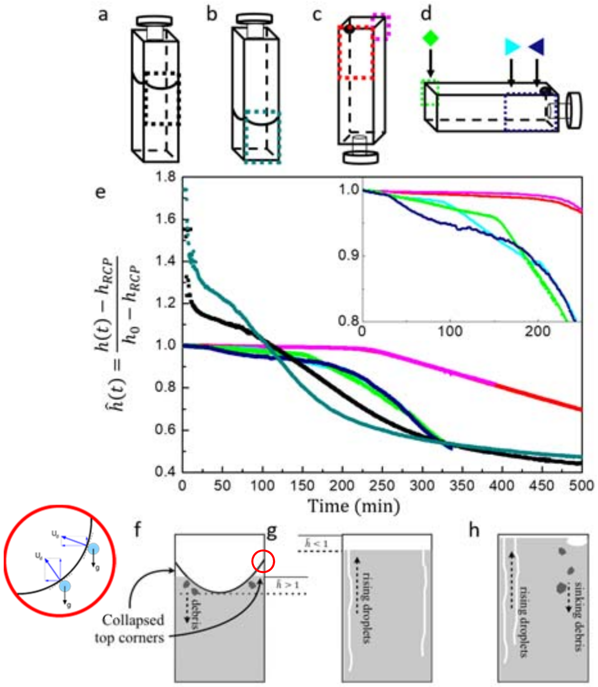

(a-d): Graphic representations of the experimental geometries. **(e):** Position of the gel with respect to the bottom of the meniscus (if present) as a function of time. **(f-h):** Cartoons illustrating the major contributions to the onset of rapid collapse. **(f):** Collapse starts at the corners of the meniscus, with debris sinking into the bulk. **(g):** Without a meniscus, collapse is uniform; droplets rising precurse the collapse. **(h):** With a partial meniscus both processes occur: the collapse due to sinking debris overtakes the one due to rising droplets.

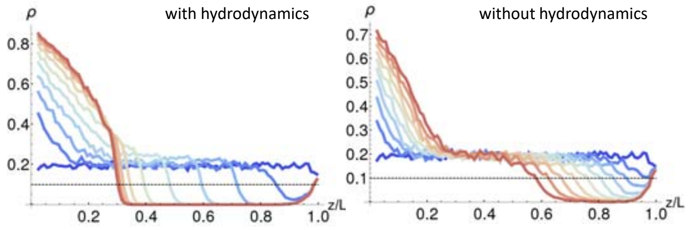

The local density ρ as a function of position in the cell, time increases from blue to red. The position of the interface can be extracted from the intercept with the dashed line.

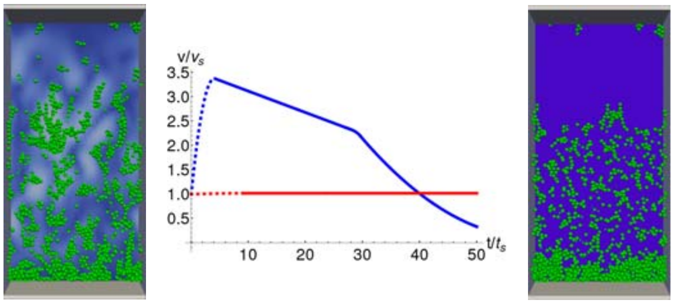

The speed of the interface v over the single-particle sedimentation speed v_s with (blue) and without (red) hydrodynamics, as a function of time t over the sedimentation time t_s. The snapshots show the lattice-Boltzmann hydrodynamics (left) and Langevin (right) simulations

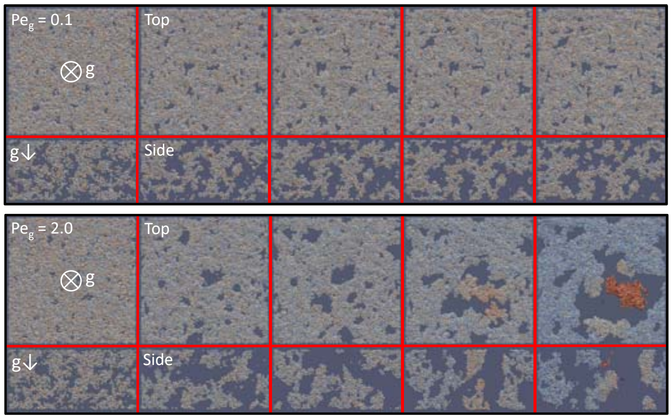

A bulk piece of colloidal gel, ϕ = 0.1, subjected to gravity and hydrodynamics for low (top) and high (bottom) Pe_g. Time increases from the left in steps of $50t_B$; t_B = Brownian time. Red colored particles move up, blue ones down.

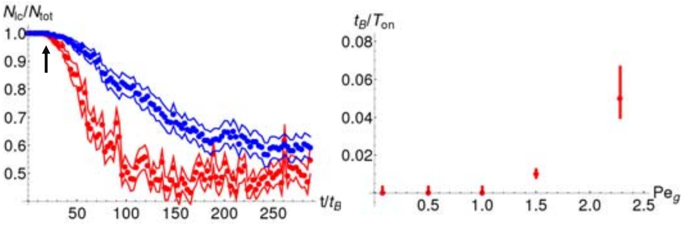

(left) The number of particles in the largest cluster N_{lc} over the total number of particles N_{tot}, for Pe_g = 2.0 and two different system sizes: N_{tot} = 10.500 (blue) and N_{tot} = 25.000 (red). The onset time for clusters to shear off, T_{on}, is indicated by the arrow and is the same; the larger system collapses more rapidly. **(right)** The inverse of T_{on} as a function of Pe_g.

This work is funded by IFPRI, EPSRC and the EU.

[1] R. Harich, T.W. Blythe, M. Hermes, E. Zaccarelli, A.J. Sederman, L.F. Gladden, and W.C.K. Poon: "*Gravitational collapse of depletion-induced colloidal gels*." Soft Matter **12**, 4300 (2016).

[2] L. Starrs, W.C.K. Poon, D.J. Hibberd, M.M. Robins: "*Collapse of transient gels in colloid-polymer mixtures*." J. Phys.: Cond. Mat. **14**, 2485 (2002).

Self-Assembled Monolayers as Nucleating Surfaces to Study Early Formation Pathways of Crystallographic Polymorphs

Cornell University

Zihao Zhang, Katherine P. Barteau, Lara A. Estroff, and Ulrich B. Wiesner
Materials Science and Engineering, Cornell University, Ithaca NY

IFPRI
International Fine Particle Research Institute

Abstract

Self-assembled monolayers (SAMs) are well-defined surfaces that can be used to study the relationship between the nucleation event and the final polymorph selection. Furthermore, by tuning the substrate-crystal interface energy, potentially crystalline order of SAMs can promote the nucleation of polymorphs not accessible via solution methods. It is these two advantages, i.e. the establishment of scientific correlations between nucleation and observed polymorph and access to polymorphs not accessible via solution methods, that have led us to choose heterogeneous surface nucleation via SAMs as the primary means to study polymorph selection.

In this work, we have examined multiple SAM chemistries on gold and silicon in the presence of various solvent systems to investigate their ability to influence the nucleation, crystal growth, and polymorph selection of a common drug, acetaminophen (ACM). We have found that both solvent and substrate work together to control crystal polymorph. The –CH$_3$ and phenyl terminated surfaces promote the formation of the less thermodynamically stable orthorhombic form of ACM with (002) cleavage planes perpendicular to the substrate, and the -OH surface induces the same polymorph of orthorhombic ACM, but with the (002) cleavage planes parallel to the substrate surface. We hypothesize that this selection is due to the energetic favorability of certain crystal facets interacting with the chemically specific SAMs surface.

Background

Why try to control crystal polymorphs?

The understanding and control of crystallographic polymorphism and crystal habit of organic as well as inorganic compounds is scientifically and technologically important to a number of industries. To date, however, the experimental control of polymorphs (crystalline solids with different arrangements of the same constituents) is difficult.

Use of surfaces as nucleating agents

We form arrays of self-assembled monolayers (SAMs) from alkane-thiols, with different terminal (omega) functional groups, on gold substrates. These arrays of SAMs will provide nucleating surfaces with diverse chemical functionality.

Why use self-assembled monolayers?

One benefit of using SAMs to study polymorphism is that the polymorph selectivity of a given surface should be related to the chemical, stereo-chemical, and 2-D crystalline structure of the SAM. By studying the relationships between the structure of the crystal and the nucleating surface, we will gain insights into molecular-scale recognition events that can lead to polymorphism.

Experimental Design – Drug Choice

Acetaminophen (Paracetamol, ACM)

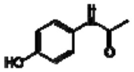

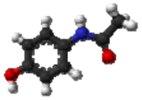

https://en.wikipedia.org/wiki/Paracetamol

- Two well-known polymorphs: monoclinic and orthorhombic
- Surface chemistries presented on crystal faces differ between the polymorphs
- Popular use in medication and readily available
- The monoclinic polymorph (Form I) is the thermodynamically preferred and commercially produced form
- The orthorhombic polymorph (Form II) would be desirable for easier commercial processing due to its flat cleavage planes

Acknowledgements

This research is supported by IFPRI. This work made use of the Cornell Center for Materials Research Shared Facilities which are supported through the NSF MRSEC program (DMR-1120296).

Key Results

Solvent Effects on the polymorph control: hydrophobic surfaces

Solvent	*SAM chemistry*	*n*	*Form I*	*Form II*
Ethanol  OH	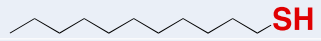 SH	20	**80%**	20%
	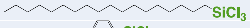 SiCl$_3$	18	**94%**	6%
	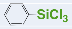 SiCl$_3$	14	**93%**	7%
DI water	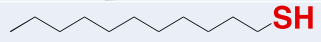 SH	9	**93%**	7%
	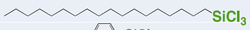 SiCl$_3$	18	**89%**	11%
	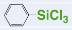 SiCl$_3$	10	**90%**	10%
1,4-dioxane 	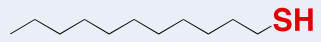 SH	12	**100%**	0
	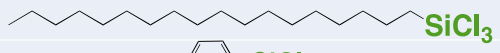 SiCl$_3$	10	**90%**	10%
	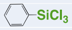 SiCl$_3$	10	**70%**	30%
DI water/dioxane 20:80	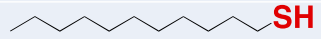 SH	11	9%	**91%**
	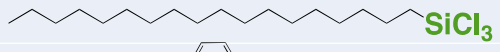 SiCl$_3$	11	0	**100%**
	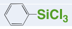 SiCl$_3$	9	0	**100%**

ACM crystallization in a mixture of water and 1,4-dioxane results in Form II, while either pure water or pure 1,4-dioxane primarily yields Form I. Polymorph selection is not strongly sensitive to the specific hydrophobic surface chemistry.

Both solvent and substrate work together to control polymorph

Substrate Solvent	-CH$_3$ on gold (hydrophobic)			-OH on gold (hydrophilic)		
	N	Form I	Form II	N	Form I	Form II
DI water	**9**	**93%**	7%	**17**	**100%**	0
DI water/ dioxane 20:80	**11**	9%	**91%**	**10**	0	**100%**
1,4-dioxane	**11**	**100%**	0	**10**	20%	**80%**
Ethanol	**20**	**80%**	20%	**11**	9%	**91%**

In water containing systems, polymorph selection is independent of substrate chemistry, whether hydrophobic or hydrophilic. However, for pure organic solvents, the polymorph switches from Form I to Form II when surface chemistry is changed from hydrophobic to hydrophilic.

Substrate can dictate crystallographic orientation

Solvent	*SAM chemistry*	*n*	*Form I*	*Form II*
DI water/dioxane 20:80	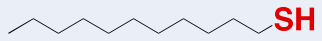 SH	11	9%	**91%**
	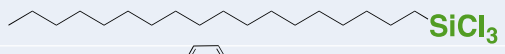 SiCl$_3$	11	0	**100%**
	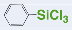 SiCl$_3$	9	0	**100%**
	 HO SH	10	0	**100%**

X-ray Diffraction (XRD) of ACM on PTS and –OH surfaces

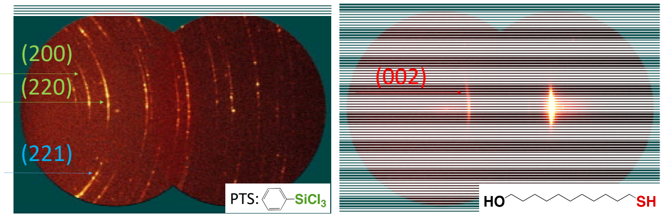

Using a water/dioxane mixture as the crystallization solvent, Form II crystallized on both hydrophobic and hydrophilic surfaces, but the observed orientation of the crystal is vastly different depending on surface chemistry.

Substrate can dictate crystallographic orientation

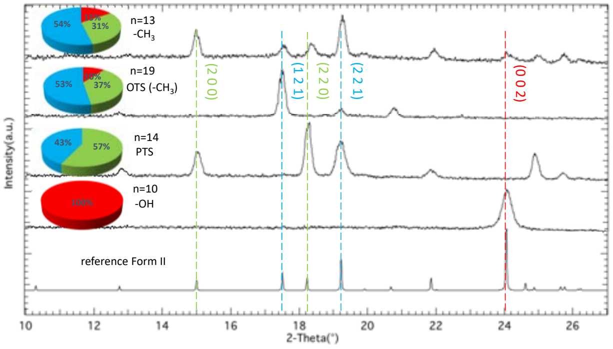

🟥 (0 0 2) or parallel 🟦 Non-orthogonal angle 🟩 Perpendicular to (0 0 2)

The XRD patterns indicate that –OH terminated SAMs strongly orient the (002) plane parallel to the substrate, whereas PTS and other hydrophobic SAMs induces "high angle" orientations, which are perpendicular or nearly perpendicular to the (0 0 2) plane.

Molecular interpretation and orientation influence on the morphology

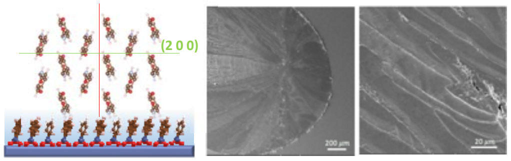

On PTS surfaces, ACM crystallizes as Form II, with the **(002) cleavage planes perpendicular** to the substrate. Crystallites appear **large and smooth**.

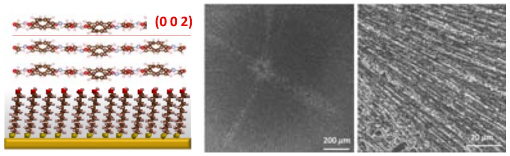

On -OH surfaces, ACM crystallizes as Form II, with the **(002) cleavage planes parallel** to the substrate. Crystallites appear **small and rough.**

Conclusions

1. A more reproducible and inexpensive SAMs system on silicon wafers was introduced, the results of which are consistent with our earlier studies on gold-thiol based SAMS
2. On hydrophobic surfaces, use of pure solvents resulted in ACM Form I, while a mixture of water and dioxane produces Form II
3. In general, both the solvent and SAM surface chemistry act in concert to control polymorph selection
4. The SAM detailed surface chemistry further influences the crystallization orientation

Future Directions (Year 3)

- In-depth studies of earliest stages of crystal formation as observed by optical microscopy and in-situ blade coating coupled x-ray scattering.
- cryo-scanning transmission electron microscopy (cryo-STEM) on early nucleation and growth stages
- Work with industry to identify other organic compounds for in-depth polymorph studies

Blade-coating of ACM on PTS surface from 1,4-dioxane

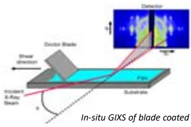

In-situ GIXS of blade coated films

Y. Gu, U.W. *et al*, *Macromolecules 2016*, **49,** 4195.

Die Filling of Aerated Powders

Joesry El Hebieshy, Serena Schianoand Chuan-Yu (Charley) Wu,
Department of Chemical and Process Engineering,
University of Surrey, Guildford, UK
Email: C.Y.Wu@surrey.ac.uk

1. Introduction

- ❑ Die filling is a critical process stage in powder compaction, a common manufacturing process for a wide range of products including pharmaceutical and detergent tablets, catalyst pellets, fertilizer, biomass, ceramic and metallic components.
- ❑ Powder behaviour during die filling plays a dominant role in controlling the performance of subsequent processes and the quality of final products, as it determines the pre-compaction conditions (e.g. density distribution, composition distribution, packing patterns).
- ❑ Moreover, any defects induced during die filling (such as segregation, insufficient filling) will have a detrimental impact on the properties of the products.
- ❑ Understanding of complex powder behaviour during die filling also helps decode complicated nature of fine powder mixtures, as a number of powder characteristics (flowability, permeability, etc.) controls the behaviour of powders during die filling.
- ❑ The goal of this project is to understand the die filling behaviour of aerated powder blends. The following three tasks are proposed:

Task I
Rotary die filling
(M1-M12)

Task 2
Assisted die filling
(Suction filling, paddled shoe; M13-M24)

Task 3
Segregation during die filling
(M25 - M36)

2. Rotary die filling

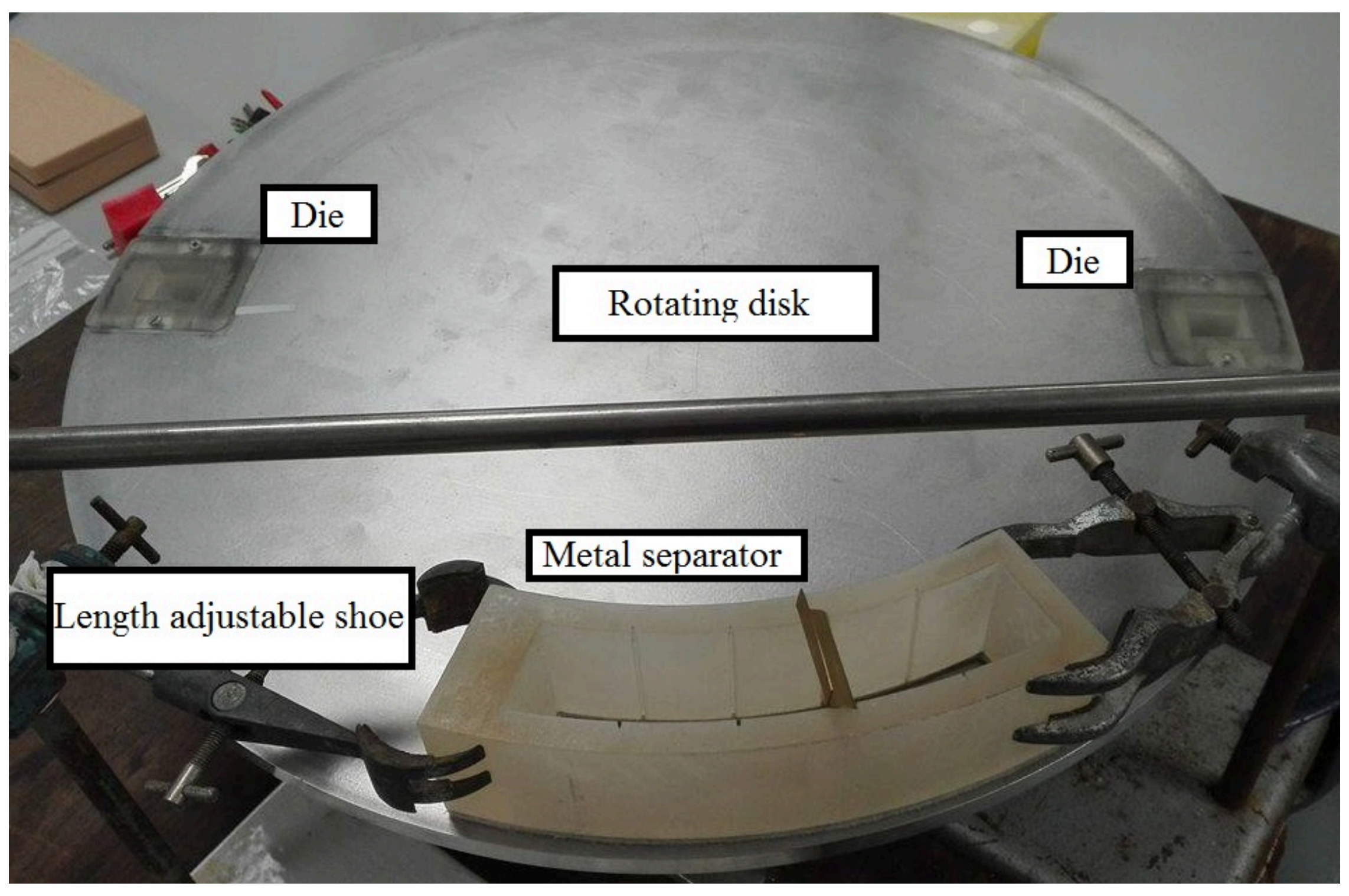

- ❑ A rotary die filling system was developed.
- ❑ The system was fitted with two dies and a shoe with adjustable length of 30-150 mm.
- ❑ A filling speed of 0-1,500 mm/s can be achieved.
- ❑ Comparative study with linear die filling was performed using Cenopheres 500 (d=500 μm, ρ_p=600 kg/m^3).
- ❑ The effect of shoe length was also explored.

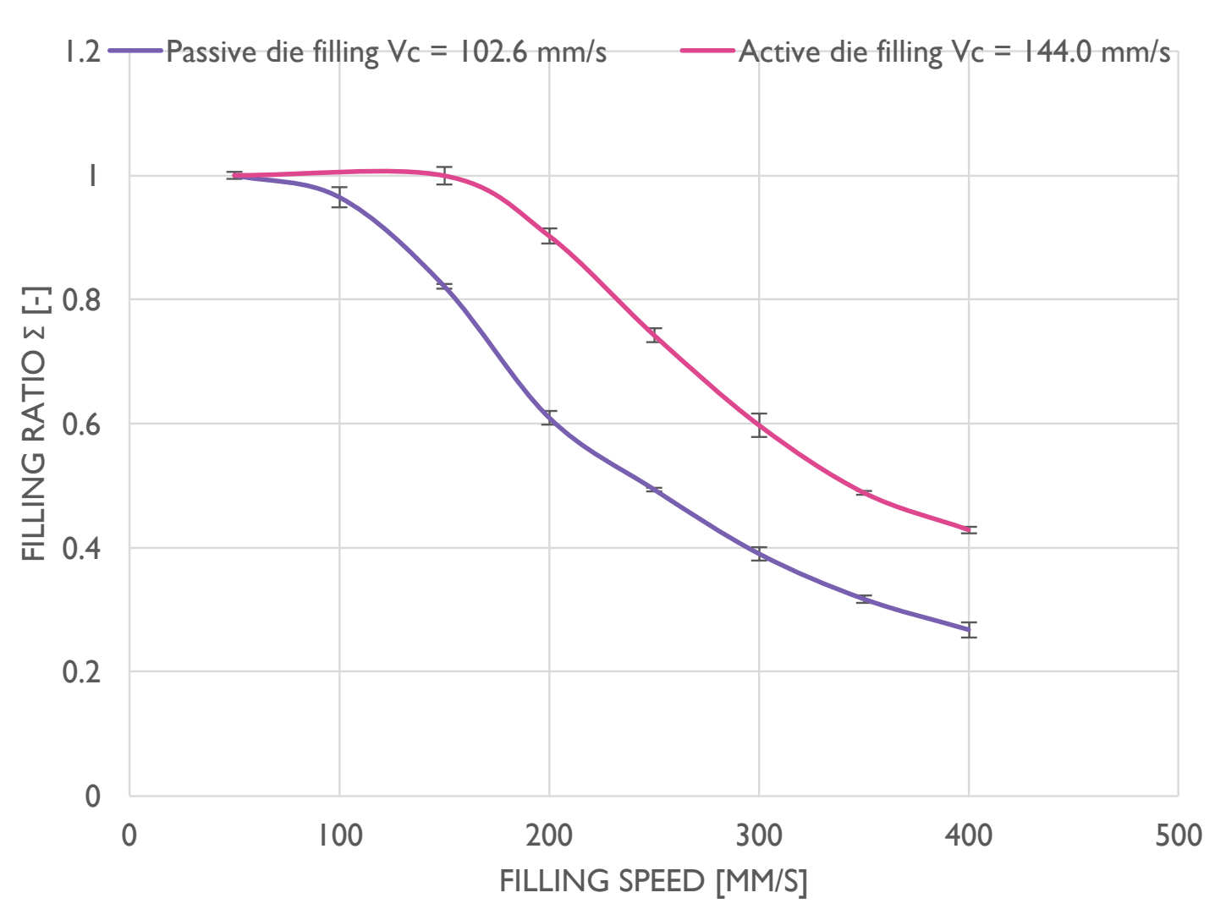

Experimental results.

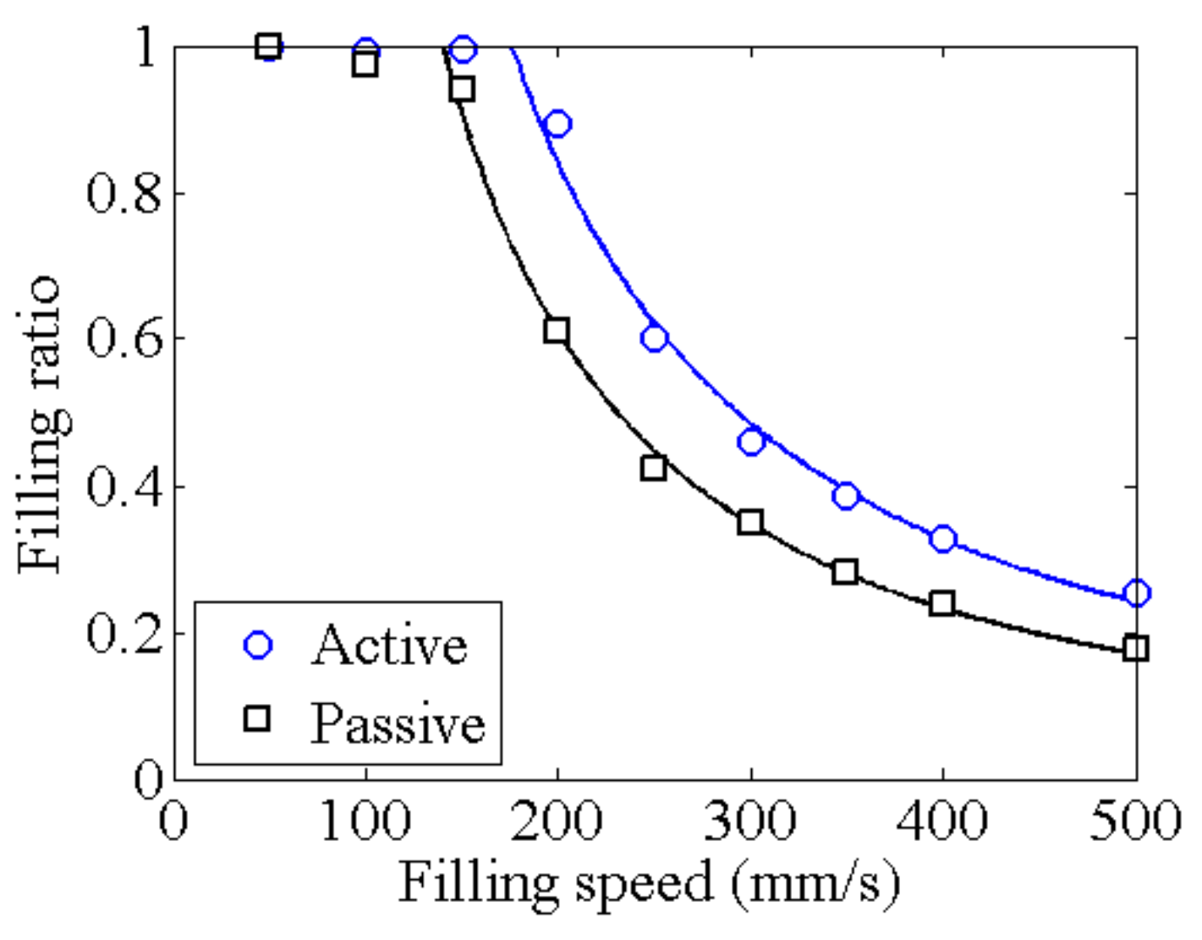

DEM Simulation
(Wu, 2008, *PARTICUOLOGY*, 6 (6), pp. 412-418.)

- ❑ A higher filling ratio is generally obtained during rotary die filling (active) than passive die filling (the die is stationary).
- ❑ Excellent agreement between experimental and numerical simulations is obtained.
- ❑ As the shoe length increases, more powder is deposited into the die, due to the increase in the effective discharge time (i.e. residence time).

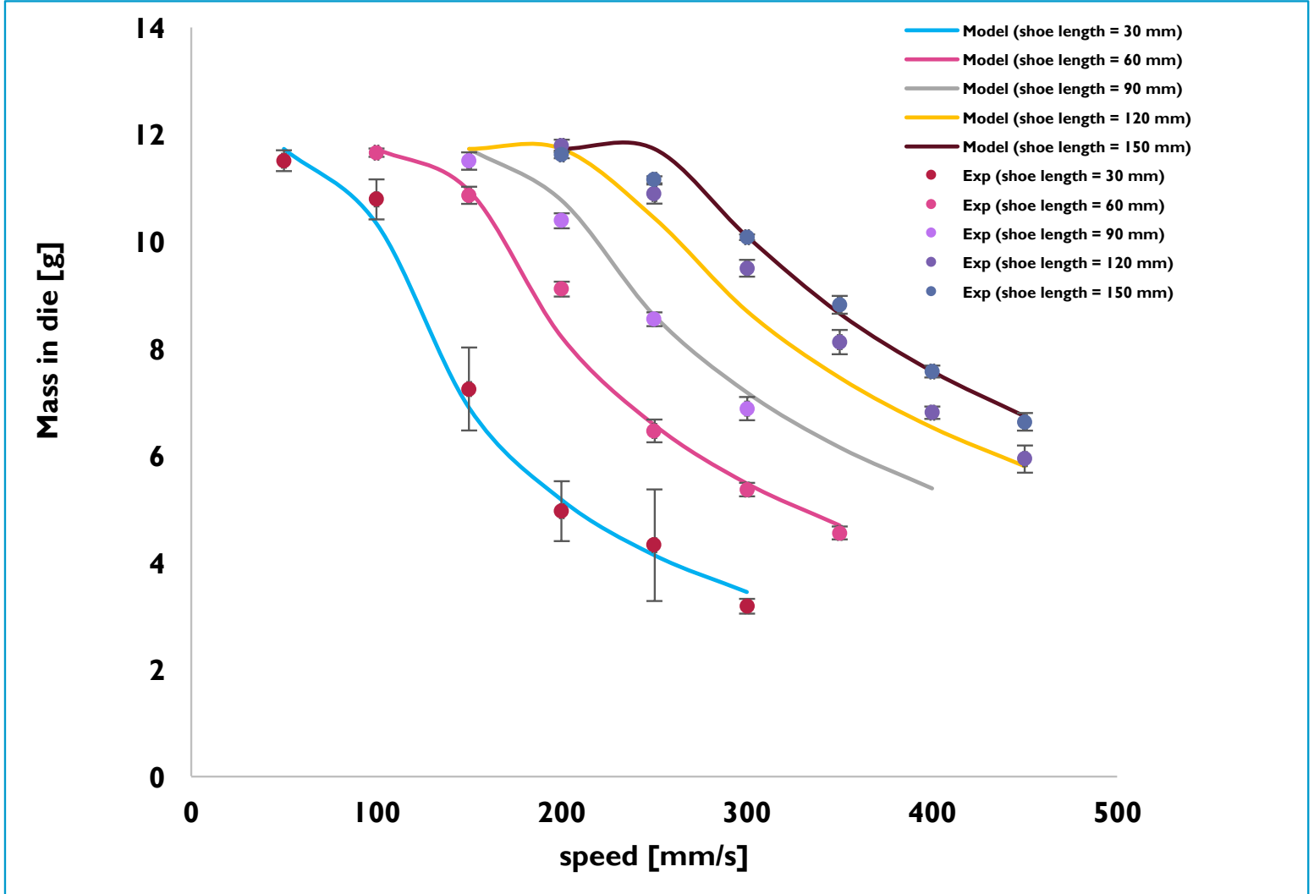

3. Density-induced segregation during die filling

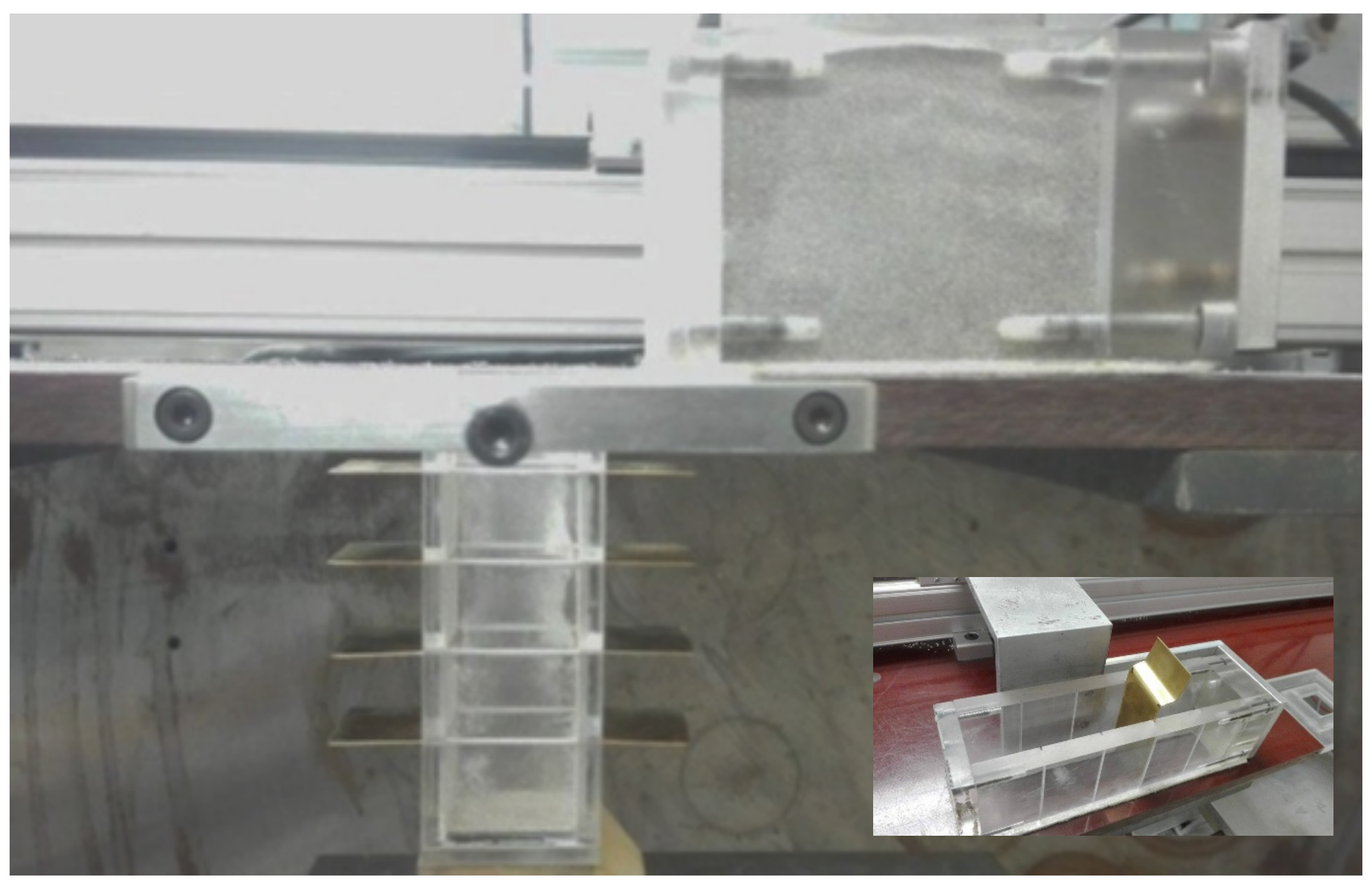

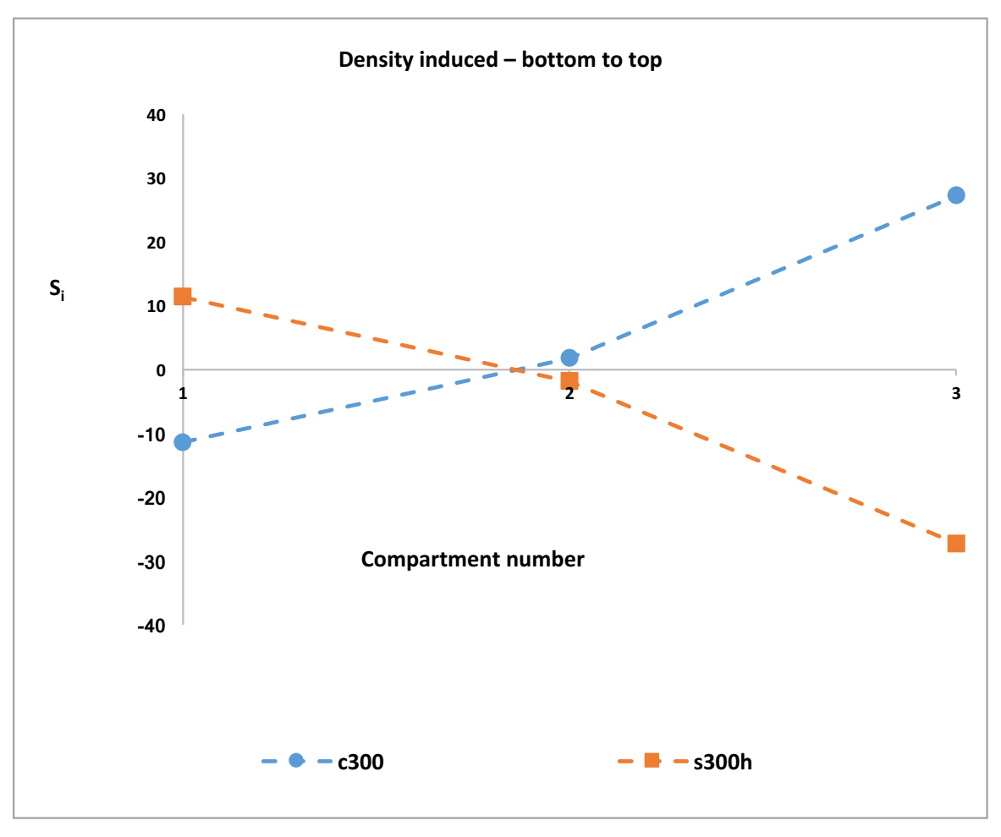

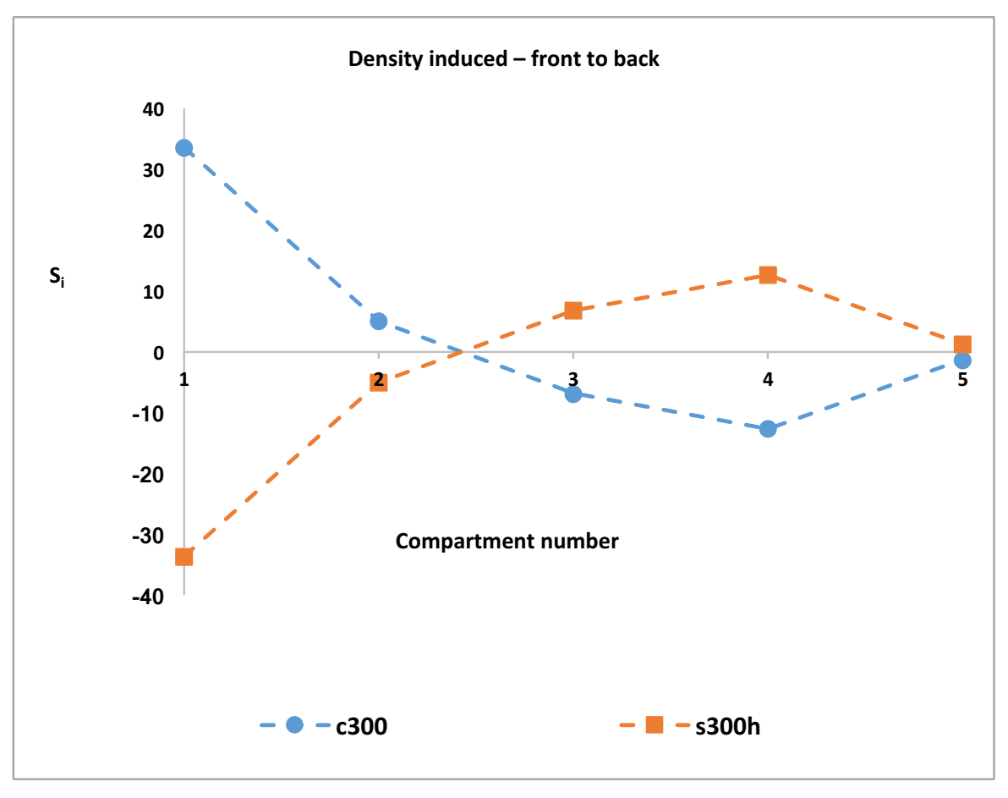

- ❑ Density induced segregation was experiemntally explored.
- ❑ It was found that significant segregation took place during filling the shoe and die filling.
- ❑ Segregation tendency during die filling depnds on the filling speed.

4. Air pressure build up during die filling

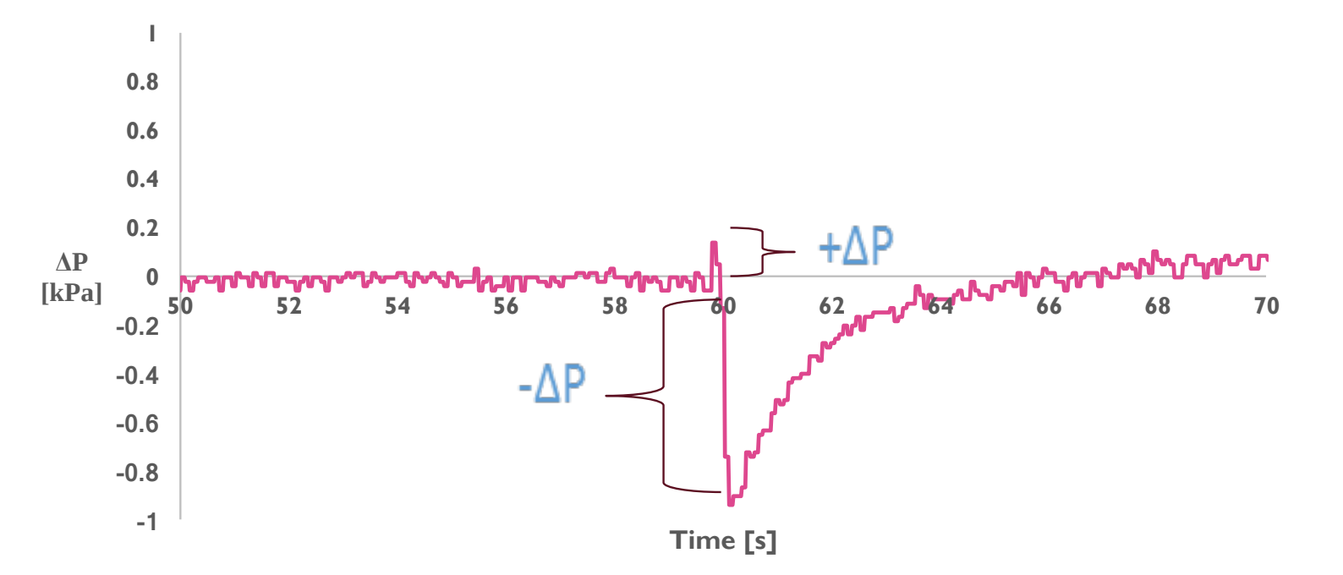

Using the die filling system instrumented with an online air pressure sensor, it revealed that there is a significant pressure drop in the die during die filling. Similar phenomena were also observed by Donsi et al. (1997).

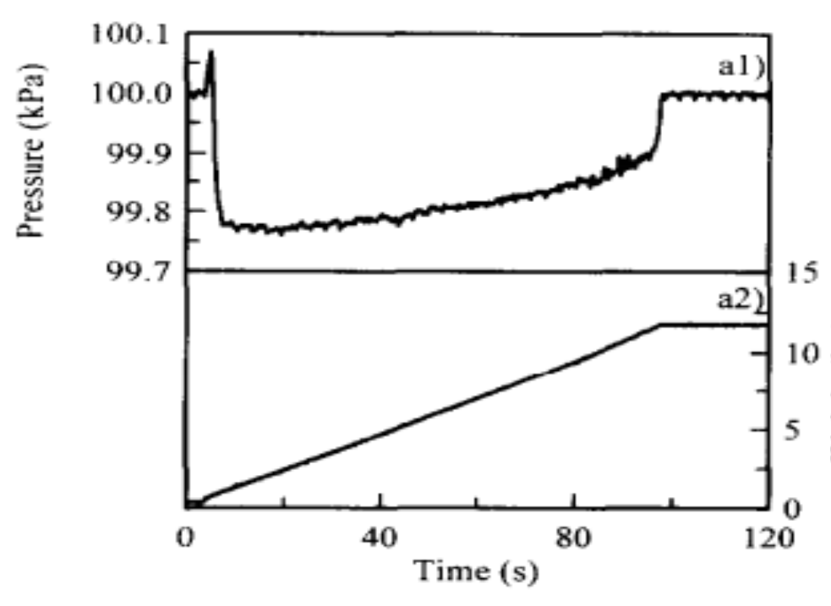

The pressure and mass flow rate evolution of a hopper discharging glass beads of d50= 5 5µm (Donsi et al. 1997)

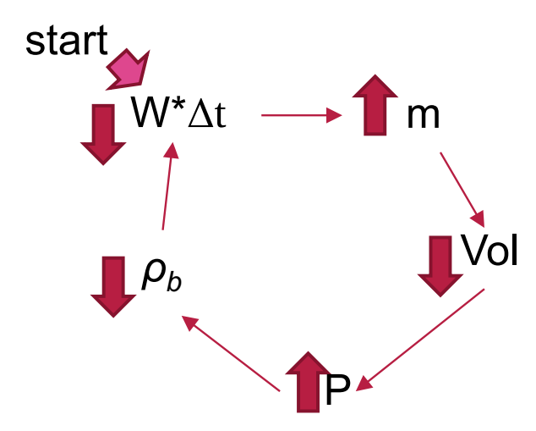

$$W = C\rho_b\sqrt{g}(D_0 - kd_p)^{5/2}$$

$$C = \frac{P_{atm}}{P_{atm} + \Delta P}$$

$$\Delta P = \left(\frac{P_{atm}.Vol_d}{Vol_d - V_{mp}}\right) - \left(\frac{180 h_s \eta_a (1-\varepsilon)^2}{\psi^2 d_p{}^3 \varepsilon^3 C_d \rho_a} \frac{(-6) l_d d_p \pi \eta_a}{\sqrt{2hd_p/g}}\right)$$

$$V_{mp} = \frac{mt}{\rho_t}$$

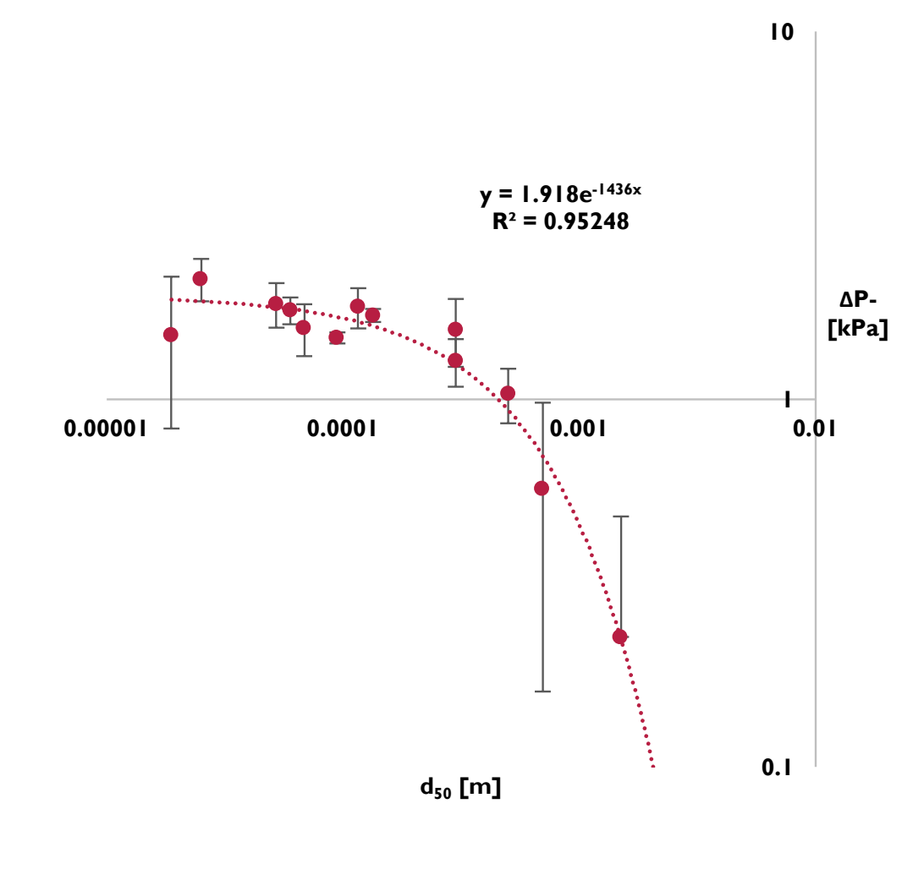

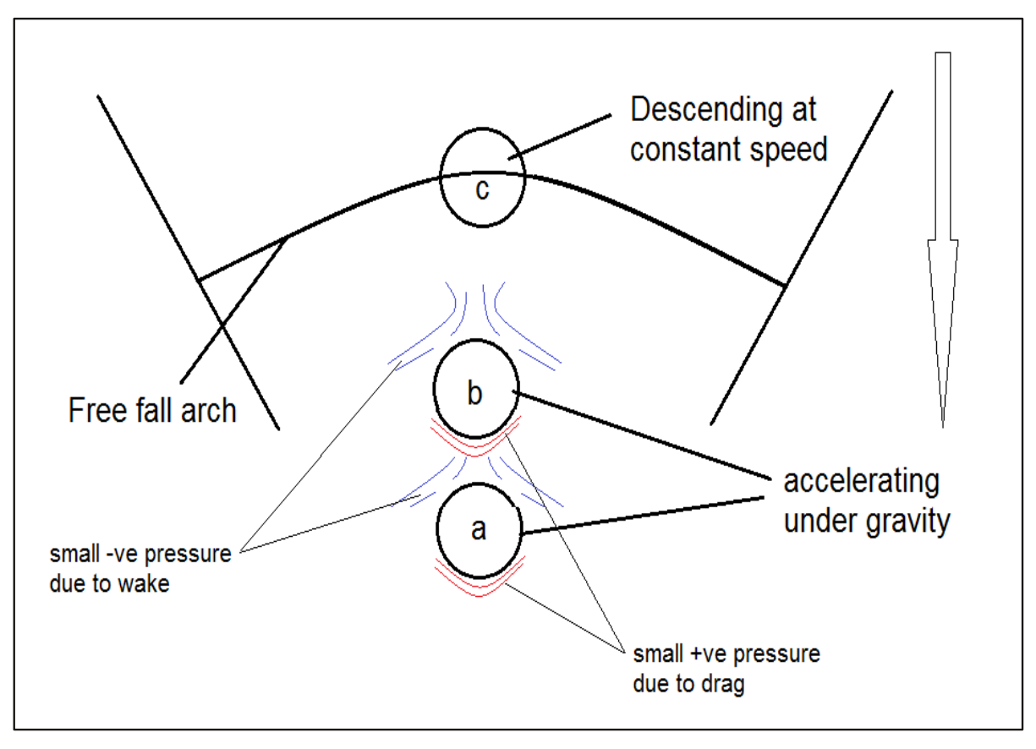

$$\Delta P_D = \frac{3}{2}\frac{\eta_a V_t}{(d_p/2)}\cos\pi\frac{S_a(1-\varepsilon_i)d_p}{(4/3)\pi(d_p/2)^3}$$

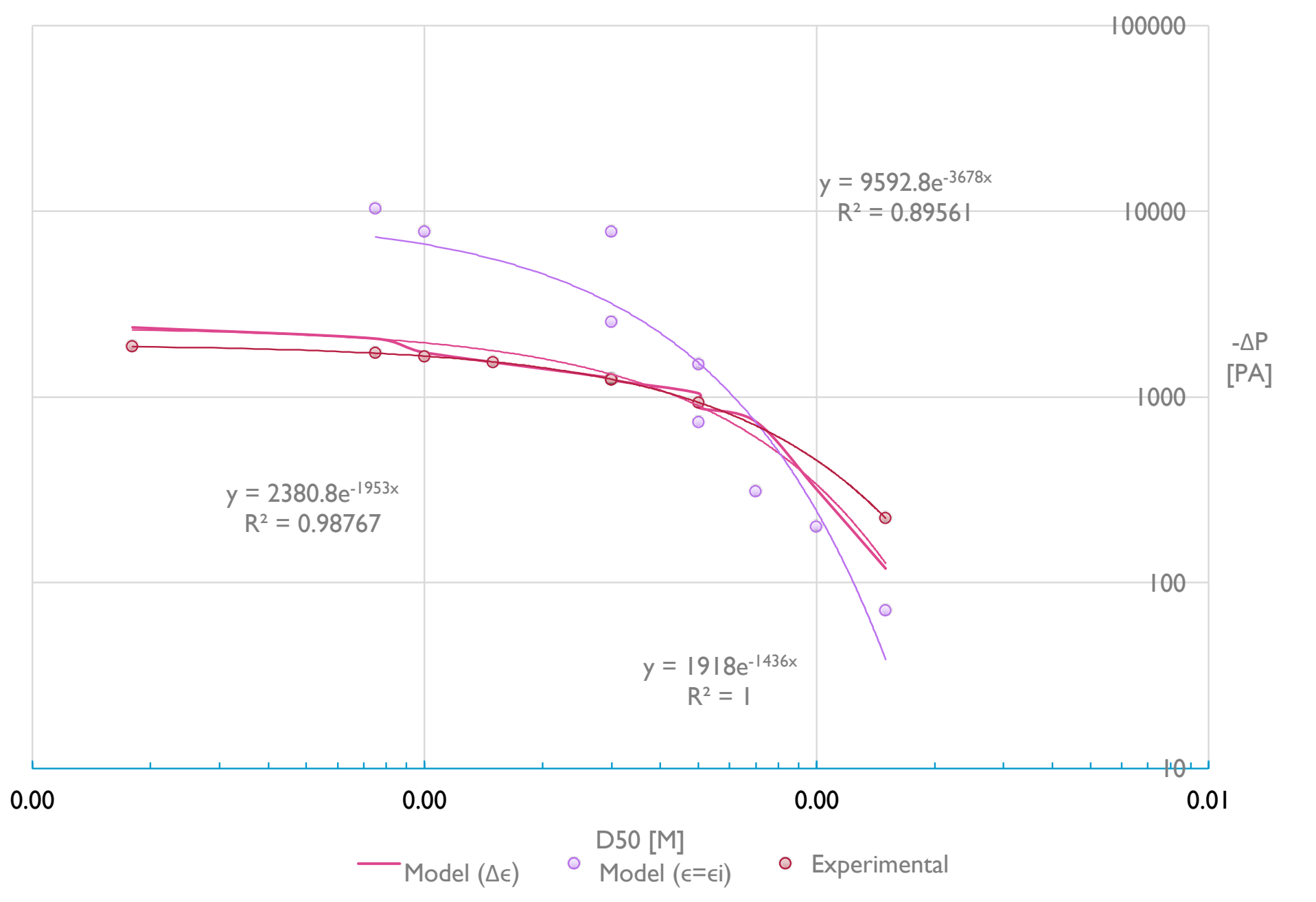

- ❑ A transient die filling model is then proposed, assuming the negative pressure is primarily induced in the wakes of falling particles.
- ❑ The model can predict the pressure change provided the voidage in the flowing powder stream can be approximated.

5. Correlation between powder flowability and die filling performance

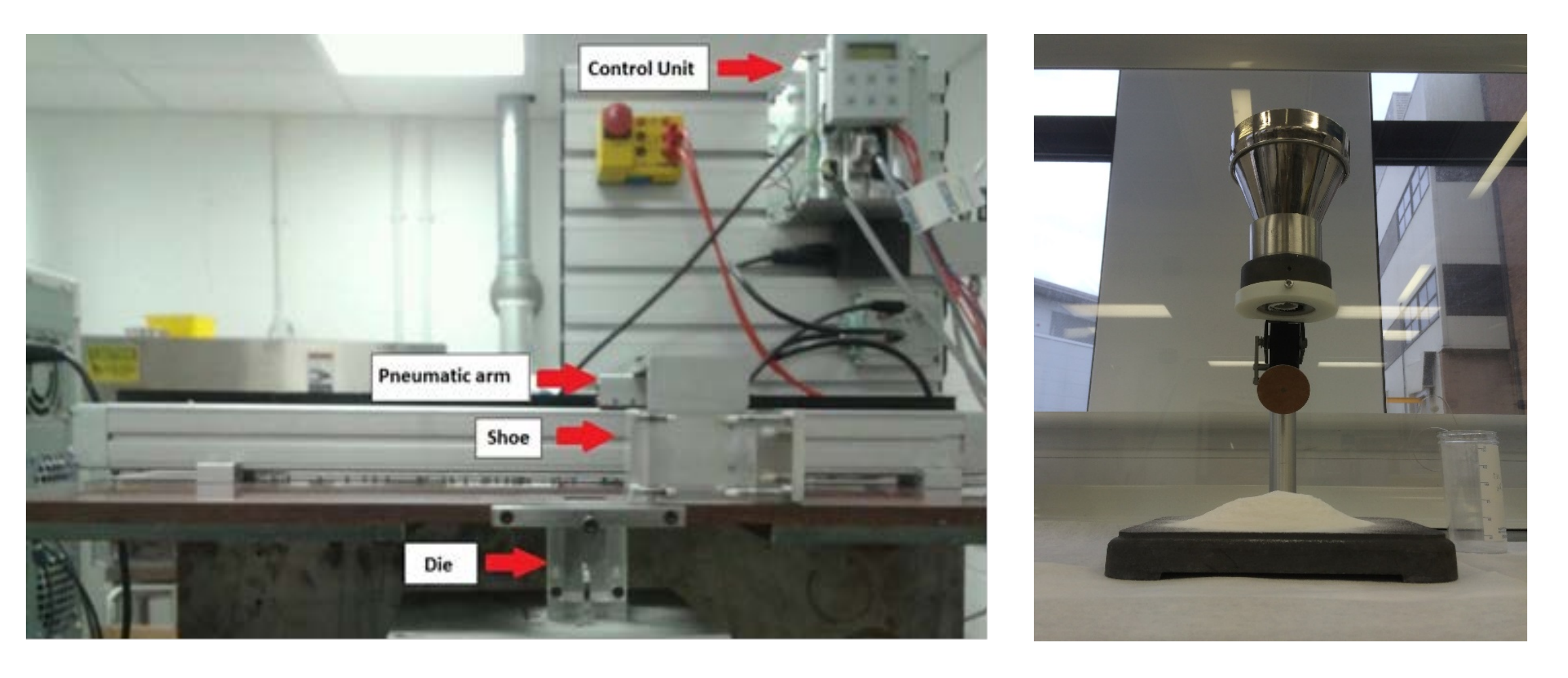

- ❑ Critical filling speed was proposed to characterise die filling performance.
- ❑ It is the highest filling speed at which the die can be completely filled.
- ❑ Attempts were made to explore the dependency of the critical filling speed on other flow-ability measurements,. such as the flow index measured using a Flodex tester.
- ❑ A wide range of materials and granules made of binary mixtures were evaluated.
- ❑ It was found that there is a strong correlation between the critical filling speeds and the flow index.

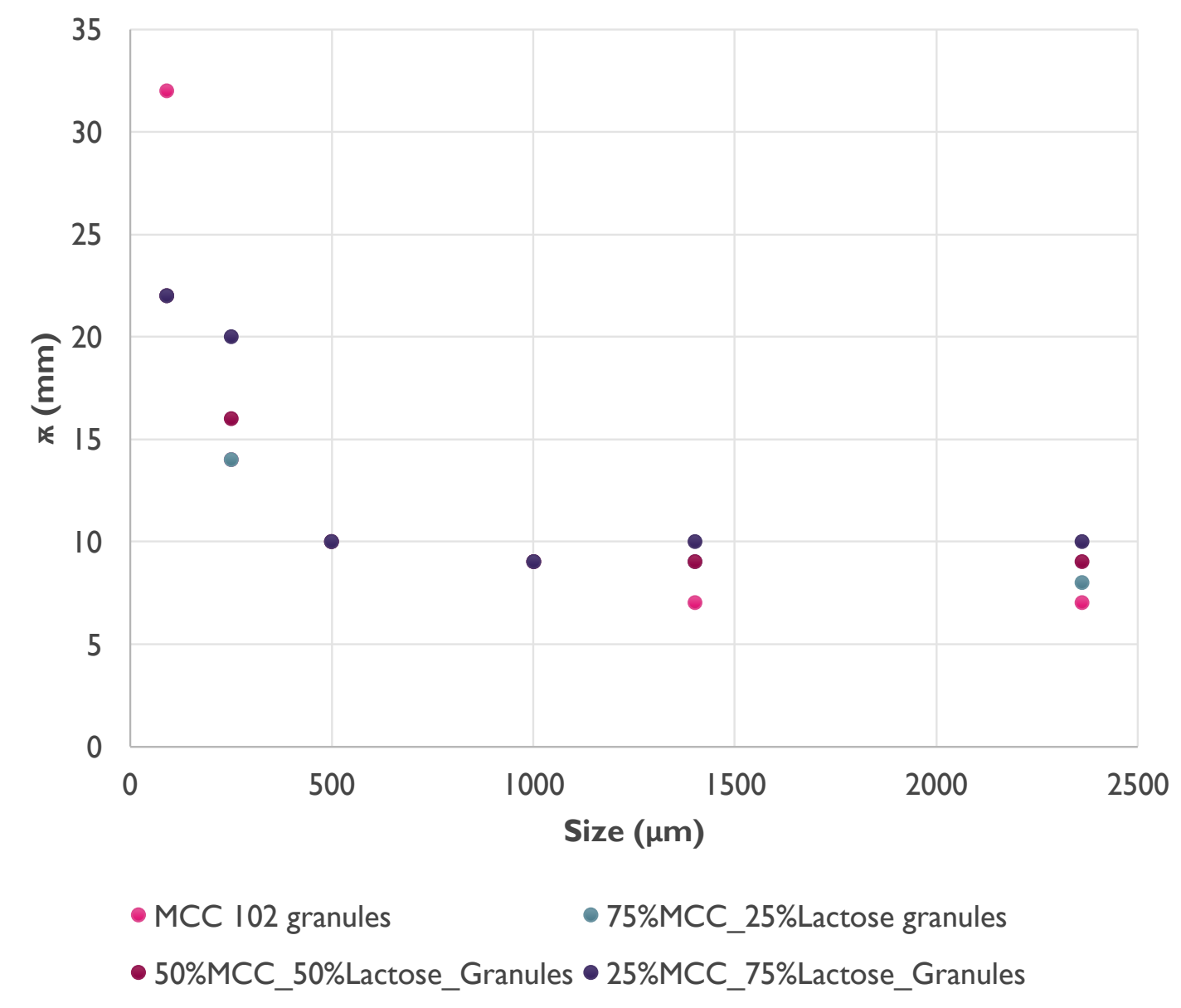

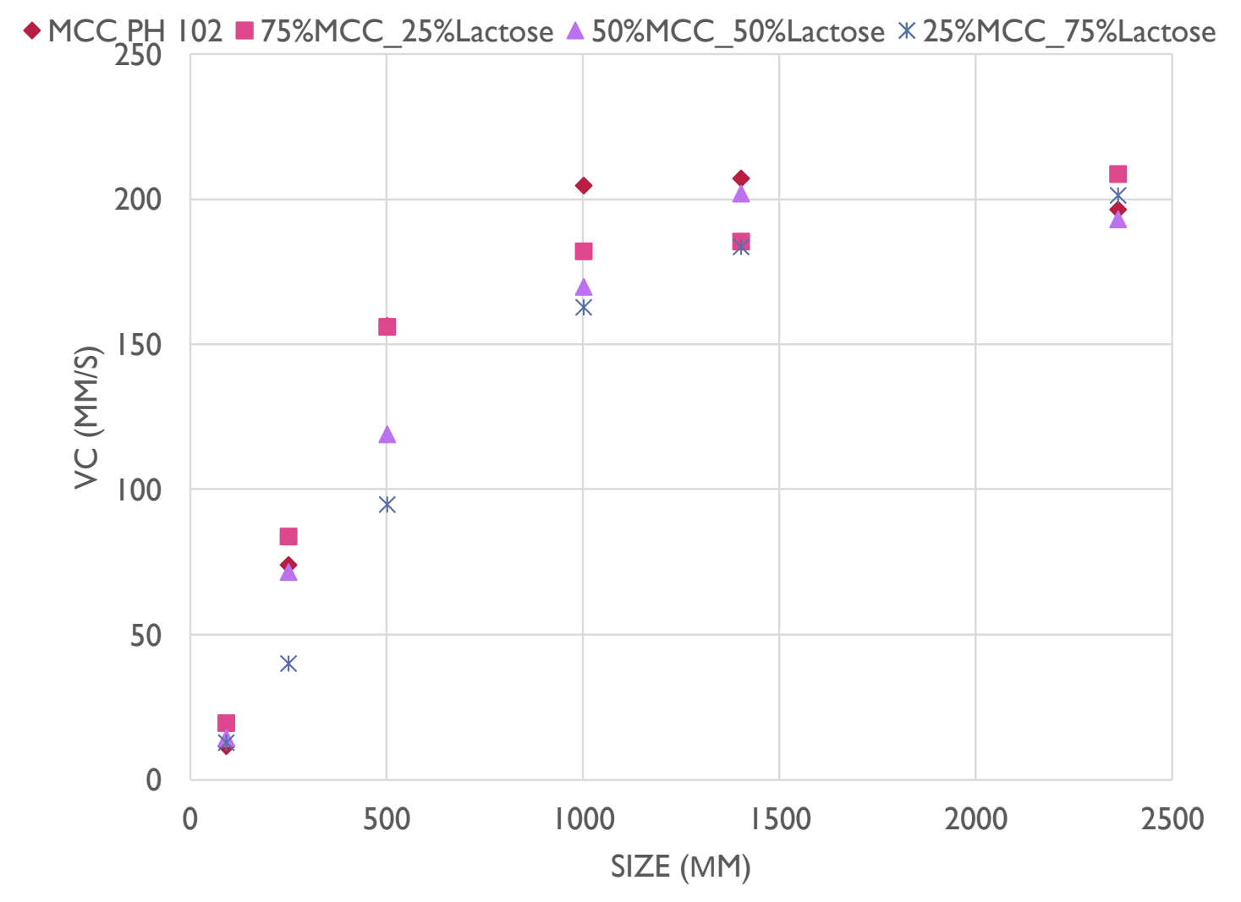

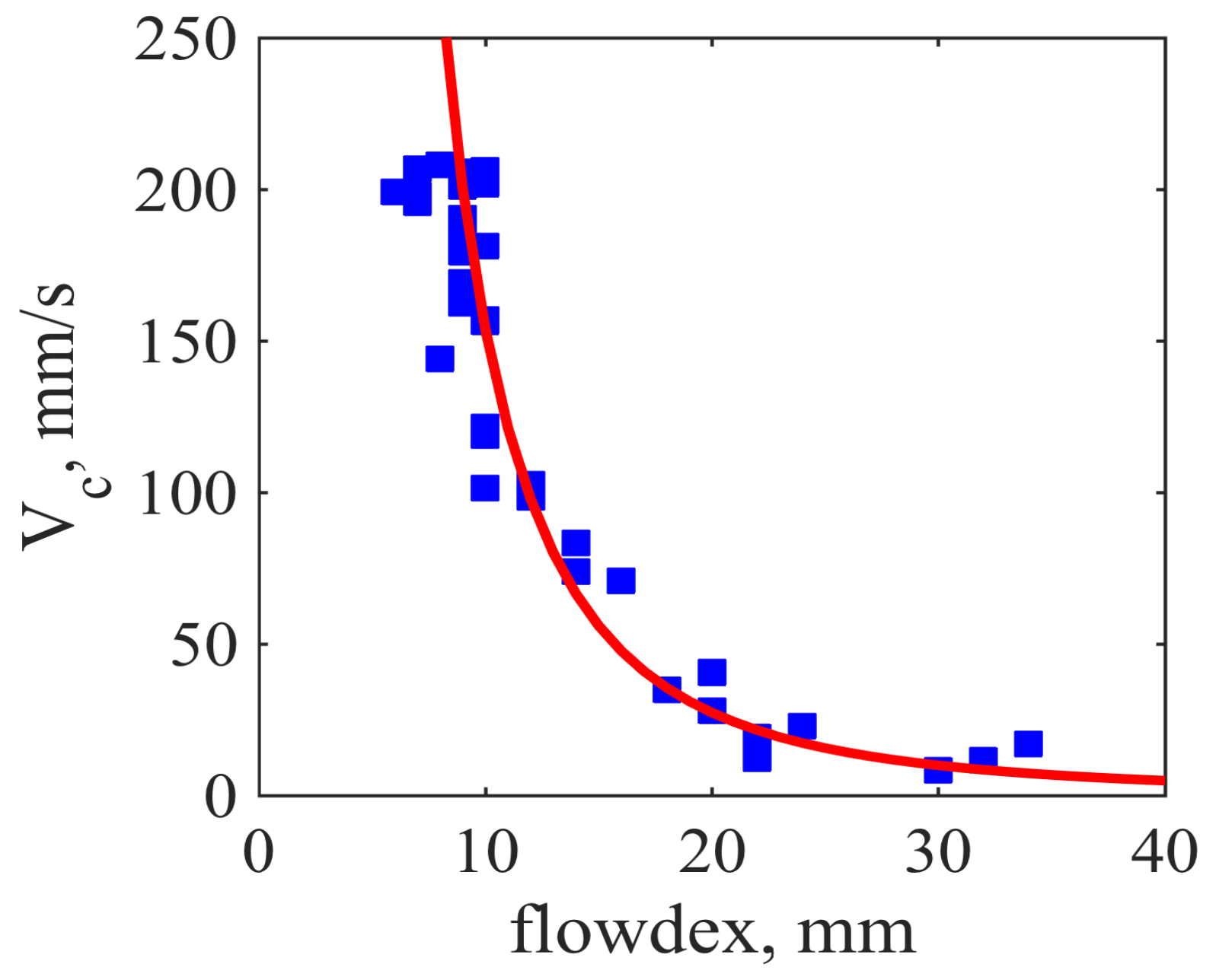

6. Summary and future work

- ❑ Active (rotary) die filling can lead to higher filling efficiency than passive (linear) filling.
- ❑ Significant density induced segregation can be induced die filling.
- ❑ A theoretical framework was developed to predict the air pressure build up during die filling. Its accuracy relies on the precise determination of porosity.
- ❑ Critical filling speed has a strong correlation with the Flodex measurements

The following future work is planned

1) Suction filling: system development and detailed experimental investigation;
2) Paddled hopper/shoe: system development and preliminary investigation;
3) Correlation with other flow measurements;
4) Further rotary die filling study – moist/cohesive powders.